UNIVERSITA' DEGLI STUDI DI MILANO

School of Veterinary Medicine

PhD Course in Veterinary and Animal Science

Class XXXII

SHEEP AS ANIMAL MODEL IN MINIMALLY INVASIVE NEUROSURGERY IN EDEN2020

Marco Trovatelli

Tutor: Prof. Fabio ACOCELLA

Coordinator: Prof. Valeria Grieco

PhD Candidate: Marco TROVATELLI

R11611

Academic Year 2018-2019

Summary

Abstract

Glioblastomas (GBMs) is a malignant type of central nervous system tumours and its presentation is almost 80% of all malignant primary brain neoplasia. This kind of tumour is highly invasive infiltrating the white matter area and is confined to the central nervous with a very poor patient outcome survival around 10 months. Of the existing treatment approaches, Convection Enhanced drug Delivery (CED) offers several advantages for the patient but still suffers from significant shortcomings.

Enhanced Delivery Ecosystem for Neurosurgery in 2020 (EDEN2020) is a European project supported with a new catheter development as the key project point in an integrated technology platform for minimally invasive neurosurgery. Due to the particular anatomy and size, sheep (*Ovis aries*) have been selected as experimental large animal model and a new Head Frame system MRI/CT compatible has been made and validated *ad hoc* for the project. In order to understand experimentally the best target point for the catheter introduction a sheep brain DTI atlas has been created. Corticospinal tract (CST), corpus callosum (CC), fornix (FX), visual pathway (VP) and occipitofrontal fascicle (OF), have been identified bilaterally for all the animals. Three of these white matter tracts, the corpus callosum, the fornix and the corona radiata, have been selected to understand the drugs diffusion properties and create a computational model of diffusivity inside the white matter substance. The analysis have been conducted via Focused Ion Beam using scanning Electron Microscopy combined with focused ion beam milling and a 2D analysis and 3D reconstruction made. The results showed homogeneous myelination via detection of ~40% content of lipids in all the different fibre tracts and the fibrous organisation of the tissue described as composite material presenting elliptical tubular fibres with an average cross-sectional area of circa 0.52µm^2 and an estimated mean diameter of 1.15µm.

Finally, as the project is currently ongoing, we provided an overview on the future experimental steps focalised on the brain tissue damage after the rigid catheter introduction

Project overview

Brain diseases cost the European Economy approximately 35% of the overall disease burden despite the high number of all brain diseases, brain tumours are low in terms of prevalence but highly costly per patient. It is estimate that the cost per patient in brain tumours is 33900 euros [16-18]. The world age-standardised incidence rate of malignant brain tumour for Italy has been estimated at 6.2 per 100,000 in men and 4.2 in women [19].

Psychotic/affective disorders and addiction are the leading source of expenditures (€18.7 billion), followed by neurological (€12.4 billion) and neurosurgical disorders (€ 1.0 billion). Direct medical costs are the leading cost item for psychiatric and neurosurgical disorders, direct non-medical costs for dementia and indirect costs for neurological disorders. However, important cost categories are missing for several disorders, for example direct non-medical costs could not be included for brain tumours and the costs of stroke, brain tumour and trauma are even grossly underestimated as being based on incidence[20].

Glioblastomas (GBMs) is a malignant type of central nervous system tumours and its presentation is almost 80% of all malignant primary brain neoplasia[21].

This kind of tumour is highly invasive infiltrating the white matter area and they are confined to the central nervous, showing no metastases.

Due to this high infiltration tissue rate there is no standard of care in the major of cases and long-term survival statistics remain poor due to recurrence and the unavoidable side effects of repeat systemic therapies. In literature is reported as after first-line treatment, virtually all glioblastoma patients experience disease progression after a median of survival of 7 to 10 months[22].

Their treatment generally involves a combination of ablative therapy (e.g. radiotherapy), systemic therapy (e.g. chemotherapy), surgical resection, and localized drug delivery.

Of the existing treatment approaches[23], Convection Enhanced drug Delivery (CED) offers several advantages for the patient, however the CED procedure still suffers from significant shortcomings.

Enhanced Delivery Ecosystem for Neurosurgery in 2020 (EDEN2020) is a European project supported by the European Union's EU Research and Innovation programme Horizon 2020 under grant agreement n° 688279.

The main aim of EDEN2020 is to provide a step change in the treatment of brain disease by delivering an integrated technology platform for minimally invasive neurosurgery focusing on the integration of different technologies:

- pre-operative MRI and diffusion-MRI imaging;
- intra-operative ultrasounds;
- robotic assisted catheter steering;
- brain diffusion modelling;
- robotics assisted neurosurgical robotic product (Neuromate®).

EDEN2020 is built around two parallel research threads, the first focused on a clinical investigation of diffusion, encompassing experiments and computational modelling, and the other on technological development of the catheter and catheter controller, intelligent planner, real-time intra-operative visualisation and tracking, and in vivo diagnostics via flexible access.

Clinical research activities workflow has been validated in a staged approach throughout the project three sequential animal trials: *ex vivo* experiments to fine tune system performance and procedural work flow; *in vivo* ovine trials to ascertain feasibility of the system under realistic operating conditions; *in vivo* study to evaluate and verify system performance in a clinical setting.

The present PhD thesis has been part of the clinical research area focused on sheep as animal model. Due to the high level of the project regarding neurosurgery in large animal model, some technical issues about the surgical tools customized for our purposes were presented. For this reason the first step of my PhD has been focused on “Development and in-vivo Assessment of a Novel MRI-Compatible Stereotactic System for the Ovine Animal Model”.

Once the head frame system has been validated the animal model has been studied under anatomical MRI and DTI in order to create a sheep brain atlas, summarized in the manuscript: “In vivo diffusion tensor magnetic resonance tractography of the sheep brain: an atlas of the ovine white matter fiber bundles”.

Further aim in EDEN 2020 is to understand the drugs diffusion properties and create a computational model of diffusivity. To achieve this, the brain tissue has been modelled on the base of white matter microstructure. The third year of my PhD has been focused on the study of white matter samples via FIB-SEM microscope and 3D reconstruction of axons bundles for different sheep white matter tracts presented in “Cytoarchitecture of commissural, association and projection fibres: a comparative study”.

In summary, the following thesis has been realized in a way to follow all the procedural steps carried out during the conduction of my PhD. The thesis is divided in two main chapters, the former after a brief overview about EDEN2020 project, is focalized on the animal model, why has been selected and his anatomical skull, brain and vascular features.

The latter is about the technical work resulting from project workflow. This area in subdivided in sub-chapters for each work presented as scientific journal papers.

The thesis ends focusing on further work related to EDEN2020 project which is ongoing during the PhD thesis submission. Here is presented the rational method to study and analyse the brain tissue damage during the catheter surgical insertion procedure. A minor additional work related to the PhD period is also presented. An ovine brain slicer has been created and proposed as innovative tool for ovine animal model brain sampling.

Chapter 1

EDEN2020

Enhanced Delivery Ecosystem for Neurosurgery in 2020 (EDEN2020) is a European project supported by the European Union's EU Research and Innovation programme Horizon 2020 under grant agreement n° 688279.

The main aim of EDEN2020 is to provide a step change in the treatment of brain disease by delivering an integrated technology platform for minimally invasive neurosurgery focusing on the integration of different technologies:

- pre-operative MRI and diffusion-MRI imaging;
- intra-operative ultrasounds;
- robotic assisted catheter steering;
- brain diffusion modelling;
- robotics assisted neurosurgical robotic product (Neuromate®).

To achieve the project's objectives the consortium is composed by different research institutions and companies working together providing different technical and clinical skills.

University of Milan is part of this research consortium with the veterinary team as active part in the experimental phases with *ex vivo* and *in vivo* trials on sheep as animal model.

Brain diseases cost the European Economy approximately 35% of the overall disease burden despite the high number of all brain diseases, brain tumours are low in terms of prevalence but highly costly per patient. It is estimate that the cost per patient in brain neoplasia is 33900 euros [16-18]

Glioblastomas (GBMs) is a malignant type of central nervous system tumours and its presentation is almost 80% of all malignant primary brain cancers[21].

Currently the World Health Organization classified gliomas from 1 to 4^{th} on the base of histopathological criteria described by degree of undifferentiation, anaplasia and aggressiveness[24].

Glioblastoma results as 82% of case in malignant glioma and it is characterised by high cellularity mitotic activity, vascular proliferation and necrosis. Typical of this neoplasia is a high pleomorphic rate giving the common name of glioblastoma multiforme.

This kind of tumour is highly invasive infiltrating the white matter area and they are confined to the central nervous, showing no metastases.

Due to this high infiltration tissue rate there is no standard of care in the major of cases and long-term survival statistics remain poor due to recurrence and the unavoidable side effects of repeat systemic therapies. In literature is reported as after first-line treatment, virtually all glioblastoma patients experience disease progression after a median of survival of 7 to 10 months[22].

Their treatment generally involves a combination of ablative therapy (e.g. radiotherapy), systemic therapy (e.g. chemotherapy), surgical resection, and localized drug delivery.

White matter tracts are critical to the treatment of glioblastoma because they can be incorporated into imaging to define cancer extents; they determine the limits of surgical resection; they may provide pathways for the spread of disease; and they have markedly different diffusion characteristics than grey matter.

Of the existing treatment approaches[23], Convection Enhanced drug Delivery (CED) offers several advantages for the patient, including minimal access, circumvention of the blood-brain-barrier (BBB), which limits the degree of absorption of drugs delivered systemically[25], and better chronic disease management, thanks to the ability to alter the drug regime over time, as the lesion adapts and develops resistance. In CED, drugs are delivered directly to the neoplasia or resected site. A catheter attached to a drug reservoir is inserted into the target and a pressure gradient ("convection enhanced") improves diffusion into the tissue[26].

However the CED procedure still suffers from significant shortcomings, including reflux (the drug flowing back towards the surface via the pathway generated by the catheter during the insertion process), inaccurate catheter placement (due to brain shift and tissue deformation) and limited drug distribution within the substrate at the point of delivery[26].

Over the past 15 years, neurosurgery has been characterized by a fast growth in the advancement and clinical adoption of new imaging modalities as high resolution brain topology information from Computer Tomography (CT) and Magnetic Resonance Imaging (MRI). Diffusion tensor imaging (DTI) is a form of diffusion weighted MRI that assesses physiological water directionality and motion, providing images of important white matter tracts within the Central Nervous System (CNS)[27].

Information from DTI has been noted to give an high impact in the neuro-oncology patient outcomes thanks to the improvement in the identification of resection boundaries with better accuracy than MRI alone; highlighting substantial subcortical connections and preserve it, allowing the re-

organization of the CNS and a better patient outcomes in terms of both life expectancy and quality of life[28].

While DTI offers excellent pre-operative imaging to support patient-specific planning for both resection and targeted delivery of therapeutics, intra-operative brain shift following bone flap elevation (correlated to the extent of deliquoration occurring due gravitational forces) affects the spatial relationship between the key anatomical regions; and instrument-tissue interactions further disrupt the mapping process. Consequently, while open resection provides an adequate workspace for the surgeon to adapt to the changing anatomy, all minimally invasive instruments used in current neurosurgical practice (for e.g. biopsy, electrical stimulation, drug delivery systems, etc.) are guided via rigid cannulas and thus constrained to lie on a straight insertion path. The complexity of white matter tracts and the profound effect that has on key therapeutic choices (location, approach direction, insertion trajectory) justifies the need for a new technology platform for minimally invasive neurosurgery, which is what EDEN2020 aims to provide.

The new catheter development is the key project point, indeed the catheter concept is based on a steerable multi-segment catheter designed to follow precisely adaptive curvilinear trajectories.

While the catheter EDEN2020 cannot be readily compared to other commercial systems, since none exist in the needle steering field to date, the placement accuracy and repeatability figures for the catheter are compared to rigid placement of a rigid needle of equal size and shape, placed via conventional stereotactic frame.

In summary, EDEN2020 aim is to address the remaining limitations by developing a technology platform for the accurate delivery of pharmaceutical agents to lesions within the brain.

Animal model

3R rules had a huge impact in the animal model sciences. In 1959, William Russell and Rex Burch published "The Principles of Humane Experimental Technique". They proposed that if animals were to be used in experiments, every effort should be made to Replace them with non-sentient alternatives, to Reduce to a minimum the number of animals used, and to Refine experiments which used animals so that they caused the minimum pain and distress. Refinement can also be achieved by moving from species that are considered more sentient to those less sentient.

The choice for the most accurate animal model for EDEN2020 has begun with the analysis of the project aim. EDEN2020 project has been focused on the validation of an integrated technology platform for minimally invasive neurosurgery. To achieve this aim a proper animal model must be taken in consideration

In respect of the 3R rules and in order to obtain the best translational value, large animal models have been contemplated as better models then small models as mouse, rat, rabbit, even though small-animal models are usually favourited due to low cost, ease of care, and the possibilities for high work rate. While they are still valuable for answering some basic research questions, the translation of therapeutic approaches from bench to bed is usually unsuccessful. Thus, there is a growing awareness that therapies should be tested in large-animal models prior to clinical application[29].

Besides, murine models are characterized by smooth (lissencephalic) neocortex. Accordingly, the gyrification index (GI), which is defined as the ratio of total neocortical surface area (including sulci) to superficially exposed neocortical surface area, the measurements of GI range from lissencephaly has a GI rate of 1.00 quite distant for Humans (GI = 2.56)[30].

The rabbit brain is counted among the lissencephalic brain type in contrast to the gyrencephalic one and it is characterized by a GI of 1.2.

Other animal model with a proper gyrencephalic brain as domestic animals, dogs and cats, are not been used as for their brain size but even for an ethical restriction. Considering the relationship between brain and spinal cords and the ratio of brain to head mass non-human primates are most similar to humans compare with quadrupeds which are characterized by brain and spinal cord long

axes parallel while in humans have a right angle [31] but for ethical reason have been excluded from the animal model considerations.

In light of this restrictions showed before, large animals models seem to have better characteristic then other animal models (figure1).

Pig as animal model has been used in neuroscience [32, 33] but the anatomical features in the skull create some limitations. The anterior pig head has a plane forehead and vertex that end in a high crest where the neck muscles are inserted. Laterally, the vertex is limited by the parietal bone, reducing the brain access area to a small square[34]. Additionally minipig breeds and domestic pig have a fast growth index if compared with sheep, with an average daily weight grain for Large White-Landrace reported to be between 734 and 992 g/day in the first six months of life[35] reaching the adult stage (1-2 years in age) at more than 300 Kg[32]. Last minipig and pig models at 3-6 months develop a sizeable frontal sinus that pneumatizes all of the dorsolateral part of the skull[36], thus becoming impracticable for application in neurosurgery experiments and chronic postoperative management[37]

Due to their particular anatomy and size, sheep (*Ovis aries*) have been largely used as experimental large animal models in a multitude of specialities in biomedical research varying from orthopaedics[38], traumatic brain injury[39] and neurological disorders[40].
In terms of neuroanatomical similarities, sheep exhibits many resemblances to the human regarding electroencephalographic elements [41], neuroradiological features [42], neurovascular structure [43] and skull ovine anatomy is close to humans in regards to thickness, porosity and the curvature of the calvarium (figure1-2)[1].
In light of these characteristics cadaveric sheep brains have been largely used as teaching material for mammalian cerebral anatomy [44] and several neurosurgical techniques have been developed and tested through this neurosurgical model. Hamamcioglu et al. described a laboratory dissection of cranial nerves in the posterior fossa[45]. Another cranial approach proposed in ovine model has been the orbital surgery simulation by Altunrende et al.[46]
In the field of paediatric neurosurgery, training in the area of craniosynostosis can be very useful in familiarizing the thickness of the calvarial and facial bone being similar to that found in paediatric patients[47].
Ovine model has been even used for neuro-oncological training, where Kamp et al. simulated cerebral masses in cadaveric sheep brains using an agar-agar and ink solution[48].

For these reasons sheep fitted mostly the anatomical features to perform EDEN2020 project and it has been considered as ideal animal model for the experimental protocol.

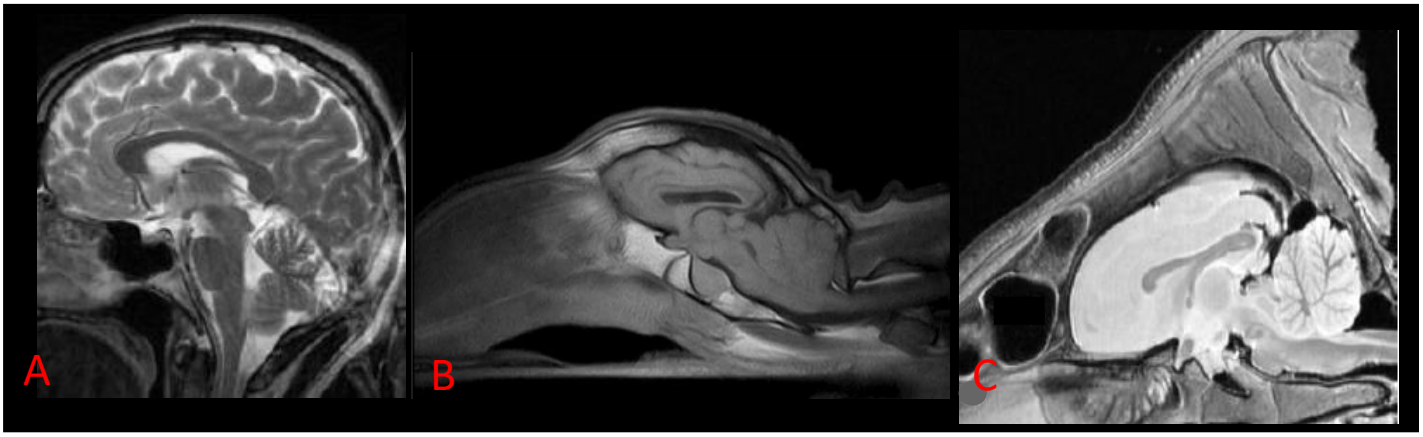

Figure 1 Magnetic resonance of Human, Sheep, Pig brain. A) Medial sagittal acquisition of Human brain B) Ovine Brain C) Pig Brain. Note the different thickness and curvature of the calvarium[5, 6]

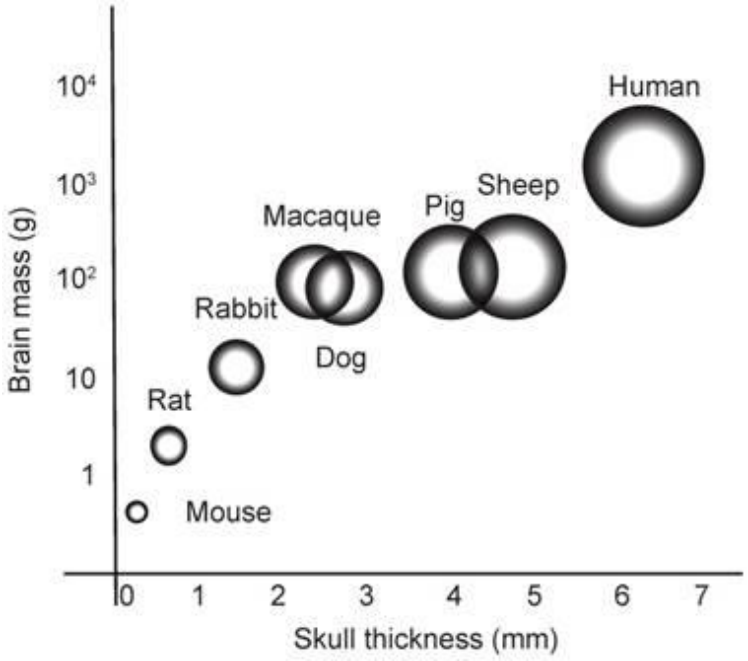

Figure 2 Brain mass in animal models [1, 2]

The head Anatomy

In the beginning of my PhD project the study of the skull anatomy has played a fundamental role in order to understand and plan all the following procedural steps in this research.
The sheep cranium has been analysed and each features studied trying to find the best points for the head frame system development and underline the best technical point for craniotomy finding the subsequent surgical scenario. For these reasons here below is presented a detailed anatomical dissertation on sheep head anatomy.
The skull is a dynamic structure composed by flat bones characterised by fibrous sutures at the edges of them which allow cranium expansion during the brain growth.

The cranium is composed of seven flat bones of which five are unequal; the occipital, parietal, frontal, sphenoid and ethmoid; one only, the temporal, is double. These bones circumscribe the cranium cavity which communicates behind with the spinal canal, and lodges the brain. (figure 3)

Sheep is characterized by a long gestation time of 145 days and during its intrauterine life has an early calvarial bone formation. The prolonged time gestation of the lamb allows indeed a complete suture fusion in utero[49].

During the embryogenesis the skull development can be shared in three different phases: neuro-cranium, dermato-cranium and splanchno-cranium. The neuro cranium creates a cavity fulfilled by all the brain except the telencephalon. The dermato-cranium is composed by the *cranii* vault bones and the nose bones. The splanchnocranium is composed by the maxillary bones and the scheletric structures from the pharyngeal arch mesenchyme.

During the embryogenesis the neurocranium appear as mesenchymal dense structure located under the brain and as epithelial sensing capsules (olfactory, optic and otic). These capsules chondrificate together forming a ventral-cranial structure to the immature brain. Lateral processes are created by a dorsal development of this formation, following the brain shape modifications. Numerous bone centres for sphenoid, occipital, vomer and ethmoid creation are then made. These ossification centres with cartilaginous tissues forms the endochondral bones.

At the same time the encephalic mesenchyma and the dorsal ectoderm tissue create the intramembranous bone formation of the cranial vault and just when all the bones development relations are right the splanchno-cranii can begin its ossification.[50] The earliest distinct centre of

ossification is the mandible, which appear at day 39th, and is rapidly followed by the pre-maxilla, maxilla and the tectum posticum. At day 41 the supra occipital ossification centre is noted followed by the frontal, zygomatic bone at day 43 and premaxilla, parietal and squamosal bone at day 46. The exoccipital, basi occipital and basi sphenoid centres are created at day 47 and pre-sphenoid and periotic at day 48.

The growth process appear accelerate at day 61 when the vertebral column ossification centres are presents and at day 68 both tympanic ring and the squama of the temporal bones are defined[51].

The prolonged time gestation of the lamb allow a complete suture fusion in utero [49]. In adult sheep sutures are, from back to forward, the lamboid, sagittal, coronal and interfrontal suture.

Lamboid suture is the junction between the superior border of the occipital bone and the posterior borders of the parietal bones. The sagittal suture divides the parietal bones, the coronal sutures separates the frontal and the parietal bones and the interfrontal suture is located between the paired frontal bones and it is the analogous of the metopic suture in humans[52].

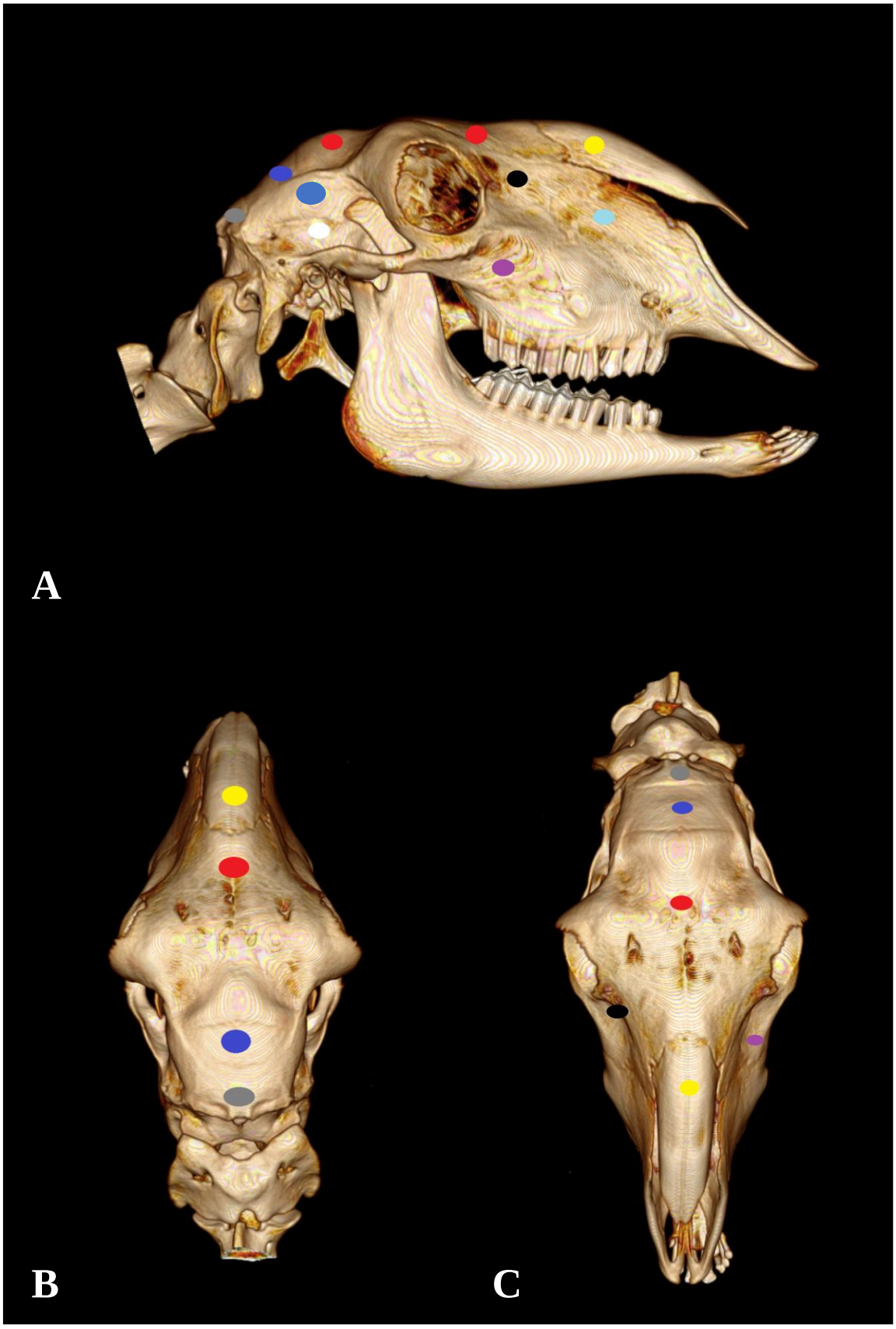

Figure 3 Sheep skull anatomy. A) lateral view B) Caudal view C) Frontal view. Each skull bone is presented with a different colour ring. Frontal bone (Red), Parietal (Blue), Occipital(Grey), Temporal (White), Nasal (Yellow), Lacrimal (Black), Zygomatic (Purple) and Maxilla (Light Blue)

Occipital Bone

The occipital bone occupies the superior extremity of the head and it is bent at a right angle in front and behind. It is composed by an external and an internal face and a circumference which brings it into contact with the adjoining cranial bones; the latter is subdivided into two anterior lateral borders, two posterior lateral borders, an anterior and posterior salient angle, and two lateral reentering angles.

The external face is divided into three portions by the double flexure of the bone and on the median line shows the external occipital tuberosity. This protuberance forms the culminating point of the head and divides the anterior and superior parts of the external face of the bone.

The occipital foramen or *foramen magnum*, is a large orifice which establishes a communication between the cranial cavity and spinal canal.

The occipital bone is composed on its side by a high crest occupying the top of the head and prolongs laterally and descends medially continuing with the superior root of the zygomatic process and the mastoid crest of the temporal bone. In parallel of this crest a second line prolongs on the base of the styloid process. Close to these is defined a posterior recti muscles insertion.

The external surface of the basilar process is a laterally convex surface. It is a narrow and thick bone prolongation that meet the sphenoid bone.

The internal surface is concave and it is composed by an area forming the roof of the cerebral cavity and below it the superior face of the basilar process. On foramen magnum sides the internal orifice of the condyloid foramen is presented.

The anterior lateral borders are thick, and are united by suture with the parietal bone, and with the tuberous portion of the temporal bone by the harmonia suture. The posterior lateral borders are sharp and form the sides of the basilar process helping to create the *foramen lacerum basis cranii*. The anterior angle interlocks in the parietal bone. The posterior angle is thick and forms the summit of the basilar process and it is united by suture with the body of the sphenoid. The lateral re-entering angles are occupied by the petrous portion of the temporal bone[53, 54].

The parietal bone

The parietal bone is a wide and thin bone forming the roof of the cranial cavity. It is characterized by no sinuses and it is bounded above by the occipital bone, below by the frontal and laterally by the two temporal bones.

The external face is convex and it exhibits two curved crests which terms with the parietal ridges and join each other superiorly continuing with the anteroposterior ridge of the occipital bone. They below diverge and proceed joining the supra-orbital process.

The surface is divided into three portions: two lateral areas, which are rough and traversed by vascular channels, forms part of the temporal fossa; the third is in the middle and it is plane and smooth.

The internal face is concave, covered by digital impressions, and grooved by small vascular canals. On each side it is composed by an excavation elongated transversely where a venous sinus is located and where opens the parieto-temporal canal. The internal face is continued frontally by a median crest and two other crests rise from the sides of this eminence and descend to the sphenoid bone dividing the cerebral from the cerebellar cavity.

The superior border is thick and has an irregular surface, it articulates with the occipital bone. The inferior border, slightly concave, and deeply dentated. The other borders are thin and are composed by two portions. The inferior is articulated by suture with the squamous portion of the temporal bone and the superior, which is curved inwards towards the centre of the cranial cavity. The latter portion of the lateral border is in contact with the anterior face of the petrous portion of the temporal bone[53, 54].

The frontal bone

The frontal is a flat quadrilateral bone with the sides bent in the middle at an acute angle in order to meet the wings of the sphenoid bone.

It is bounded above by the parietal bone, ventrally by the nasal and lacrimal bones and on each side, by the temporal bones. The external face is divided into a middle and two lateral regions. The first

gives rise on each side a long process, flattened above and below, which curves backward, forming the orbital arch.

The external face of this process is convex and roughened; the internal face is smooth and concave, and forms part of the orbital fossa. Its posterior border continues with the corresponding parietal ridge, and externally with the superior border of the zygomatic process. The anterior border concurs in the formation of the orbital margin; the summit is thickened and denticulated and is united to the zygomatic process of the temporal bone while the base is wide and is traversed by an opening termed the supra-orbital foramen. The two lateral regions of the external face of the frontal bone participates to form the orbits.

The internal face of the frontal bone is concave and is divided into two unequal parts by a transverse ridge, corresponding to the anterior border of the cribriform plate of the ethmoid bone.

The superior face is the most extensive and it exhibits on the median line, a slight crest which is continuous dorsally with the median ridge of the parietal bone, and below, with the *crista-galli* process.

On the sides the superior surface receives the wing of the sphenoid bone. The inferior part joins on the median line the perpendicular plate of the ethmoid. It forms the bottom of the nasal cavities and presents laterally two large openings which lead to the frontal sinuses that are prolonged until the line passing to the back side of the orbital cavity.

The superior border is in contact with the parietal and squamous portion of the temporal bone.

The inferior border joins the nasal bones through the medium and laterally articulates with the lacrimal bone. The lateral borders, thin and irregular, present two notches: one, the superior , named *incisura sphenoidalis*, is occupied by the wing of the sphenoid bone. The other forms the orbital foramen which opens into the cranium close to the ethmoid fossa[53, 54].

The ethmoid bone

The ethmoid bone is located on the limit between the cranium and the face, enclosed between the frontal, the sphenoid, the vomer, the palatine and the supermaxillary bones. It is composed of three portions: a perpendicular lamina and two lateral masses.

The Perpendicular Lamina of the ethmoid bone is located in the mesian plane and flattened on both sides, presenting two faces, a left and right, and four borders. The faces are covered by the pituitary membrane characterized posteriorly by small sinuous crests.

The superior border looks towards the centre of the cranial cavity and constitutes the *crista-galli* process. It is concave and prolonged in front and above by the median crest of the frontal bone.

The inferior border is continuous with the cartilaginous plate which separates the nasal cavities.

The anterior border is consolidated with the vertical septum which separates the frontal sinuses. The posterior border is joined above to the median plate which divides the sphenoidal sinuses into two compartments and below, it is fixed with the vomer bone.

The lateral masses of the ethmoid bone are two large pyriform tuberosities placed on each side of the perpendicular lamina. Each of these is formed by the ethmoidal cells, numerous thin osseous plates curved into small convolutions, which are largely developed and forms the olfactory antrum.

The external surface of each ethmoidal mass is divided into an internal, making part of the nasal cavities and the external which forms the walls of the frontal and maxillary sinuses.

Internally, the lateral masses are composed by diverging canals which opens inferiorly into the nasal cavities.

The base of each lateral mass is composed by the cribriform plate of the ethmoidal bones giving passage to the ethmoidal.

The summit of each lateral mass is formed by the inferior extremity of the ethmoidal cells, which is directed downwards, towards the nasal cavities[53, 54].

Sphenoid bone

The sphenoid bone is situated behind the cranium, between the occipital, ethmoidal, palatine, vomer, pterygoid, frontal, and temporal bones.

It is a flattened and curved bone with its middle part named the body thick and tapers on the sides prolonging ventrally forming the wings.

The external surface is convex, externally the body continues with the basilar process, and dorsally it is characterized by muscular imprints. On the sides there is the pterygoid fissure, directed dorsoventrally, and continues by the pterygoid canal which opens into the orbital hiatus. The pterygoid process articulates with the palatine and pterygoid bones, and it is crossed by the pterygoid canal.

Dorsally is located the superior orifice of the sub-sphenoidal foramen and cranially is located the orbital hiatus, a vestibule with the principal branch of the subsphenoidal canal, the three supra-sphenoidal canals, the *vidian* and optic canals, and the orbital opening.

The internal face is concave and on the median line join the *crista galli* by a small projection. The

optic fossa ventrally offer the superior orifice of the optic foramen to reach the orbital hiatus. The supra-sphenoidal or pituitary fossa is named the *sella turcica*. *Sella turcica* is a depression characterized posteriorly by a curved lamina forming with its extremities the posterior clinoid processes.

Ventro caudally the sphenoid bone is composed by a fossa which the mastoid lobule of the brain is located. between this fossa and the *sella turcica* are presented two vertical fissures. One internal, named the cavernous sinus and one external which is dedicated for the passage of a large nervous branch.

These two fissures open near to the three supra-sphenoidal canals junction.

The superior of these is the *foramen lacerum orbitale* while the other fissure is the *foramen rotundum* opening into the orbital hiatus. The third fissure is a small one named *foramen patheticum* and opens above the optic foramen.

The superior border is concave and articulates with the summit of the basilar process. Two notches per sides defines the *foramen lacerum basis cranii*. The internal notch is named *carotid canal*. It is the narrowest and it is accepts the passage of its the internal carotid artery. The external notch is named *foramen ovale*, it is wider than the carotid canal and it is crossed by the inferior maxillary nerve. Outside is located the *foramen spinosum* which is narrow notch for the middle meningeal artery. All these fissures are composed by a fibro-cartilaginous substance that partially fills them.

The inferior border is concave and it is divides in a middle and two lateral sections. The first section is thick, and it is formed by the inferior extremity of the body. This part is characterized by two large

cavities belonging to the sphenoidal sinus. These cavities are separated from one another by a vertical osseous plate.

The lateral section is part of the circumference of the sphenoid wings and help the formation of the orbital foramen.

The lateral borders are thin and convex taking part of the wings while the rest of the lateral border is thick and articulate with the squamous portion of the temporal bone[53, 54].

The temporal bone

The temporal bones limit the cranial cavity laterally and it is articulated with the occipital, parietal,

frontal, sphenoidal, malar bones and with the inferior maxilla and the hyoid bone. Each temporal bones is divided into two pieces, one forming the squamous portion and the other forming the petrous portion.

The squamous portion is a flattened portion with a convex external face, and it is marked by some muscular imprints, vascular fissures, and openings which penetrate the parieto-temporal canal.

It forms part of the temporal fossa and gives origin to the zygomatic process at the base of which there is concave surface belonging to the temporal fossa and behind there is the articular surface of the maxillary bone.

The temporo- maxillar articulation is composed of the glenoid cavity and the maxillar condyle. The glenoid cavity is limited by the supra-condyloid process against which the maxillary condyle remain in passive position.

The external face of the zygomatic process is smooth and convex while the internal is concave, smooth and bordered outwards by the temporal fossa.

The internal face of squamous portion of the temporal bone is divided in two parts by a channel which terminates above the supra-condyloid process and creates the parieto-temporal canal.

The superior part of this parts has a triangular form and it is articulates by a suture with the external

face of the petrous portion. The inferior part is bigger and shows the cerebral impressions.

The anterior border is in relation with the parietal and frontal bones. The posterior border articulates with the sphenoid bone and at the level of the supra-condyloid process is characterized by the external auditory canal.

Dorsally, the two borders unite at the summit articulating with the occipital bone.

The petrous portion contains two systems of cavities which are the middle ear and internal ear. The external surface of this temporal portion is circumscribed anteriorly by the occipital bone, laterally by the parietal bone and the internal face of the temporal. It forms a quadrangular pyramid with a turned downwards base.

The anterior face is united by harmonia suture to the parietal bone and the posterior face join in the same way the occipital bone. The external face lies against the squamous portion of the bone while the internal face form the lateral wall of the cerebellar cavity.

Internally it is composed by the *meatus auditorius internus*

Important is the mastoid crest, a thick crest which after joining the superior root of zygomatic process continues with the occipital bone ending with the mastoid process for muscular insertion. This border is traversed by the mastoid fissure which passes under the squamous portion and enters the parieto-temporal canal.

The second important structure is the internal crest which divide the cerebral and cerebellar cavities of the cranium ang gives the attachment to the *tentorium cerebelli.*

The Base is composed by the external auditory hiatus and the external auditory canal which penetrates the middle ear.

Dorsally it is composed by the pre-mastoid foramen and the external orifice of the *aqueduct of Fallopius* while ventrally it composed by the styloid process for the *tensor palati* muscle and the *Eustachian tube*.

The styloid process is a long, thin process which shows the styloid foramen that enters the cavity of the tympanum.

The mastoid portion constitutes almost entirely the base of the temporal pyramid and which is part of it the external auditory canal, the mastoid process which is hardly distinct form the crest, the sheath of the hyoid prolongation, and the styloid process[53, 54].

Paranasal Sinuses anatomy

Nasal cavity is considered as a cylindrical cavity, divided by a midline nasal septum. Each side is characterized by maxillary sinuses and anteriorly by frontal sinus and sphenoidal and lacrimal sinuses which are grouped in the paranasal sinuses (figure 4).

The role of the paranasal sinuses is not yet clarified even if different hypothesis are considered as the decrease in the skull weight, humidify and heat the inspired air, protection against trauma[55].

Maxillary sinus

Maxillary sinus is in relation with maxilla and zygomatic bone, it begins from the second premolar tooth and extends reaching the infraorbital foramen while its base touch the rostro-ventral part of the orbital rim[56]. This sinus is divided by the infraorbital canal in a medial chamber, called palatinal sinus, and lateral chambers, the larger named maxillary sinus proper [57, 58]

Frontal sinus

Frontal sinus is characterized mainly by the frontal bone and rostrally with lacrimal bone and caudally with parietal bone.

This sinus extends from the second molar teeth line to 2 cm caudal to the posterior orbits limit. Laterally is limited by a line passing the orbital rim.

Frontal sinus is an air filled space between two layers of cortical bones which are the external cortex and the internal cortex that forms part of the endocranial cavity surface. The main aim of this sinus it to protect the vital cranial structures via shock absorption[59]

Differently from horned animals in sheep the frontal sinus in characterized by few septa. Medially this sinus is divided by the inter frontal septum in two different compartments, medial and lateral one. Lateral compartment is bigger than the medial and communicate with the middle nasal meatus by a naso-frontal opening. The medial section is subdivided in a rostral and caudal sub-compartments which are in communications with the dorsal conchal sinus and maxillary sinus by conch frontal opening and fronto maxillary opening respectively[56].

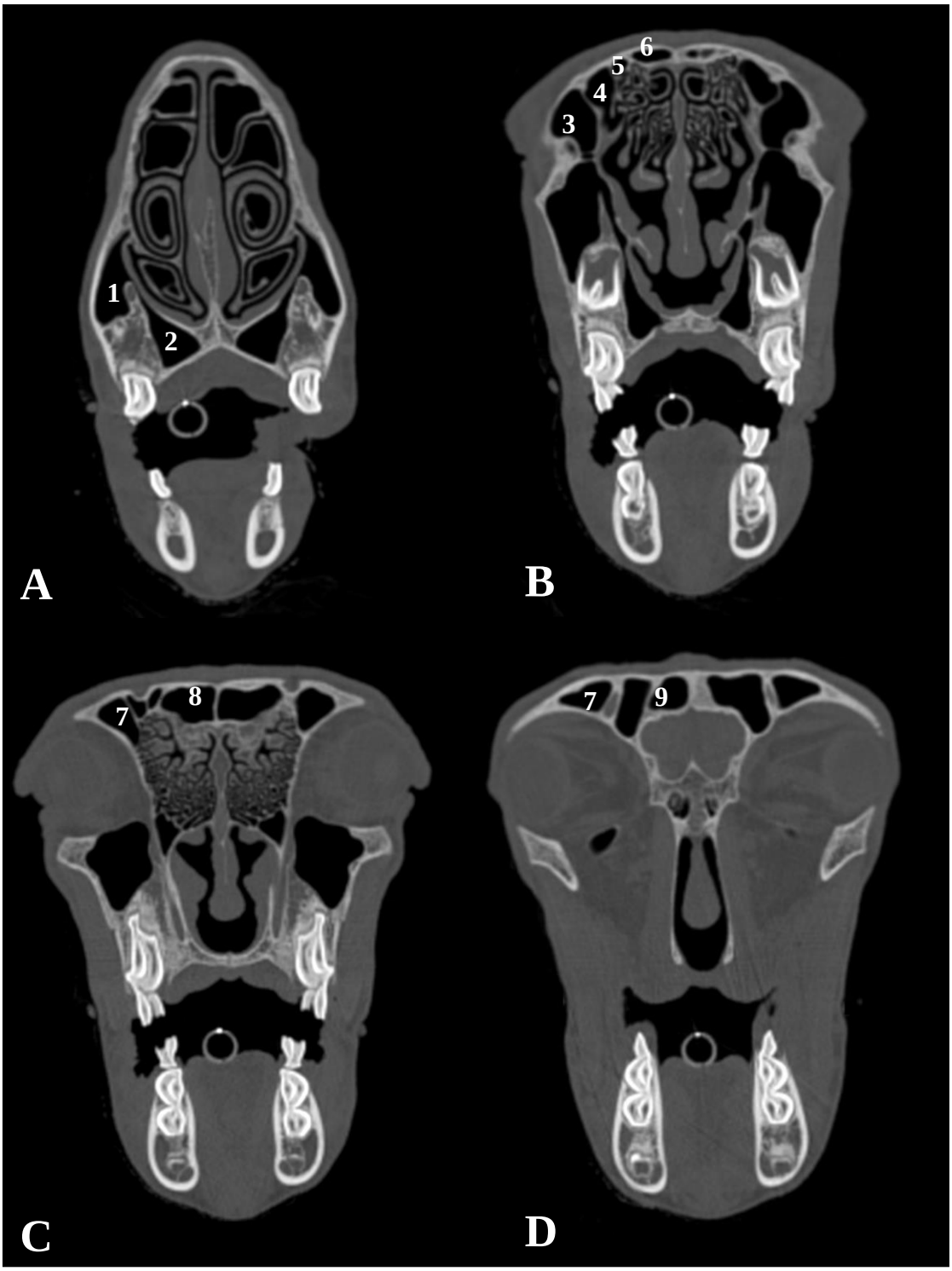

Figure 4: Sheep head sinuses CT. The acquisition are presented in cranial-caudal presentation where A is the most anterior plane and D posterior. In figure A can be observed the lateral chamber of the maxillary sinus (1) and medial chamber of the maxillary sinus (2). In figure B is localized the lacrimal sinus (3), lateral compartment of rostral frontal sinus (4), Intermediate compartment of rostral frontal sinus (5), medial compartment of rostral frontal sinus (6). In figure C can be observed the postorbital diverticulum of the caudal group of compartments of frontal sinus (7) and the middle group of compartments of frontal sinus (8). In figure D is presented the postorbital diverticulum of the caudal group of compartments of frontal sinus (7) and the nuchal diverticulum of the caudal group of compartments of frontal sinus (9)

Lacrimal sinus

Lacrimal sinus is a small sinus which extends in the lacrimal bones, in a rostrodorsal position to the orbital cavity[60]. Ventrally is limited by the nasolacrimal duct and is separated from the frontal sinus by a fine bony septum[56].

This sinus is in communication with the maxillary sinus via the maxilla lacrimal opening.

Sphenoidal sinus

The sphenoidal sinus is a small cavity contained in the body of sphenoid bone. Each of two sinuses are divided chambers not in communication[56].

Cerebral anatomy and morphology

Ovine cerebral hemispheres, similarly to human one, are divided in four lobes. The superior face of each hemisphere is convex and it is covered by the frontal and parietal bone of the skull. The external surface is covered by the squamous part of the temporal bone, the parietal and the frontal bone and the sphenoid ala bones while the inferior is located on the sphenoid bone.

The frontal, parietal, temporal and occipital lobes distinguish the morphological cerebral anatomy and are characterized. The convolutions are part of cerebral cortex and are limited by sulci, also named fissures.

Sheep is characterized by a long gestation time of 140-150 days after which the new born is behaviourally mature. The foetus brain surface at 60 days of gestation is lissencephalic but from the 66^{th} day begin to form the first impression of the suprasylvian gyrus.[61]

Embryologically the brain surface development begins with the fissure appearance followed by the sulci. Cortical adult sheep brain is characterized by cerebral convolutions, named also gyri, limited by sulci also named fissures. Gyrification is a process that maximize the number of cell bodies and minimize the distance between them in consequence of the limited space of the skull. The degree of gyrification seems to increase with the brain size and seems to be consequence of the brain growth in a restricted space, the skull, with limited degree of freedom in its modification[62].

Alternative hypothesis about gyri formation consider the tension developed by fibre tracts which connect different cortical areas[63]. Other hypotheses consider the developmental mechanisms of the cortex [64] or the relation between the thickness of supragranular versus infragranular layer of the cortex as cause of gyrification [65].

Cortical surface can be analysed using the gyrification index [66] which is the measure of the degree of folding and it is calculate as ratio between the total outer cortical surface and the superficially exposed part of the outer diameter. It has been noted that gyrification increase with the brain size up to the brain approximately 530g and cortical folding of mammals increases with decreasing cortical thickness in an order specific scaling. Thinner cortices allow for smaller and more numerous gyri, which results in more intense cortical folding relative to brain weight. Sheep is characterized by 2.29 of gyrification ratio with an adult weight brain approximately of 118 grams index [66]

The gyri and sulci are natural extensions of the subarachnoid space. The brain surface can be characterized by major or minor gyri (g.) with their sulcal spaces. Sulci (s.) can be long or short and can be resumed in four main type as large primary sulci (e.g arcuate), short primary sulci (e.g rhinal), short sulci composed by several branches and short free supplementary sulci. (figure 5)

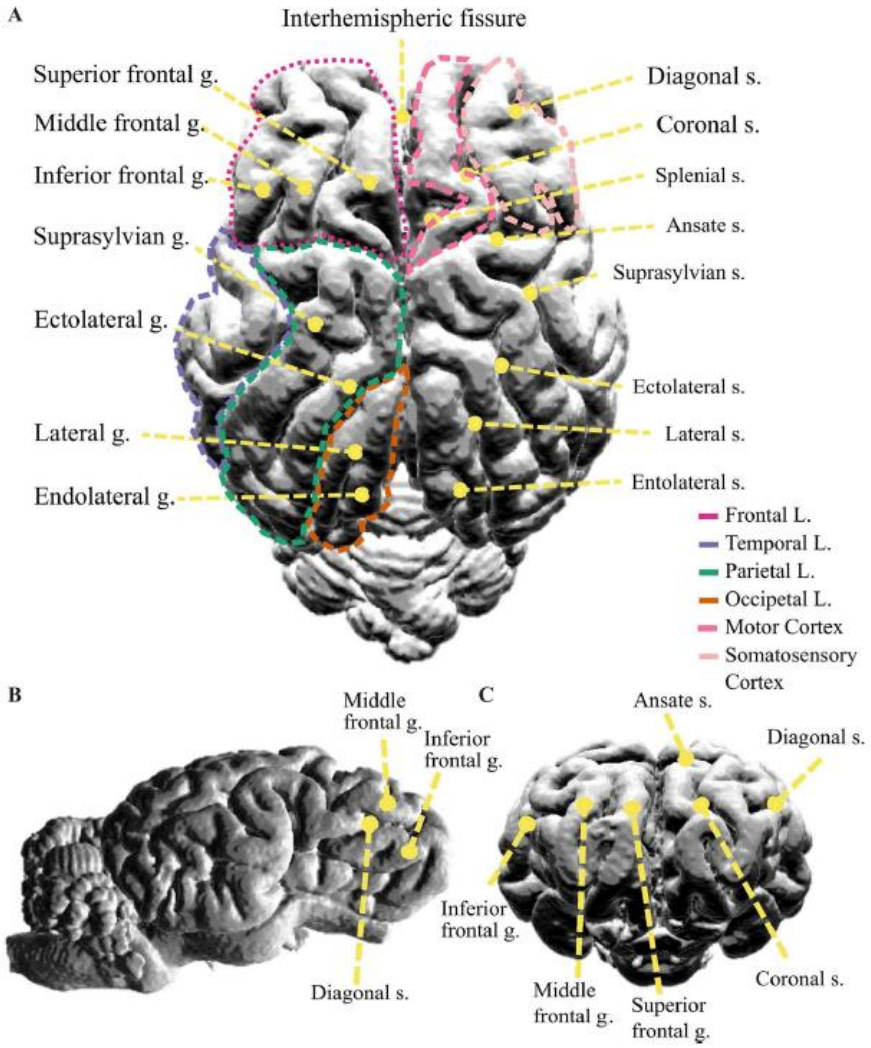

Figure 13 sheep brain sulci and giri. (A) Dorsal perspective detailing the various lobes (abbreviated 'L.'), sulci (abbreviated 's.'), and gyri (abbreviated 'g.') (B) The lateral perspective (C) Frontal perspective.[3, 7]

Dorsal surface

The dorsal surface of the brain is characterized by one transverse fissure (f.), the *sylvian*, one transverse sulcus, *cruciatus*, five longitudinal sulci, *coronalis*, *lateralis*, *entolateralis*, *ectolateralis* and *suprasylvius* and one diagonal sulcus.

The sulcus *entolateralis* lies close to the f. *longitudinalis* parallel to the s. *lateralis* with which can terminate joining it or end turning on the medial border of the hemisphere. The s. *lateralis* begin from the median border of the hemisphere and ends sometimes joining the r. *occipitotemporalis*. Anyway any reduction in length of s. *lateralis* is compensated by change in *ectolateralis*.

The s. *ectolateralis* is located between the lateralis and *suprasylvius* finishing cranially close to the s. *ansatus*. The caudal portion of s. *ectolateralis* reach the caudal pole of the hemisphere and its pathway is limited by the s. *suprasylvius*.

The *suprasylvius* is located close to the lateral border of the hemisphere and create an arch dorsally to the dorsal ramus of the *Sylvius* and approach or join the s. *ansatus*. The s. *suprasylvius* is characterized by a ventral ramus which is connected with s. *posticus*. The caudal ends of s. *suprasylvius* sometimes is made of a bifurcation which the dorsal ramus may join the s. *ectolateralis* while the ventral rami join the s. *posticus*[3, 67].

Rostral surface

The rostral surface is characterized by transverse and horizontal sulci. The transverse sulci are composed by *cruciatus* and *splenialis* sulci while the *coronalis*, *presylvius*, *diagonalis* sulci are part of the transverse sulci.

The *ansatus* sulcus extends from the *longitudinalis* fissure to the *suprasylvius* sulcus but not join it thanks to a curved gyrus.

The sulcus *coronalis* begin caudally to the sulcus *ansatus* and continues cranially with a lateral ramus which sometimes can be combined with a medial ramus. The lateral ramus lies parallel with the rostral end of the *presylvian* sulcus.

The olfactory sulcus is visible just when the olfactory tract and bulb are removed or depressed. The sulcus rostralis is located on the medial border of the hemisphere between the sulcus *ansatus* and the cranial end of the hemisphere.

The sulcus *diagonalis* is located laterally in the cranial part of the hemisphere. It begins close to the pars dorsalis of the sylvian fissure and extend to the s. *coronalis*. The sulcus *diagonalis* can be characterized sometimes by a ventral ramus[3, 67].

Lateral surface

The lateral surface is composed by horizontal fissures mostly with main exception of the *sylvius* fissure which is vertical. The *sylvius* fissure is composed by three portions, pars dorsalis which occasionally *bifurcaters*, pars anterior and the pars posterior. The pars dorsalis, is named processus *acuminis Krueg* and sometimes can be characterized by a bifurcation with two additional branches. The dorsal branch of this bifurcation can reach the s. *suprasylvius* while the ventral one can join the s. *diagonalis*. The ventral part of *sylvius* fissure is characterized by a caudal and a ventral branch which the latter reach the *rhinalis* sulci.

Presylvian sulcus begin ventrally to the ventral branch of the anterior ramus of the f. *Sylvius* and continues with a ventro-medal direction. It extends until the hemisphere rostral pole where joins a branch of s. *coronalis* or terminates in the rostral hemisphere extremity keeping a parallel line with the lateral ramus of s. *coronalis*.

The *suprasylvian* sulcus is the major sulcus in the lateral hemisphere surface. It also named arcuate sulcus thanks to its curved pathway which begins cranially to the pars dorsalis of the s, *Sylvius* and ends in the caudal pole of the hemisphere. It can be divided into a pars anterior, a pars media and a pars posterior. The pars anterior can be divided in two branches named anterior and ventral ramus. The pars media is in continue with to the s. *ansatus*. The pars anterior usually is characterized by a bifurcation in an anterior ramus and a ventral ramus.

The sulcus *diagonalis* is characterized by a ventromedial pathway. It begins caudally to the pars dorsalis of the *Sylvius* fissure and extend close to the s. *coronalis* ending close to the *Sylvius* fissure.

The sulcus *posticus* begins with its anterior ramus rostrally to the f. Sylvius and ends ventrally to the ventral ramus of pars media of s. *Suprasylvius*[3, 67].

The caudal surface

The caudal surface is characterized mainly by the s. *rhinalis* which can ends into the lateral surface and can continue joining the s. *suprasylvius* or with a more medial course into ending with the s. lateralis. These differences in the s. *rhinalis* ending depends on the *enxtension* of the *occipito-temporalis* sulcus. The *occipito-temporalis* sulcus pathway is located parallel and between the *retrosplenialis* and *rhinalis* sulci[67].

Sheep brain cortex

Cerebral cortex origins from the ependyma cells which migrate radially in association with the astroglial cells of the embryonic telencephalon. The cells are topographically organized in register, they have ventricular and subventricular progenitors and keep the same topographical relationships during the migration. This migration occurs at the same time and in the same way in both dorsolateral aspects of the lateral ventricles.

Every time neurons reach the cortical plate are separate in different layer, five layers structure in sheep [3]. The six-layer areas comprise a first peripheral layer, a second layer with sparse small pyramidal cells, a third layer of sparse large pyramidal cells, a fifth layer of gigantic pyramidal cells, and a sixth layer with spindle cells [68].

When the last neurons migrate from the ventricular plate to the surface the brain surface is smooth and giving to brain a similar aspect in all mammals during these early stages. Once all the neurons migration is completed gyrigenesis can begins forming all the gyri and sulci structures typical for each specie[69].

The motor cortex and somatosensory cortex lie in the frontal lobes parallel to the interhemispheric fissure, differently respect humans which the somatosensory cortex lies in the parietal lobes and are divided by central sulcus.

Another difference between human and sheep motor cortex is that sheep motor cortex is not divided in pre motor or supplemental motor cortex.

Sheep motor cortex is localized in the superior frontal gyrus of the frontal lobe and bounded in the rostral-caudal direction by the cruciate sulcus in the frontal lobe and the coronal sulcus in the medial

lateral direction. In literature has been observed great variability in the localization of sheep motor cortex area. For example the functional location in the motor cortex of the forelimb has been largely studied but the results shows different outcomes (figure 6)

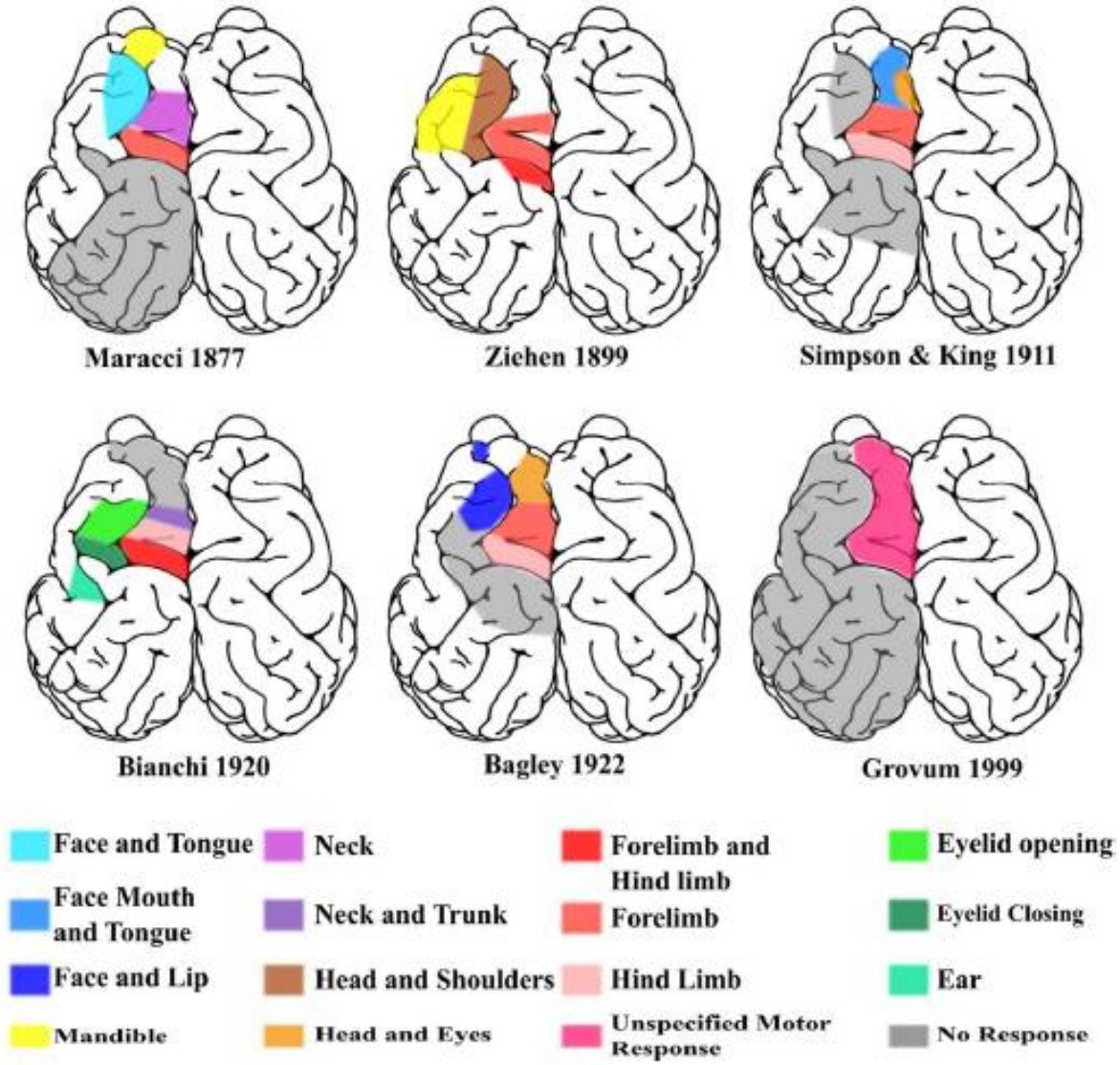

Figure 6 Sheep motor cortex. Functional mapping transcribed from six studies describing the sheep motor cortex using direct[3] showed by Maracci[7], Ziehen[2], Simpson[12], Bianchi[13], Bagley[14] and Grovum[15]

The cytoarchitectural studies of the motor cortex showed that main location of pyramidal cells is in superior frontal gyrus[70, 71]. Piramydal cells extended form superior frontal gyrus to the medial surface of the middle frontal gyrus [3]. The cells structure is different depending from the area

analysed. Indeed middle frontal gyrus is characterized by different cell structure with fewer, smaller pyramidal cells then the superior frontal gyrus.

The anterior extremities of the superior frontal gyrus is characterized by a lower concentration of pyramidal cells which gradual reduction at the limits of the superior frontal gyrus.

Electrical stimulation studies showed that pyramidal cells were located prevalent along both surfaces of the coronal sulcus and fewer on the medial face of the superior frontal gyrus.[70-72]

Cortical sensory area is located in the frontal lobe of the brain. The mechanosensory projections form the peripheral receptors to the sensory cerebral cortex in mammalian are species specific. In literature it is reported that the behavioural specializations are reflected by variants in mechanosensory projections, indeed fundamental is the relation between the animal and the environment and how the animal get information from and respond to it[9].

Ovine specie is characterized by two typical properties which are the predominance of ipsilateral then contralateral projections and the higher number of projections form the mouth area than the body and limbs one even though the huge difference between the surface body area represented.

The locations of projections to the sensory cerebral cortex is characterized by a somatotopic organization. The cortical area in question is located between the ansate, anterior suprasylvian, coronal and diagonal sulci. Important anatomical consideration is given to the coronal sulcus which is considered the board between the motor and the somatosensory area. (Figure 7)

The projections, connected mainly with the sensory thalamic nuclei, are divided in two major groups; ipsilateral and contralateral. Ipsilateral developed from the lips and nose area which are the predominantly represent on the sensory cortex. Cranially to the diagonal sulcus is located the teeth, dental pad and tongue to the region[9].

Projections from contralateral head and body are located on the anterior suprasylvian sulcus where in the posterior area are located the projections from the postcranial body.

Elecrophysiological studies have shown that the first somatosensory area (SI) is located between the coronal, diagonal, and the anterior suprasylvian sulcus while the second somatosensory area (SII) is located on the posterior wall of the suprasylvian sulcus.[72]

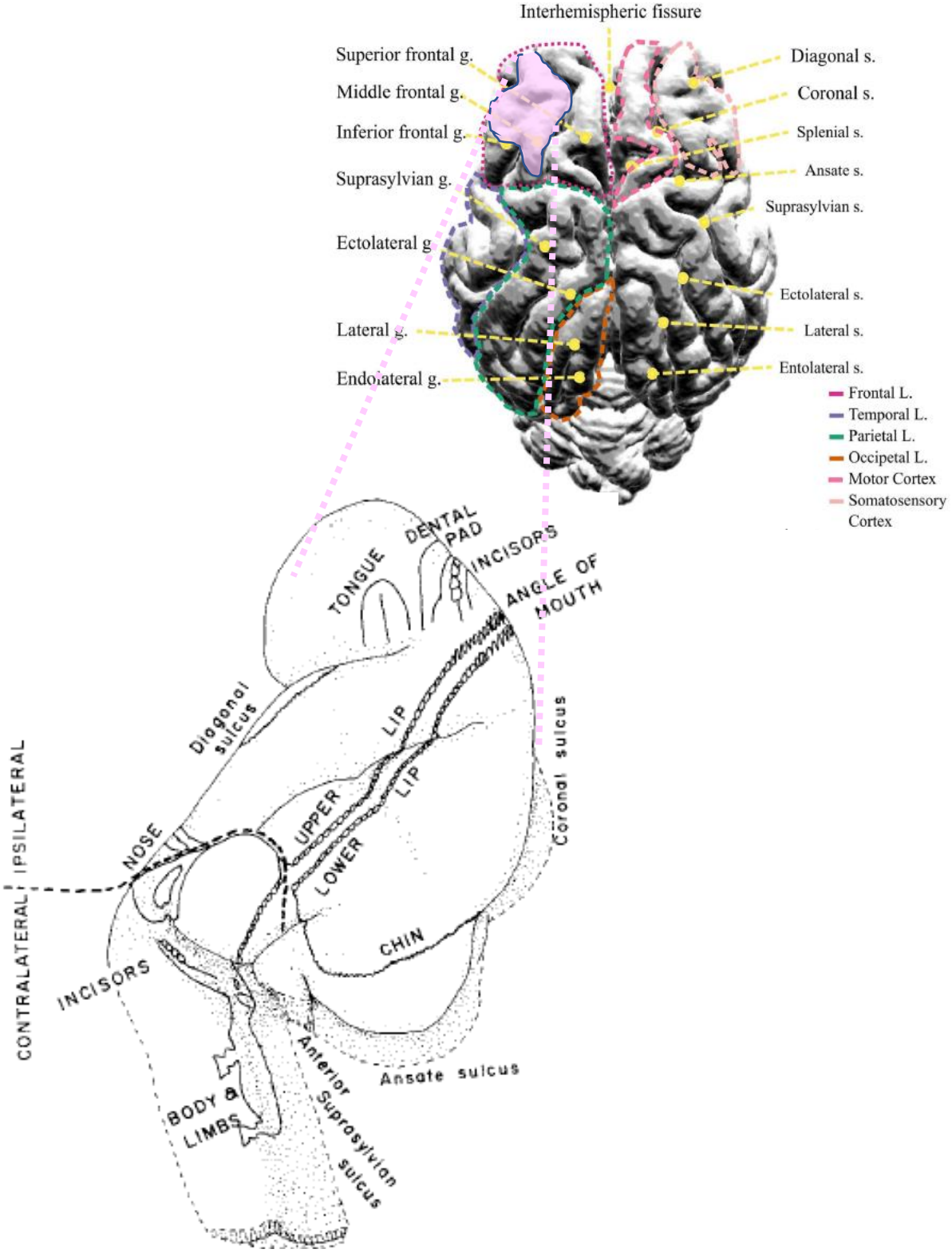

Figure 7 Sheep brain sensory cortex [9]

The vascular anatomy

Arterial brain anatomy

The carotid arteries arise by a common trunk from the right axillary artery and along his pathway it gives the thyroid and the laryngeal branch. Then it is divided in occipital artery and continues with the external carotid. Important for this specie is that the internal carotid is absent and in young animal is poorly developed[73] (figure 8).

The occipital artery supplies the anterior muscles of the head and a small meningeal branch placed under the dura mater enters the cranium by the *foramen lacerum basis cranii* passing into the condyloid foramen. This branch is bend on the back connecting with the anterior extremity of the collateral artery of the spine at the superior foramen of the atlas.

The occipital artery passing the condyloid foramen sending into the parieto-temporal canal a small branch dedicated to the dura mater. Along its pathway the occipital artery joins the *rete mirabile* once entered into the cranial cavity

The external carotid artery finishes with the superficial temporal and internal maxillary artery. Along his route gives the pharyngeal artery, the lingual artery, the maxillary artery and the posterior auricular artery. The stylomastoid arteriole arises from the posterior auricular artery followed by the concho-muscular branches and a mastoid artery which enters via the temporo-parietal canal, giving two branches. The external branch is dedicated to the temporal muscle and then joins deeper with the temporal arteries. The internal branch is considered as a meningeal artery and goes to the falx cerebri and the tentorium cerebri.

A later branch of external carotid is a small maxillo-muscular artery which is divided in the internal pterygoid and the subcutaneous muscles.

The superficial temporal artery is the last bifurcation of the external carotid artery and it is divided in three branches which are the anterior auricular artery, the middle temporal artery and the transverse artery of the face.

The internal maxillary artery doesn't pass the subsphenoidal canal because this passage in sheep does not exist, and form this arise different branches: inferior dental artery, the spheno-spinous artery which enter via oval foramen in the cranium cavity and forms the rete mirabile. Another

branch from the internal maxillary artery is the posterior deep temporal artery, the interior deep temporal artery, the buccal artery, the ophthalmic artery. The ophthalmic artery in sheep is a long artery, longer than in the other animals which pass the orbital foramen dividing in a supra-orbital branch and a fasciculus of muscular and ciliary arteries.

As note before the rete mirabile is characterized by three originating arteries. One of these, the spheno-spinous artery, arises from the internal maxillary at the same point as the inferior dental artery, and enters cranium through foramen ovale. The other two originating arteries arise from internal maxillary in common with the ophthalmic artery and pass backwards through a supra-sphenoidal canal.

The rete mirabile is a small area located under the dura mater, on the side of the sella Turcica, within the superior maxillary nerve. It is composed by a multitude of fine arterial divisions which anastomose with each other. Its inferior extremity, passing into the supra-sphenoidal canal, receives the generating arteries. The posterior extremity, covered by the clinoid process, is in communication with the spheno-spinous artery. Its middle area crosses the dura mater and gives a large posterior branch going to the interpeduncular fossa. After this branch the internal carotid continues ventrally to the optic tract and reach the optic chiasma where is then divided in the middle cerebral artery and then it continues as anterior cerebral artery. The anterior cerebral artery continues cranially reaching the longitudinal fissure anastomosing with the opposite one forming a fine vessels network replacing the anterior communicating artery. The anterior cerebral artery terminates dividing into the corpus callosum artery and into a marginal artery. The posterior communicating arteries makes a semicircle around the midbrain anastomosing each other cranially to the pons. These arteries are much larger in sheep than in other species as results of the brain blood supply is made mainly by carotids in ovine.[74, 75]

The vertebral artery contribution in the brain arterial network is absent. The basilar artery makes a small anastomosis with the vertebral one and reducing in caliber reaching the vertebral artery.

In light of these anatomical consideration the circle of Willis, which is important as potential collateral pathway at the base of brain, in ovine animals is composed by the internal carotid arteries along its course, cranially by anterior fine plexus of vessels, caudally by the posterior communicating artery which is a posterior branch of internal carotid artery and by the basilar artery.[76]

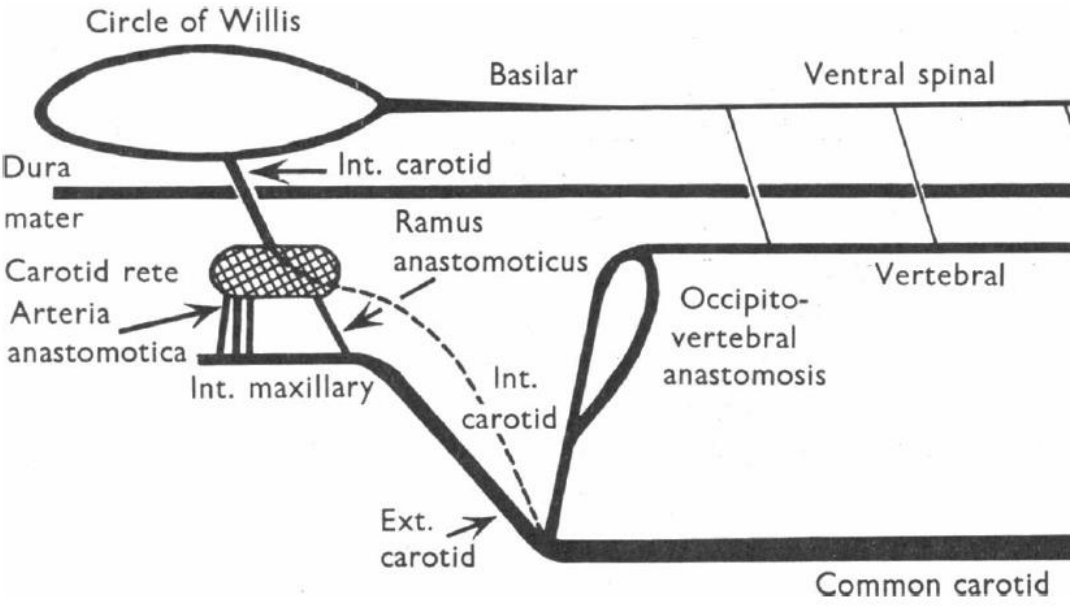

Figure 8 Ovine cerebral circulation diagram. The dotted line indicates that the internal carotid does not persist in the adult[2, 4]

Venous system

The dura mater is composed by sinuses which are vascular spaces situated between the meninges or meninx and bones which form the walls of the cerebro-spinal sheath and excavated on the inner surface of these bones. They are composed by an epithelial layer which lies on dura mater meninx or on the bone tissue. The sinuses are opened without valves and are characterized by *trabeculae* or *Willissi cordae* which have a vale-like shape and a functional role to prevent reverse blood flows [77]

The main brain sinuses of the dura mater are four and are the falx cerebri sinus, two cavernous sinuses and the ventral occipital sinus.

The sinus of the falx cerebri, also known as dorsal sagittal sinus, collects blood from the dorsal part of the brain and it is located in the *falx cerebri,* begin close to the *crista galli* process of the ethmoid bone and run backwards and finish on the internal occipital protuberance. It received the ethmoidal veins cranially, the dorsal cerebral veins laterally and the diploic and meningeal veins dorsally.

Dorsal cerebral veins are connected to the dorsal sagittal sinus via lateral dorsal cerebral veins expansions containing the arachnoid granulations for cerebrospinal fluid drainage.

The dorsal sagittal sinus received even the straight sinus and it is characterized by a bifurcation, named confluence of sinus, in the bilateral transverse sinus. The straight sinus is created from the splenium of *corpus callosi* by the confluence of the great cerebral veins ventrally ant the vein of *corpus callosum* dorsally. It drains in the dorsal sagittal sinus before the formation of the confluence sinuses.

Transverse sinus is located inside the *tentorium of cerebellum* and it is the *continuum* of the dorsal sagittal sinus. This sinus is characterized by a transverse groove and terminates dividing in the temporal and sigmoid sinuses.

The temporal sinus is larger than sigmoid one and continue in a rostroventral direction. It is located in the temporal canal and it emerged as the emissary vein of the retroarticular foramen and joined maxillary vein and pterygoid plexus. The sigmoid sinus continues in a caudoventral direction, joined the emissary vein of the condylar foramen. Ifs branches finally drains into the occipital vein and basilar sinus[78].

The cavernous sinuses are part of the ventral sinus system with the ventral petrosal sinus and the ventral occipital sinus. The cavernous sinuses are characterized by a plexiform structure and are located right and left occupying the internal face of the sphenoid bone, close to the *sella turcica*. They spread from the *foramen orbitorotundum* to the *dorsum sellae*. This sinus empties via emissary vein to extracranial pterygoid plexus while caudally continue with the central petrosal sinus and before the jugular foramen it makes anastomosis with the latter sinus.

The ventral occipital sinus is located close to the occipital *foramen magnum*. Cranially this sinus is linked with the posterior extremity of the cavernous sinuses while caudally they continue with the spinal sinuses. The ventral occipital sinus indeed open into the internal vertebral venous plexus and into the emissary vein of *hypoglossal* vein. The *hypoglossal* vein and the emissary veins coming from the *jugular foramen* join together forming a plexus structure which in human is described as anterior condylar confluent.[43]

In addition to these main sinuses other minor sinuses are presents in the sheep brain. Important is consider the temporal sinus which is create by the cranial union of the transverse sinuses. The

temporal sinus enter the temporal meatus and then is divided in two different vessels which emerged from the retroarticular foramen joining the maxillary vein.

On the brain surface the venous system creates a rich network with the main branches go into the *dura mater* sinuses. Mainly these reach the transverse sinus but few of these gain the cavernous sinuses while the *cerebellum* and *medulla ablongata* veins passes to the petrosal and occipital sinuses.

They join into one of the main internal brain vein, *Galeni vena*, which is located dorsally to the *corpus callosum*, receives the superficial veins of the internal hemispheres face and reach the interlobular fissures entering into the back of the middle sinus.

The median and transverse sinuses effluent pathway is made by parieto-temporal confluents which are located in canals along the mastoid artery. These commences terminates at level of the supra-condyloid eminence and open in the temporal veins, giving a branch which pass the *foramen lacerum.*

The pterygoid veins and the anterior radicles of the occipital veins drain via the subsphenoidal confluents which develop from the sphenoid bone and basilar process to the condyloid fossa. They are in communication with the cavernous sinus in their middle portion. Anteriorly they finished with a dead end and caudally communicate with the occipital sinuses via the condyloid foramina.

The common jugular vein is the major vessel in the ovine neck/head anatomy characterized by circa 7.4 mm in diameter followed by the internal jugular vein of 4.4 mm. The proper larger brain veins in sheep decrease in dimensions with the transverse sinus characterized by circa 2.5 mm of diameter, dorsal sagittal sinus with 2.4 mm in the caudal portion reaching 1.2 mm on the distal section. The cruciate sulcal vein is reported with 1.1 mm in diameter[4].
Dorsal sagittal sinus is the longer venous brain vessel with a length of circa 6,5 cm, followed by the temporal sinus with 2,5 cm and the straight sinus with 9 mm of length[78].
In relation with the motor cortex the dorsal sagittal sinus lies close to the midline, the motor cortex is reported to be drained by major draining venous pathway coursing along the vertex of the brain in the midline, forming just behind the frontal sinus anteriorly to join the confluence of sinuses posteriorly. The sensory area located more laterally than the motor one is more drained by the dorsal cerebral veins [79]. (figure 9)

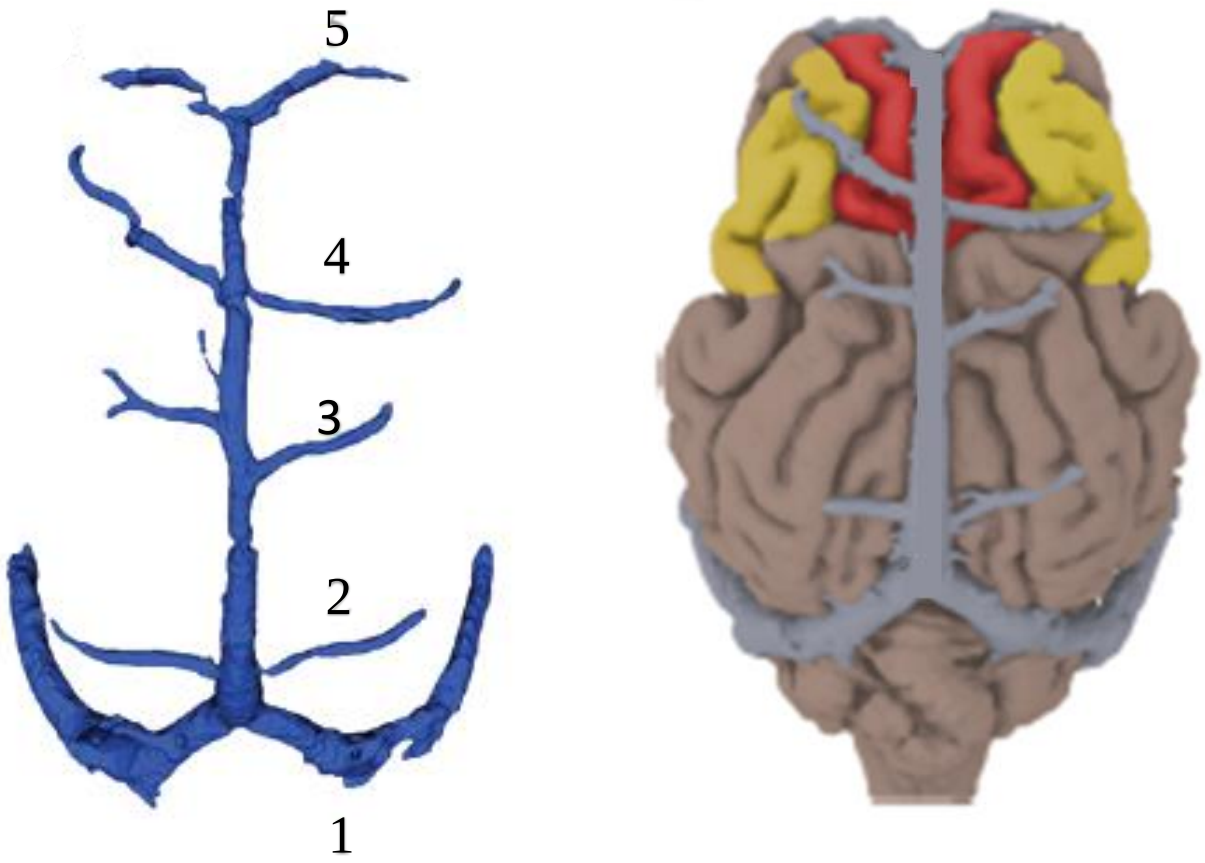

Figure 9 Dorsal venous brain vessels

A) Schematic presentation on the dorsal venous brain ramification. 1) transverse sinus 2) Straight sinus 3) Dorsal cerebral veins 5) Ethmoid veins [4]

B) Vascular anatomy and motor, sensitive cortex. The motor cortex is presented by the red area while the sentive cortex by the yellow one[8]

1. Pelekanos M, Leinenga G, Odabaee M, Saifzadeh S, Steck R, Götz J: **Establishing sheep as an experimental species to validate ultrasound-mediated blood-brain barrier opening for potential therapeutic interventions**. *Theranostics* 2018, **8**(9):2583-2602.
2. Ziehen T: **Ein Beitrag zur Lehre von den Beziehungen zwischen Lage und Function im Bereich der motorischen Region der Grosshirnrinde mit spezieller Rucksicht auf das Rindenfeld des orbicularis oculi.** . In., vol. Phys. Abth 17: Arch. f. Anat. u. Physiol.; 1899.
3. John SE, Lovell TJH, Opie NL, Wilson S, Scordas TC, Wong YT, Rind GS, Ronayne S, Bauquier SH, May CN *et al*: **The ovine motor cortex: A review of functional mapping and cytoarchitecture**. *Neurosci Biobehav Rev* 2017, **80**:306-315.
4. Oxley TJ, Opie NL, Rind GS, Liyanage K, John SE, Ronayne S, McDonald AJ, Dornom A, Lovell TJH, Mitchell PJ *et al*: **An ovine model of cerebral catheter venography for implantation of an endovascular neural interface**. *J Neurosurg* 2018, **128**(4):1020-1027.
5. Schmidt M: **Comparative anatomy of the pig brain - An integrative magnetic resonance imaging (MRI) study of the porcine brain with special emphasis on the external morphology of the cerebral cortex**. Justus-Liebig-Universität Gießen; 2015.
6. Manunta ML, Evangelisti MA, Burrai GP, Columbano N, Ligios C, Varcasia A, Scala A, Sanna Passino E: **Magnetic resonance imaging of the brain and skull of sheep with cerebral coenurosis**. *Am J Vet Res* 2012, **73**(12):1913-1918.
7. Maracci A: **Determinazione della zona eccitabile nel cervello pecorino**. In. Milano: Arch. ital. per le mal. nerv.; 1877.
8. Oxley TJ, Opie NL, John SE, Rind GS, Ronayne SM, Wheeler TL, Judy JW, McDonald AJ, Dornom A, Lovell TJ *et al*: **Minimally invasive endovascular stent-electrode array for high-fidelity, chronic recordings of cortical neural activity**. *Nat Biotechnol* 2016, **34**(3):320-327.
9. Johnson JI, Rubel EW, Hatton GI: **Mechanosensory projections to cerebral cortex of sheep**. *J Comp Neurol* 1974, **158**(1):81-107.
10. **Preclinical testing of Neural Prostheses**. In: *Neurobionics: The Biomedical Engineering of Neural Prostheses.* edn.
11. McCreery D: **Preclinical testing of Neural Prostheses**. In: *Neurobionics: The Biomedical Engineering of Neural Prostheses.* edn.; 2016.
12. Simpson SK, J. Luella: **Localisation of the motor area in the sheep**. In.; 1911.
13. Bianchi L: **La Meccanica Del Cervello e La Funzione Dei Lobi Frontali**. In.: Bocca; 1920: 432.
14. BAGLEY C, JR.: **CORTICAL MOTOR MECHANISM OF THE SHEEP BRAIN**. *Archives of Neurology & Psychiatry* 1922, **7**(4):417-453.
15. Grovum WL, Gonzalez JS: **Electrical stimulation of the medial frontal lobe elicits a pattern of body movements in sheep**. *Brain Res* 1999, **851**(1-2):252-253.
16. DiLuca M, Olesen J: **The cost of brain diseases: a burden or a challenge?** *Neuron* 2014, **82**(6):1205-1208.
17. Olesen J, Gustavsson A, Svensson M, Wittchen HU, Jönsson B, group Cs, Council EB: **The economic cost of brain disorders in Europe**. *Eur J Neurol* 2012, **19**(1):155-162.
18. Sobocki P, Lekander I, Berwick S, Olesen J, Jönsson B: **Resource allocation to brain research in Europe (RABRE)**. *Eur J Neurosci* 2006, **24**(10):2691-2693.
19. Ekman M, Westphal M: **Cost of brain tumour in Europe**. *Eur J Neurol* 2005, **12 Suppl 1**:45-49.
20. Pugliatti M, Sobocki P, Beghi E, Pini S, Cassano GB, Altamura AC, Pozzoli S, Rosati G, Group CoDotBiES: **Cost of disorders of the brain in Italy**. *Neurol Sci* 2008, **29**(2):99-107.
21. Hanif F, Muzaffar K, Perveen K, Malhi SM, Simjee SU: **Glioblastoma Multiforme: A Review of its Epidemiology and Pathogenesis through Clinical Presentation and Treatment**. *Asian Pac J Cancer Prev* 2017, **18**(1):3-9.
22. Omuro A, DeAngelis LM: **Glioblastoma and other malignant gliomas: a clinical review**. *JAMA* 2013, **310**(17):1842-1850.
23. Alphandéry E: **Glioblastoma Treatments: An Account of Recent Industrial Developments**. *Front Pharmacol* 2018, **9**:879.

24. Louis DN, Perry A, Reifenberger G, von Deimling A, Figarella-Branger D, Cavenee WK, Ohgaki H, Wiestler OD, Kleihues P, Ellison DW: **The 2016 World Health Organization Classification of Tumors of the Central Nervous System: a summary**. *Acta Neuropathol* 2016, **131**(6):803-820.
25. Buonerba C, Di Lorenzo G, Marinelli A, Federico P, Palmieri G, Imbimbo M, Conti P, Peluso G, De Placido S, Sampson JH: **A comprehensive outlook on intracerebral therapy of malignant gliomas**. *Crit Rev Oncol Hematol* 2011, **80**(1):54-68.
26. Jahangiri A, Chin AT, Flanigan PM, Chen R, Bankiewicz K, Aghi MK: **Convection-enhanced delivery in glioblastoma: a review of preclinical and clinical studies**. *J Neurosurg* 2017, **126**(1):191-200.
27. Jellison BJ, Field AS, Medow J, Lazar M, Salamat MS, Alexander AL: **Diffusion tensor imaging of cerebral white matter: a pictorial review of physics, fiber tract anatomy, and tumor imaging patterns**. *AJNR Am J Neuroradiol* 2004, **25**(3):356-369.
28. Wu JS, Zhou LF, Tang WJ, Mao Y, Hu J, Song YY, Hong XN, Du GH: **Clinical evaluation and follow-up outcome of diffusion tensor imaging-based functional neuronavigation: a prospective, controlled study in patients with gliomas involving pyramidal tracts**. *Neurosurgery* 2007, **61**(5):935-948; discussion 948-939.
29. Janowski M: **Experimental Neurosurgery in Animal Models**. In.: Humana Press; 2016: 255.
30. Sun T, Hevner RF: **Growth and folding of the mammalian cerebral cortex: from molecules to malformations**. *Nat Rev Neurosci* 2014, **15**(4):217-232.
31. Finnie J: **Animal models of traumatic brain injury: a review**. *Aust Vet J* 2001, **79**(9):628-633.
32. Lind NM, Moustgaard A, Jelsing J, Vajta G, Cumming P, Hansen AK: **The use of pigs in neuroscience: modeling brain disorders**. *Neurosci Biobehav Rev* 2007, **31**(5):728-751.
33. Sauleau P, Lapouble E, Val-Laillet D, Malbert CH: **The pig model in brain imaging and neurosurgery**. *Animal* 2009, **3**(8):1138-1151.
34. Regelsberger J: **Surgery of the Brain and Spinal Cord in a Porcine Model**. In: *Experimental Neurosurgery in Animal Models.* edn. Edited by Janowski M. New York, NY: Springer New York; 2016: 165-173.
35. Campbell RG, Johnson RJ, King RH, Taverner MR: **Effects of gender and genotype on the response of growing pigs to exogenous administration of porcine growth hormone**. *J Anim Sci* 1990, **68**(9):2674-2681.
36. Bjarkam CR, Cancian G, Larsen M, Rosendahl F, Ettrup KS, Zeidler D, Blankholm AD, Østergaard L, Sunde N, Sørensen JC: **A MRI-compatible stereotaxic localizer box enables high-precision stereotaxic procedures in pigs**. *J Neurosci Methods* 2004, **139**(2):293-298.
37. Perentos N, Nicol AU, Martins AQ, Stewart JE, Taylor P, Morton AJ: **Techniques for chronic monitoring of brain activity in freely moving sheep using wireless EEG recording**. *J Neurosci Methods* 2017, **279**:87-100.
38. Martini L, Fini M, Giavaresi G, Giardino R: **Sheep model in orthopedic research: a literature review**. *Comp Med* 2001, **51**(4):292-299.
39. Dai JX, Ma YB, Le NY, Cao J, Wang Y: **Large animal models of traumatic brain injury**. *Int J Neurosci* 2018, **128**(3):243-254.
40. Karageorgos L, Hein L, Rozaklis T, Adams M, Duplock S, Snel M, Hemsley K, Kuchel T, Smith N, Hopwood JJ: **Glycosphingolipid analysis in a naturally occurring ovine model of acute neuronopathic Gaucher disease**. *Neurobiol Dis* 2016, **91**:143-154.
41. Opdam HI, Federico P, Jackson GD, Buchanan J, Abbott DF, Fabinyi GC, Syngeniotis A, Vosmansky M, Archer JS, Wellard RM *et al*: **A sheep model for the study of focal epilepsy with concurrent intracranial EEG and functional MRI**. *Epilepsia* 2002, **43**(8):779-787.
42. Boltze J, Förschler A, Nitzsche B, Waldmin D, Hoffmann A, Boltze CM, Dreyer AY, Goldammer A, Reischauer A, Härtig W *et al*: **Permanent middle cerebral artery occlusion in sheep: a novel large animal model of focal cerebral ischemia**. *J Cereb Blood Flow Metab* 2008, **28**(12):1951-1964.
43. Hoffmann A, Stoffel MH, Nitzsche B, Lobsien D, Seeger J, Schneider H, Boltze J: **The ovine cerebral venous system: comparative anatomy, visualization, and implications for translational research**. *PLoS One* 2014, **9**(4):e92990.

44. Grisham W: **Resources for teaching Mammalian neuroanatomy using sheep brains: a review**. *J Undergrad Neurosci Educ* 2006, **5**(1):R1-6.
45. Hamamcioglu MK, Hicdonmez T, Tiryaki M, Cobanoglu S: **A laboratory training model in fresh cadaveric sheep brain for microneurosurgical dissection of cranial nerves in posterior fossa**. *Br J Neurosurg* 2008, **22**(6):769-771.
46. Altunrende ME, Hamamcioglu MK, Hıcdonmez T, Akcakaya MO, Bırgılı B, Cobanoglu S: **Microsurgical training model for residents to approach to the orbit and the optic nerve in fresh cadaveric sheep cranium**. *J Neurosci Rural Pract* 2014, **5**(2):151-154.
47. Hicdonmez T, Parsak T, Cobanoglu S: **Simulation of surgery for craniosynostosis: a training model in a fresh cadaveric sheep cranium. Technical note**. *J Neurosurg* 2006, **105**(2 Suppl):150-152.
48. Kamp MA, Knipps J, Steiger HJ, Rapp M, Cornelius JF, Folke-Sabel S, Sabel M: **Training for brain tumour resection: a realistic model with easy accessibility**. *Acta Neurochir (Wien)* 2015, **157**(11):1975-1981; discussion 1981.
49. Stelnicki EJ, Vanderwall K, Hoffman WY, Harrison MR, Glowacki J, Longaker MT: **A new in utero sheep model for unilateral coronal craniosynostosis**. *Plast Reconstr Surg* 1998, **101**(2):278-286.
50. Noden DM, de Lahunta A: **The embryology of domestic animals : developmental mechanisms and malformations**. In. Baltimore (Md.): Williams and Wilkins, 1985.; 1985.
51. Harris HA: **The Foetal Growth of the Sheep**. *J Anat* 1937, **71**(Pt 4):516-527.
52. Grova M, Lo DD, Montoro D, Hyun JS, Chung MT, Wan DC, Longaker MT: **Models of cranial suture biology**. *J Craniofac Surg* 2012, **23**(7 Suppl 1):1954-1958.
53. Chauveau A, Arloing S: **The Comparative Anatomy of the Domesticated Animals**. In.; 1905: 1084.
54. Barone R: **Anatomie comparée des mammifères domestiques : Tome 6, Neurologie I.**; 2010.
55. Keir J: **Why do we have paranasal sinuses?** *J Laryngol Otol* 2009, **123**(1):4-8.
56. Awaad AS, Abdel Maksoud MKM, Fathy MZ: **Surgical anatomy of the nasal and paranasal sinuses in Egyptian native sheep (Ovis aries) using computed tomography and cross sectioning**. *Anat Histol Embryol* 2019, **48**(4):279-289.
57. Skitarelić N, Mladina R: **Lamb's head: The model for novice education in endoscopic sinus surgery**. *World J Methodol* 2015, **5**(3):144-148.
58. Valbonetti L, Berardinelli P, Scarano A, Piattelli A, Mattioli M, Barboni B, Vulpiani MP, Muttini A: **Translational value of sheep as animal model to study sinus augmentation**. *J Craniofac Surg* 2015, **26**(3):737-740.
59. Farke AA: **Frontal sinuses and head-butting in goats: a finite element analysis**. *J Exp Biol* 2008, **211**(Pt 19):3085-3094.
60. **Computed tomography and gross anatomical studies of the orbital cavity of the baladi goat (Capra hircus).** *Alexandria Journal of Veterinary Sciences* 2016, **51**(2):74-81.
61. Bernhard CG, Kolmodin GM, Meyerson BA: **On the prenatal development of function and structure in the somesthetic cortex of the sheep**. *Prog Brain Res* 1967, **26**:60-77.
62. Budday S, Steinmann P, Kuhl E: **The role of mechanics during brain development**. *J Mech Phys Solids* 2014, **72**:75-92.
63. Van Essen DC: **Cerebral Cortical Folding Patterns in Primates: Why They Vary and What They Signify**. In., vol. 4: Evolution of Nervous System; 2007: 267-276.
64. Kriegstein A, Noctor S, Martínez-Cerdeño V: **Patterns of neural stem and progenitor cell division may underlie evolutionary cortical expansion**. *Nat Rev Neurosci* 2006, **7**(11):883-890.
65. Armstrong E, Curtis M, Buxhoeveden DP, Fregoe C, Zilles K, Casanova MF, McCarthy WF: **Cortical gyrification in the rhesus monkey: a test of the mechanical folding hypothesis**. *Cereb Cortex* 1991, **1**(5):426-432.
66. Zilles K, Palomero-Gallagher N, Amunts K: **Development of cortical folding during evolution and ontogeny**. *Trends Neurosci* 2013, **36**(5):275-284.
67. Landrace FL: **The major and minor sulci of the brain of the sheep**. In., vol. 30: Ohio Journal of Science; 1930: 36-49.
68. Glatzle M, Hoops M, Kauffold J, Seeger J, Fietz SA: **Development of Deep and Upper Neuronal Layers in the Domestic Cat, Sheep and Pig Neocortex**. *Anat Histol Embryol* 2017, **46**(4):397-404.

69. Jones EG, Peters A: **Cerebrail Cortex. Comparative Structure and Evolution of Cerebrail Cortex, Part II**, vol. 8B; 1990.
70. Rose JE: **A cytoarchitectural study of the sheep cortex**. 1942, **76**(1):1-55.
71. Simpson S, King JL: **LOCALISATION OF THE MOTOR AREA IN THE SHEEP**. 1911, **4**(1):53-65.
72. Dinopoulos A, Karamanlidis AN, Papadopoulos G, Antonopoulos J, Michaloudi H: **Thalamic projections to motor, prefrontal, and somatosensory cortex in the sheep studied by means of the horseradish peroxidase retrograde transport method**. *J Comp Neurol* 1985, **241**(1):63-81.
73. BALDWIN BA, BELL FR: **The anatomy of the cerebral circulation of the sheep and ox. The dynamic distribution of the blood supplied by the carotid and vertebral arteries to cranial regions**. *J Anat* 1963, **97**:203-215.
74. Kapoor K, Kak VK, Singh B: **Morphology and comparative anatomy of circulus arteriosus cerebri in mammals**. *Anat Histol Embryol* 2003, **32**(6):347-355.
75. Deepthi S, Suseelamma D, Pramod Kumar D, Saradadevi SS, Subhadradevi V: **Comparative study of formation of circle of Willis in human and sheep brain**. In., vol. 65: Journal of the Anatomical Society of India; 2016: S16-S19.
76. Ashwini C, Shubha RA, Jayanthi KS: **Comparative anatomy of the circle of Willis in man, cow, sheep, goat and pig**. In*: 2008*; 2008.
77. Schmutz HK: **The chordae Willisii in the superior sagittal sinus: morphology and classification**. *Acta Anat (Basel)* 1980, **108**(1):94-97.
78. Merih Hazıroğl R, Takçiz I, Çiftçi N: **Gross anatomy of dural sinuses in sheep**. In., vol. 41: A.Ü. Vet. Fak. Derg; 1994: 533 - 539.
79. Opie NL, John SE, Rind GS, Ronayne SM, Wong YT, Gerboni G, Yoo PE, Lovell TJH, Scordas TCM, Wilson SL *et al*: **Focal stimulation of the sheep motor cortex with a chronically implanted minimally invasive electrode array mounted on an endovascular stent**. *Nat Biomed Eng* 2018, **2**(12):907-914.

Aim of the study

The topics addressed in the chapter 1 of the present thesis deal with the animal model analysis for EDEN2020 project.

From the analysis of EDEN2020 aims the focus has been shifted to the different animal models used in research analysing large animal models as ideal translational model for the project. Relevance has been given to the skull and brain morphology in order to simulate perfectly the clinical scenario composed by imaging study and surgical scenario. With a view to obtain the finest translational model from bench to bedside sheep has been selected thanks to the large gyrencephalic human like brain, able to provide important and improved translational clinical data related to the neuroanatomical structures compared to rodent models.

Three different analysis on sheep as animal model have been included in this doctorate thesis. All of these analysis have been prepared and presented as journal papers in the following chapter 2.

I. The first concerns the development and validation of the head frame system helmet for ovine species. The objective of the work was to develop the design and validate a new CT/MRI compatible head frame system and software (manuscript under submission).
II. The second study is related to the MRI and DTI analysis in sheep. The aim of the work was to establish the in vivo tractography atlas in order to reconstruct the white matter fibre bundles of the ovine brain, underling with DTI tractography reconstruction of the major white matter tracts as Corticospinal Tract (CST), Corpus Callosum (CC), Fornix (FO), visual pathway (VP) and occipitofrontal fascicle (OF) (manuscript published, frontiers in veterinary science DOI: 10.3389/fvets.2019.00345).
III. A further white matter related study included in this PhD thesis concerns the microscopic white matter samples analysis. White matter samples have been studied via FIB-SEM microscope and 3D reconstruction of axons bundles. In order to analyse the same structures find during DTI analysis CC, FO has been sampled. The CST has been sampled at level of corona radiata (CR) for practical issue indeed CST originates from the cerebral cortex and travels via CR, posterior limb of the internal capsule (PLIC), and pons (manuscript under submission).

Since the doctorate thesis consist of studies on different topics but all gathered in the EDEN2020 aims, the purpose of this work was to bring new information into the scientific literature about sheep as animal model in neuroscience and neurosurgical scenario. The data acquired during the works presented in my PhD has been produced following the EDEN2020 project which proceed going along the primary aim on a new catheter development as the main project goal in an integrated technology platform for minimally invasive neurosurgery.

Chapter 2

Research Papers

The papers published/submitted were reported keeping the reference style indicated by the guidelines of each Journal

Development and *in-vivo* Assessment of a Novel MRI-Compatible Stereotactic System for the Ovine Animal Model

(*The manuscript reported here is ready to be submitted)*

Development and *in-vivo* Assessment of a Novel MRI-Compatible Stereotactic System for the Ovine Animal Model

M. Trovatelli[a], S. Brizzola[b], D. D. Zani[b], M. Riva[c],
A. Castellano[d],
M. Woolley[e], P. Moore[e], R. Terblanche[e], D. Johnson[e],
F. Acocella[a], F. Rodriguez y Baena[f], L. Bello[c],
A.Falini[d], R. Secoli[f,*]

[a]Department of Health, Animal Science and Food Safety, Università degli Studi di Milano, Italy

[b]Department of Veterinary Medicine, Università degli Studi di Milano, Milan, Italy

[c]Unit of Oncological Neurosurgery Humanitas Clinical and Research Center IRCCS Rozzano - Italy

[d]Neuroradiology Unit and C.E.R.M.A.C., Vita-Salute San Raffaele University and IRCCS Ospedale San Raffaele, Milano, Italy

[e]Renishaw Plc - UK

[f]Department of Mechanical Engineering, Imperial College London - UK

Abstract

Background. The brain of sheep has primarily been used in neuroscience as an animal model because of its similarity to the human brain, in particular if compared to other models such as the lissencephalic rodent brain. Moreover, their docile behaviour en- ables easy handling of the animal, as well as post-surgical management with respect to other animal models (e.g. mouse, minipigs, etc.). Their brain size also makes sheep an ideal model for the development of neurosurgical techniques using conventional clinical CT/MRI scanners, and stereotactic systems for neurosurgery.

New Method. In this study, we present the design and validation of a new CT/MRI compatible head frame for the ovine model and software, with its assessment under two real clinical scenarios.

Results. Ex-vivo and *in-vivo* trial results report an average linear displacement of the ovine head frame during conventional surgical procedures of 0.81*mm* for ex-vivo trials and 0.68*mm* for *in-vivo* tests, respectively.

Comparison with Existing Methods. Only a few stereotactic head frame systems for the ovine model have been used in research to date, and these missed key features for translation to other clinical settings, in particular due to the lack of MRI compatibility.
Conclusions. The *ex-vivo* and *in-vivo* trial results demonstrate the robustness of the head frame system and its suitability to be employed within a real clinical setting.

Keywords: sheep model. stereotactic. head frame. animal model.

---

*Corresponding author

Email addresses: marco.trovatelli@unimi.it (M. Trovatelli), f.rodriguez@imperial.ac.uk (F. Rodriguez y Baena), r.secoli@imperial.ac.uk (R. Secoli)

Preprint submitted to Journal of Neuroscience Methods August 8, 2019

1. Introduction

Over the past three decades, translational biomedical researches have seen the use of ovine models for different applications, ranging from orthopedics [1], traumatic brain in- jury studies [2], and neurological diseases [3], to more specific studies such for Alzheimer's disease [4] and epilepsy [5]. Both the large size of the ovine brain as well as anatomical features of the skull mean the ovine model is an ideal candidate in conventional stereo- tactic techniques for deep brain stimulation, as shown by Stypulkowski et al. for the thalamus [6], and more recently, on the hippocampus [7]. Stereotactic methods have been widely used in other large animal models such as the pig. For instance, Bjarkam et al.[8] developed a stereotactic procedure which enables MRI guided isocentric stereo- taxy, and White et al.[9] established a method for stereotactic delivery of catheters and electrodes for reaching deep targets in the brain. Stereotactic procedures have been devel- oped even in sheep for neurosurgical purposes, such as in Oheim et al. [10] for the intra-cerebroventricular application of leptin into the lateral ventricle. The stereotactic surgical approach has also been used for continuous monitoring of the electroencephalographic activity through the insertion of needles, as shown by Perentos et al. [11]. Despite these studies, to our knowledge, only a few stereotactic head frames were shown to be compat- ible with the conventional Leksell Stereotactic System© . Most of the head frames were employed in studies with pig models [9, 12], with a design that could not easily be scaled to the ovine model, and was not suitable for clinical use, as reported by Oheim et al. [10]. The present work focuses on the design of a new headframe system (HFS) for the ovine model, suitable for MRI and CT studies, as previously shown for a different animal model by White et al. [9]. The new HFS was developed following clinical requirements

for neurosurgical applications. The work presents the validation of the HFS under a real clinical setting, firstly with an assessment *ex-vivo* and subsequently, during *in-vivo* trials.

2. Materials and methods

2.1 Head Frame System: requirements

The following main design requirements were deemed necessary for the Head Frame System to perform safely and correctly under a real clinical setting:

a)to be compatible and safe for use within a Magnetic Resonance Imaging (MRI) system

b)to be suitable for use within a Computerised Tomography (CT) scanner

c)with a footprint small enough to fit within the bore of a conventional MRI unit

d)with a structure capable of being fixed firmly on a stretcher for easy transportation

e)with a head fixation system capable of withstanding forces and torques caused by the motion of the body of the animal during sedation, neurosurgical procedures and transportation.

f)with a design capable of following conventional clinical procedures during general anaesthesia such as blood sampling, mucosa checking and nasogastric tube introduction

2.2 Head Frame System: design

The HFS represented in Figure 1 and 2 was designed to clamp an ovine head to a Cosman-Roberts-Wells (CRW) stereotactic frame. The ovine head frame weights 5,25 Kg, with a measured footprint of 360 x 350 mm, and can accommodate an ovine head within a workspace of 180 x 280 mm. As shown in the highlight (6) of Figure 2, clamping is achieved through the tightening of two opposing head pins onto the zygomatic arches of the ovine skull. Additional rotational support is provided by a mouth clamp (7) (in Figure 2), which bonds the upper pallet and nose arch. The system has been designed with adjustable headpins and a mouth clamp to accommodate a range of different head sizes without impacting on the rigidity of the fixturing. Interchangeable support pillars allow an adjustable height between the u-frame and the support base. These features enable the ovine head to be placed in the isocenter of the MRI scanning volume, while still ensuring patient airways remain clear.

Frame-based stereotactic procedures are facilitated through CRW arc systems that can be clamped into the novel frame using the same kinematic interface present on CRWs universal compact head rings. The relative position between the kinematics and head pins has been designed to align the brain of the ovine head in the centre of the working volume of a CRW frame. A removable bespoke localiser arch (5) featuring seven fiducial spheres is used to co-register the coordinate system of the MRI or CT scanner with the coordinate system of the CRW stereotactic frame. The fiducial spheres are aligned with the ovine head to ensure proper distribution over the ovine brain.

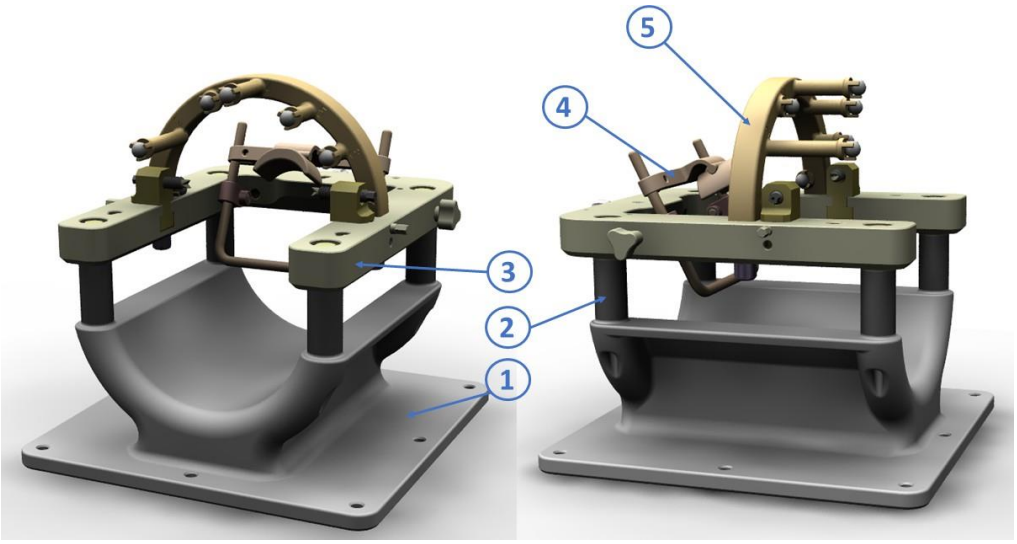

Figure 1: Rendering of the new Head frame System with arc fiducials for MR/CT registrations

2.3 Head Frame System: ex-vivo validation

A set of *ex-vivo* trials, and subsequently *in-vivo* trials following the 3R rules of [13], were performed to assess the HFS under a real clinical setting. Four additional spherical radiopaque markers 8 *mm* in diameter (BrainLab AG., Germany), fixed by titanium screws onto the skull, were used to assess any possible motion of the ovine head during all of the different phases (sedation, transportation, surgery). These four additional markers were screwed randomly in four anatomical areas (one marker per area): on the frontal bone, on the occipital bone, on the anterior orbits bone and on the posterior dorsal orbits bone, as shown in Figure 3.

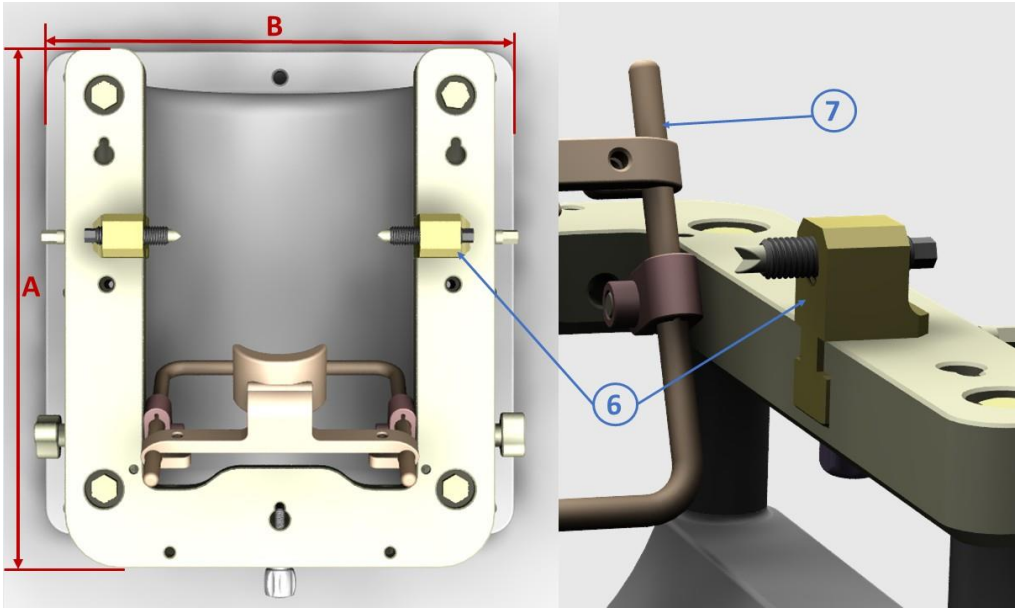

Figure 2: Render top view of the new Head Frame System with highlight of ovine head pins. Headframe footprint of A: 360mm and B: 350mm

Part n.	Description	Materials
(1)	Support base	Nylon
(2)	Support pillar	Acetal
(3)	U-frame	PU
(4)	Mouth clamp	Acetal, PEEK and Nylon
(5)	Bespoke localiser	Nylon with CT/MR fiducials
(6)	Ovine head pins	PU, PEEK and acetal
(7)	as in for (4)	PEEK

Table 1: Parts of the Head Frame with materials used for the manufacturing

For both sets of trials, pre-and post-operative CT imaging sequences were acquired with a clinical system (GE Healthcare CT system, 16 slices helical scan). The imaging sequences were acquired with standard display field of view (DFOV), matrix of 512x512, slice thickness of 0, 625 mm, 120 kilovolt (KV), 22 milliampere (mA), pitch 0, 562 : 1 and $1/s$ tube rotation.

The images were collected using a soft tissue algorithm provided within the software of the scanner.

Figure 3: *ex-vivo* surgical scenario after burr hole drilling. In the picture are noted three of the four fiducial spheres

2.3.1 Ex-vivo trials

Eight female adults, 70kg, *Ovis Aries* sheep *Bergamasca* heads were used for the assessment of the HFS in the *ex-vivo* test. Each ovine head was comprehensive of the neck up to the C3 vertebra.

Head Fixation. As per HFS design features, the sheep head was fixed using two pins clamped against the zygoma bone, without any skin incisions. The mouth bar was placed under the hard

palate and the nose clamp was pressed against the nasal bone. To replicate the sheep's body, a foam box was placed underneath he neck and secured to the HFS via velcro straps.

The head frame system was connected to a medical spinal stretcher (MRI and CT compatible) via plastic zip ties.

Figure 4: *in-vivo* clinical setting of live ovine model with the head frame system during a CT acquisition

Surgical planning and surgical procedure.

Planning software and registration. A conventional neurosurgical procedure which sees the insertion of a straight, rigid needle to reach a predefined target (e.g. a deep lesion) was used as a mock of the real clinical scenario. The target location was identified by the surgeon from an atlas of the ovine white matter bundle [14], establishing the point in the corticospinal tract. The surgical procedure started with a pre-operative CT scan, after the ovine head was fixed onto the Head Frame as described in the previous section. The needle trajectories were planned using a modified

version of a commercial neu- rosurgical software application, the *neuroinspire*^{TM} (Renishaw inc.), designed to register the new Head Frame System with the CRW frame.

Figure 5: Screenshot of the neuroinspire ^{TM}, Renishaw inc- registration arc-fiducials of the HFS with the CRW frame

The software uses 7 fiducials spread along a removable circular arc used to register the HFS with the CRW frame. As shown in Figure 5, the front-end interface provides the CT image of the head frame with a widget showing the displacement of the fiducials within the arc. The user registers each fiducial by selecting each one by one on the top- left widget. Once a fiducial is selected, a circular marker appears on the medical image in correspondence with the position estimate of the selected fiducial on the medical image. In a subsequent step, the user refines the position of the circular marker on the medical image, by moving it using orthogonal zoomed views, as shown on the right widget of Figure 5. Once registration of all seven markers is complete, further registration of different image modalities can be performed automatically by the software. In the example shown in Figure 6, a standard stereotactic ovine MRI reference template [15] was registered to the CT scan, and a Diffusion Tensor Imaging MR tractography reconstruction of the ovine corticospinal tracts was integrated in the planning [14], as part of the multi-modal planning tools exploited in the EDEN2020 project (www.eden2020.eu). As targets, one point for each corticospinal tract (two targets per trial) was selected. In a final step, the user planned suitable trajectories for the tool by

selecting the entry point location on the skull and the target location according to a given clinical case. An example is shown in Figure 6.

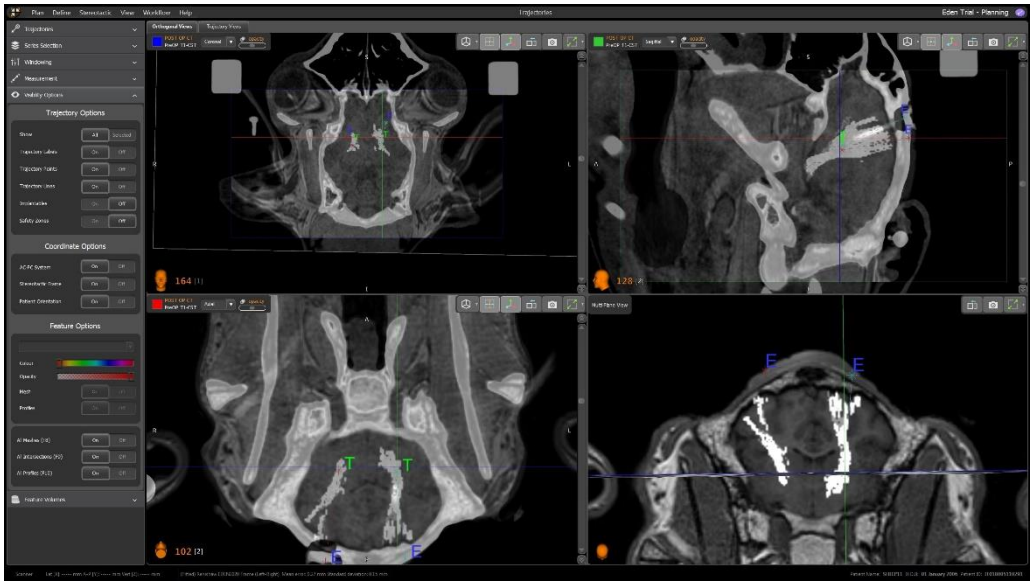

Figure 6: Screenshot of the Neuroinspire TM, Renishaw inc- during the planning of rigid catheter insertion

The area of surgical access was identified approximately 15mm cranially to the coronal suture line and roughly 10mm laterally to the metopic suture line. Ideally, the entry point area had a flat surface above the corticospinal tracts in a zone which was free from significant vessels. Once the area was identified and selected on the software, a set of coordinates on the CRW stereotactic system were provided. The CRW was then assembled on the top plate of the HFS, and a verification shaft tool was used to match the entry point shown in the software. Once the entry point was verified, it was marked on the skull using a pencil to facilitate the drilling phase. To match the real clinical setting, drilling was performed using a conventional neurosurgical perforator 14mm in diameter (CODMAN® Disposable Perforator 14mm- Drill: ANSPACH® EMAX® 2 Plus System by DePuy Synthes). Following the neurosurgical procedure, the head frame system was moved to the CT scanner for postoperative image acquisition. The data acquired were analyzed to measure any head displacement after initial placement and first CT scanning.

2.4. In-vivo trials

After a clinical evaluation of the Head Frame system using *ex-vivo* samples, the HFS was validated *in-vivo*. All animals were treated under the European Communities Council Directive (2010/63/EU), adhering to the laws and regulations on animal welfare enclosed in D.L.G.S. 26/2014 and approved by the Italian Health Department with authorization n° 635/2017.

Animal anesthesia. A total of four sheep *ovis aries* (average 70 kg ,all female, one year old) were used in this study. The animals were under general anaesthesia for all of the procedures described in the following sections. Animals were inducted via intravenous administration of *Diazepam* 0, 25 mg/Kg + *Ketamine* 5 mg/Kg, intubated and then maintained under general anesthesia with *isoflurane* 2% and *oxygen* 2L/m. Two peripheral venous accesses in right and left auricular veins were set for each sheep and urinary catheterization performed.

In-vivo procedure. The *in-vivo* trials procedure was carried out as follow:

Step 1:A general anaesthesia is administered to the animal, as described above

Step 2:The sheep is located on a spinal stretcher (acrylonitrile butadiene styrene, ABS stretcher, Millenia, Ferno) and it is secured in a prone position on a vacuum mattress with extended legs, via two straps.

Step 3:The HFS is placed onto the stretcher and secured using a bespoke fixture system Step 4:The animal head is fixed into the HFS and additional fiducial markers mounted

in the same anatomical areas as in the *ex-vivo* trials.

Step 5:Acquisition of the first CT imaging sequence (CT-pre) at facility A Step 6:Acquisition of a pre-operative MRI volume at facility B

Step 7:The sheep undergoes the surgical procedure (auth n ° 635/2017) at facility A Step 8:A second CT imaging sequence is recorded (post-CT) at facility A

3. Results

3.1 Image Analysis for linear motion of the ovine head

The following imaging process was carried out using 3DSlicer [16], while the assess- ment of the linear motion of the ovine head within the Head Frame System during the procedures (*ex-vivo* and *in-vivo* trials), expressed as the Target Registration Error of the four AFM, was carried out using bespoke software in Matlab (version 2018b, Mathworks Inc). The steps were as follows:

CT pre-operative (CT-pre) and post-operative sequences (CT-post) were loaded into the 3DSlicer software

An intensity filter was applied to the series between W 3000 HU and WL 600 HU, range where arch fiducials of the HFS and the Additional Fiducials Marker (AFM) have maximum intensity

Two meshes, one for pre-operative images (PreOP-Mesh) and one for post-operative images (PostOP-Mesh), were generated PreOP-Mesh and PostOP-Mesh were registered using the Iterative Closest Point algorithm (ICP- algorithm Tolerances: 0.01mm translation, 0.05deg rotation) ap- plied to the centroids of the fiducials of the Bespoke localiser (see n.5 on Table 1)

The output of the registration process defines a transformation matrix *T*

The Centroids of AFMs in the PreOP and PostOP Meshes were extracted using a bespoke algorithm, and identified respectively as $C_{AFM\ pre}$ and $C_{AFM\ post}$

The transformation *T* was applied to each $C_{AFM\ pre}$ to generate the corresponding

centroid on the PostOP reference frame. These fiducials were defined as $\hat{C}_{AFM\ pre}$. 8.The Target Registration Error was calculated as in [17] by using $C_{AF\ Mpre}$ and

$\hat{C}_{AFM\,pre}$, with mean (Π) and standard deviation (σ) of TREs defined as follow:

$$\Pi = \frac{1}{4}\sum_{i=1}^{4} TRE_i \qquad (1)$$

$$\sigma = \sqrt{\frac{1}{4}\sum_{i=1}^{4}(TRE_i - M)^2}$$

The results for the *ex-vivo* and *in-vivo* tests are reported in the Table 2 and 3 respectively. The average linear motion for the *ex-vivo* trials was 0.81 ± 0.54 mm., while for the *in-vivo* trials was

0.68 ± 0.61 mm. The average RMSE for Arc Fiducial registration Error (FRE) for both tests was: 0.46 ± 0.12, inline with results of [9] using the software described in Section 3.2.1.

Trial n.	Π± $\sigma[mm]$	Arc FRE [rmse]
1	0.93 ± 0.7	0.73
2	1.07 ± 0.86	0.28
3	0.81 ± 0.45	0.55
4	1.04 ± 0.26	0.49
5	0.55 ± 0.15	0.46
6	0.95 ± 0.9	0.38
7	0.71 ± 0.05	0.29
8	0.46 ± 0.09	0.44

Table 2: Results of *ex-vivo* trials

Trial n.	Π± $\sigma[mm]$	Arc FRE [rmse]
1	0.35 ± 0.13	0.53
2	0.75 ± 0.18	0.59
3	0.74 ± 0.56	0.41
4	0.83 ± 0.1	0.44

Table 3: Results of *in-vivo* trials

3.2 MRI compatibility test

MRI compatibility testing of the prototype was evaluated in an MRI scanner (Philips Achieva 1.5T, Philips Healthcare, The Netherlands) as in [18]. The prototype was installed at the centre of the field of view as shown in Figure 7, with a standard MR cylindrical phantom containing a saline solution of nickel sulfate ($N_iSO_4 + 6H_2O/2.62g\ NaCl$) placed inside the Head Frame. A T1-weighted volumetric scan was acquired by using a three-dimensional fast-field-echo (3D-T1 FFE) sequence with the following pa- rameters: repetition time/echo time (TR/TE) $20ms, /, 3.7ms$; flip angle 40°; voxel size 0.667×0.667×1.4 mm; SENSE factor R = 2. We tested two cases: the first case with only the phantom and the second case, with the Phantom and the Head Frame placed inside the bore of the MR scanner. Coronal slices were used in this evaluation. An example slice from the image set is reported in Figure 8: the image shows no geometrical imaging distortion caused by the Head Frame. The data analysis was carried out following the National Electrical Manufacturers Association (NEMA) procedures [19] standard assuming a statistically and spatially uniform distribution of noise.

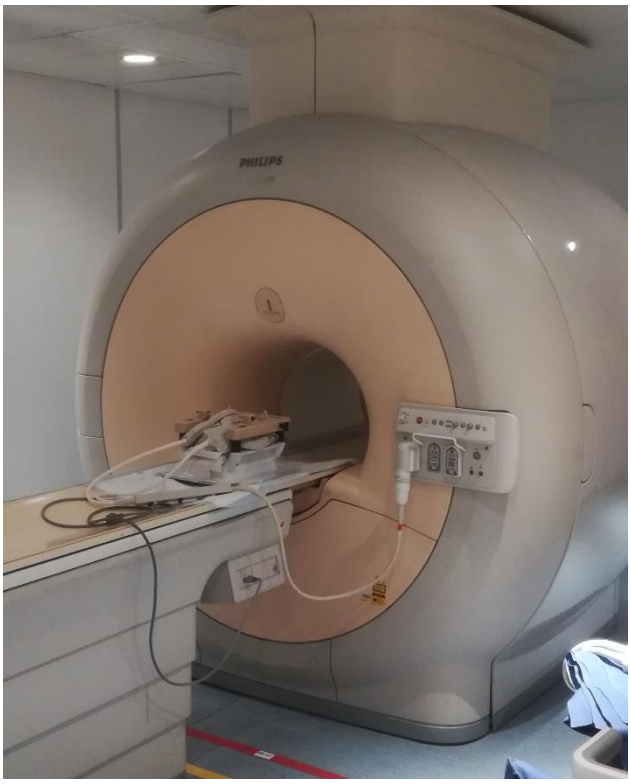

Figure 7: MR test setup with the Head Frame placed inside the bore of the machine

Two regions of interests (ROIs) of 50 × 50 pixels were selected as shown in Figure 8: one region inside the tissue phantom, and a second region outside the tissue phantom and far from the Head Frame. The noise was computed for all images, covering the whole footprint of the Head Frame, individually, and then averaged. The first image set, image set A (with only the phantom inside the MRI) was considered as the baseline, of which SNR is reported in Figure in red. The total variation of the SNR for image set B (with Head Frame - blu line in Figure 9) was 1255.2 (−41.9%- red line). The average SNR value for the baseline was 2160.8, which was calculated as reported in [20, 21, 22].

A sample slice of the full imaging sequences are reported in Figure 10 and Figure 11 respectively the sequence without the Head Frame and with the Head Frame, while a render of the MR Volumes in both cases are reported in Figure 12.

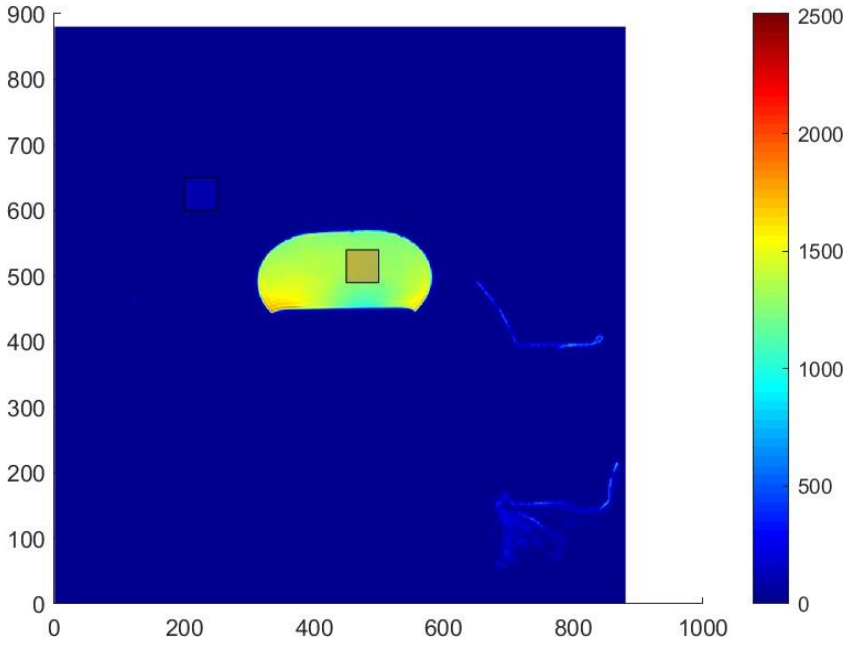

Figure 8: Slice n.20 on MR set with phantom and Head Frame. Bottom-right shadows is water moist over part of the Head Frame structure.

Discussion

Sheep has been employed as the animal model for translational applications in a range of studies including epilepsy [5], neuropsychiatrics [23], traumatology [2], cardio- vascular [24] and neurological diseases [3]. The ovine brain size features gyrencephalic sulci as in the human brain, showing better modelling characteristics when compared to lissencephalic rodent brain [25]. Even if primate brains are anatomically and functionally more similar to human brains, their use is limited due to the strict ethical constraints

[26] [27]. The pig animal model seems to be the most used in neuroscience [28] [29], but aspects of their skull anatomy should be considered. For instance, the anterior pig head has a planar forehead and vertex that end in a high crest where the neck muscles are inserted. Laterally, the vertex is limited by the parietal bone, reducing the accessible brain area to a small square, as shows in [30]. Additionally, minipig breeds and domestic pig have a fast growth index if compared with sheep, with an average daily weight gain for Large White-Landrace reported to be between 734 and 992 g/day in the first six months of life [31], reaching the adult stage (1-2 years in age) at more than 300 Kg [2

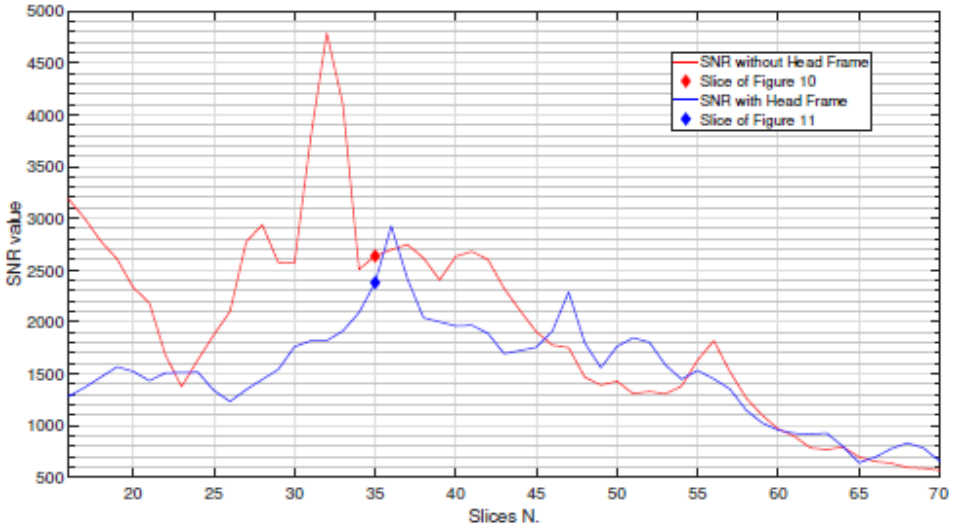

Figure 9: SNR for dataset A (red line - without Head Frame) and for dataset B (blue line - with Head Frame). Market points are SNR of the Figure 8 and Figure 9, respectively with value 2636 and 2378 (-9.78%)

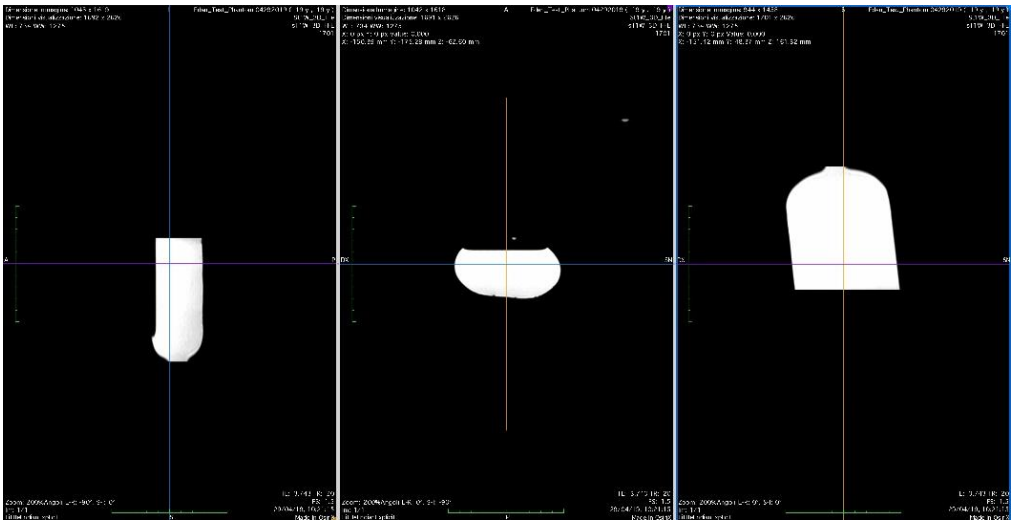

Figure 10: MRI sequence with only the phantom (slice n.35).

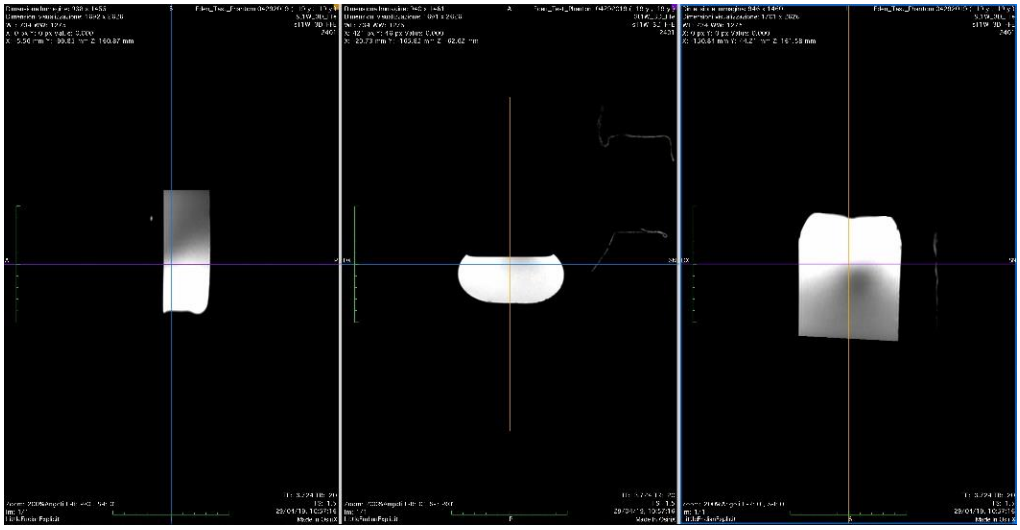

Figure 11: MRI sequence with phantom and Head Frame (slice n.35). The image report a visible attenuation of SNR (as reported in Figure 9) but without geometrical distorsion

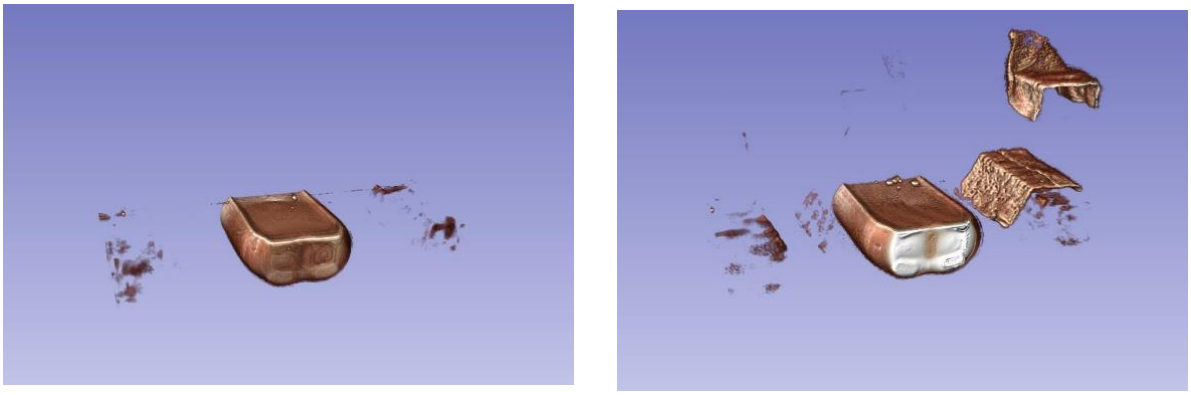

Figure 12: MRI Volume Render: on the left, only the phantom while on the right, the phantom and the Head Frame. In the latter, wet tissue placed over the Head Frame to enhance the visualisation.

Last, minipig and pig models at 3-6 months develop a sizeable frontal sinus that pneumatizes all of the dorsolateral part of the skull [12], thus becoming impracticable for application in neurosurgery experiments [11] and chronic postoperative management. The sheep skull bone anatomy is distinguished by less skull cap convexity than human and primates [32], requiring a bespoke head frame design to be used in near investigation studies.

In literature, previous studies [10, 11, 33] have used an experimental stereotactic frame which is not applicable in a clinical setting because the lack of MRI compatibility involves the use of a specific brain atlas which could lead to inaccuracy during the surgi- cal procedure, this latter bolstered by the variability within the ovine species. Frameless stereotactic systems could be employed to overcome the variability issue during the sur- gical procedure, however, the cost associated to neuronavigation systems are significant [34]. Dhawan et al. [35] demonstrated that these two stereotactic methods have equiva- lent accuracy, thus frame-based systems could be more cost-effective for animal studies, especially in the context of interventional MR studies, which are becoming increasingly popular in related literature. In light of these findings, framed systems facilitate animal management during general anaesthesia by supporting the head in a fastened position during the surgical procedure and transportation (e.g. between the surgical room and the CT or MRI suite). Last, amid frame systems it is possible to avoid using bone fiducials, which in a research situation are employed on the same day of the surgical procedure, with additional stress to the animal.

Conclusion

In this work, we present a novel head frame system for the ovine model, to address several clinical requirements of translational studies, such as CT/MRI compatibility, compatibility with a conventional human stereotactic CRW frame, robustness during the surgical procedure and robustness against the anatomical variability which is inherent in the sheep model. The system described in this study may benefit future research projects using sheep as an animal model.

Competing interests

The authors declare that they have no competing interests.

Acknowledgements

This project has received funding from the European Unions EU Research and Inno- vation programme Horizon 2020 under grant agreement [no 688279]

[1]L. Martini, M. Fini, G. Giavaresi, R. Giardino, Sheep model in orthopedic research: A literature review, Comparative Medicine 51 (4) (2001) 292–299.

[2]J.-X. Dai, Y.-B. Ma, N.-Y. Le, J. Cao, Y. Wang, Large animal models of traumatic brain injury, International Journal of Neuroscience 128 (3) (2018) 243–254.

[3]L. Karageorgos, L. Hein, T. Rozaklis, M. Adams, S. Duplock, M. Snel, K. Hemsley, T. Kuchel, N. Smith, J. J. Hopwood, Glycosphingolipid analysis in a naturally occurring ovine model of acute neuronopathic gaucher disease, Neurobiology of Disease 91 (2016) 143 – 154. doi:https://doi.org/10.1016/j.nbd.2016.03.011.

[4]S. J. Reid, N. E. Mckean, K. Henty, E. Portelius, K. Blennow, S. R. Rudiger, C. S. Bawden, R. R. Handley, P. J. Verma, R. L. Faull, H. J. Waldvogel, H. Zetterberg, R. G. Snell, Alzheimer's disease markers in the aged sheep (ovis aries), Neurobiology of Aging 58 (2017) 112 – 119. doi:https://doi.org/10.1016/j.neurobiolaging.2017.06.020.

[5]P. H. Stypulkowski, S. R. Stanslaski, R. M. Jensen, T. J. Denison, J. E. Giftakis, Brain stimulation for epilepsy local and remote modulation of network excitability, Brain Stimulation 7 (3) (2014) 350 – 358. doi:https://doi.org/10.1016/j.brs.2014.02.002.

[6]P. H. Stypulkowski, J. E. Giftakis, T. M. Billstrom, Development of a Large Animal Model for Investigation of Deep Brain Stimulation for Epilepsy, Stereotactic and Functional Neurosurgery 89 (2011) 111–122. doi:10.1159/000323343.

[7]P. H. Stypulkowski, S. R. Stanslaski, J. E. Giftakis, Modulation of hippocampal activity with fornix deep brain stimulation, Brain Stimulation 10 (6) (2017) 1125 – 1132. doi:https://doi.org/10.1016/j.brs.2017.09.002.

[8]C. R. Bjarkam, G. Cancian, A. N. Glud, K. S. Ettrup, R. L. Jrgensen, J.-C. Srensen, Mri-guided stereotaxic targeting in pigs based on a stereotaxic localizer box fitted with an isocentric frame and use of surgiplan computer-planning software, Journal of Neuroscience Methods 183 (2) (2009) 119 – 126. doi:https://doi.org/10.1016/j.jneumeth.2009.06.019.

[9]E. White, M. Woolley, A. Bienemann, D. Johnson, M. Wyatt, G. Murray, H. Taylor, S. Gill, A robust mri-compatible system to facilitate highly accurate stereotactic administration of therapeutic agents to targets within the brain of a large animal model, Journal of Neuroscience Methods 195 (1) (2011) 78 – 87. doi:https://doi.org/10.1016/j.jneumeth.2010.10.023.

[10]R. Oheim, F. T. Beil, F. Barvencik, M. Egermann, M. Amling, I. C. P. Pogoda, Targeting the lateral but not the third ventricle induces bone loss in ewe: An experimental approach to generate an improved large animal model of osteoporosiss, The Journal of Trauma and Acute Care Surgery 72 (3) (2012) 720–726.

[11]N. Perentos, A. Nicol, A. Martins, J. Stewart, P. Taylor, A. Morton, Techniques for chronic moni- toring of brain activity in freely moving sheep using wireless eeg recording, Journal of Neuroscience Methods 279 (2017) 87 – 100. doi:https://doi.org/10.1016/j.jneumeth.2016.11.010.

[12]C. Bjarkam, G. Cancian, M. Larsen, F. Rosendahl, K. Ettrup, D. Zeidler, A. Blankholm, L. ster- gaard, N. Sunde, J. Srensen, A mri-compatible stereotaxic localizer box enables high-precision stereotaxic procedures in pigs, Journal of Neuroscience Methods 139 (2) (2004) 293 – 298. doi:https://doi.org/10.1016/j.jneumeth.2004.05.004.

[13]P. Flecknell, Replacement, reduction and refinement., ALTEX 19 (2) (2002) 73–8.

[14]V. Pieri, M. Trovatelli, M. Cadioli, D. D. Zani, S. Brizzola, G. Ravasio, F. Acocella, M. Di Gian- camillo, L. Malfassi, M. Dolera, M. Riva, L. Bello, A. Falini, C. A, In vivo diffusion tensor magnetic resonance tractography of the sheep brain: an atlas of the ovine white matter fiber bundles, Frontiers Veterinary Science - *Under Review*.

[15]B. Nitzsche, S. Frey, L. D. Collins, J. Seeger, D. Lobsien, A. Dreyer, H. Kirsten, M. H. Stoffel, V. S. Fonov, J. Boltze, A stereotaxic, population-averaged t1w ovine brain atlas including cerebral morphology and tissue volumes, Frontiers in Neuroanatomy 9 (2015) 69. doi:10.3389/fnana.2015. 00069. URL https://www.frontiersin.org/article/10.3389/fnana.2015.00069

[16]A. Fedorov, R. Beichel, J. Kalpathy-Cramer, J. Finet, J.-C. Fillion-Robin, S. Pujol, C. Bauer, D. Jennings, F. Fennessy, M. Sonka, J. Buatti, S. Aylward, J. V. Miller, S. Pieper, R. Kikinis, 3d slicer as an image computing platform for the quantitative imaging network, Magnetic Resonance Imaging 30 (9) (2012) 1323 – 1341, quantitative Imaging in Cancer. doi:https://doi.org/10. 1016/j.mri.2012.05.001.

[17]J. M. Fitzpatrick, J. B. West, The distribution of target registration error in rigid-body point- based registration, IEEE Transactions on Medical Imaging 20 (9) (2001) 917–927. doi:10.1109/ 42.952729

[18]R. Secoli, M. Robinson, M. Brugnoli, F. Rodriguez y Baena, A low-cost, high-field-strength magnetic resonance imaging compatible actuator, Proceedings of the Institution of Mechanical Engineers, Part H: Journal of Engineering in Medicine 229 (3) (2015) 215–224. doi:10.1177/0954411915574306.

[19]Rosslyn, Determination of signal-to-noise ratio (snr) in diagnostic magnetic resonance imaging, National Electrical Manufacturers Association (NEMA) 229 (3) (2008) 215–224.

[20]L. Kaufman, D. M. Kramer, L. E. Crooks, D. A. Ortendahl, Measuring signal-to-noise ratios in mr imaging., Radiology 173 (1) (1989) 265–267. doi:10.1148/radiology.173.1.2781018.

[21]R. M. Henkelman, Measurement of signal intensities in the presence of noise in mr images, Medical Physics 12 (2) (1985) 232–233. doi:10.1118/1.595711.

[22]O. Dietrich, J. G. Raya, S. B. Reeder, M. F. Reiser, S. O. Schoenberg, Measurement of signal- to-noise ratios in mr images: Influence of multichannel coils, parallel imaging, and reconstruction filters, Journal of Magnetic Resonance Imaging 26 (2) (2007) 375–385. doi:10.1002/jmri.20969.

[23]E. Nestler J., S. Hyman E., Animal models of neuropsychiatric disorders, Nature Neuroscience 13 (10) (2010) 1161–1169.

[24]J. L. David, C. J. Christopher, M. C. Ian, M. N. Clive, F. D. Melanie, F. M. Christopher, B. I. Sinclair, I. Hamid, Continual recordings of cardiac sympathetic nerve activity in conscious sheep, American Journal of Physiology. Heart and circolatory physiology 282 (1) (2002) H93–9.

[25]J. W. Finnie, Animal models of traumatic brain injury: a review, Australian Veterinary Journal 79 (9) (2001) 628–633. doi:10.1111/j.1751-0813.2001.tb10785.x

[26]J. P. Capitanio, M. E. Emborg, Contributions of non-human primates to neuroscience research, The Lancet 371 (9618) (2008) 1126 – 1135. doi:https://doi.org/10.1016/S0140-6736(08)60489-4.

[27]D. A. Grow, J. R. McCarrey, C. S. Navara, Advantages of nonhuman primates as preclinical models for evaluating stem cell-based therapies for parkinson's disease, Stem Cell Research 17 (2) (2016) 352 – 366. doi:https://doi.org/10.1016/j.scr.2016.08.013.

[28]N. M. Lind, A. Moustgaard, J. Jelsing, G. Vajta, P. Cumming, A. K. Hansen, The use of pigs in neuroscience: Modeling brain disorders, Neuroscience Biobehavioral Reviews 31 (5) (2007) 728 – 751. doi:https://doi.org/10.1016/j.neubiorev.2007.02.003.

[29]P. Sauleau, E. Lapouble, D. Val-Laillet, C.-H. Malbert, The pig model in brain imaging and neu- rosurgery, animal 3 (8) (2009) 11381151. doi:10.1017/S1751731109004649.

[30]J. Regelsberger, Surgery of the Brain and Spinal Cord in a Porcine Model, Springer New York, New York, NY, 2016, pp. 165–173.

[31]M. R. Taverner, R. G. Campbell, R. H. King, R. J. Johnson, Effects of gender and genotype on the response of growing pigs to exogenous administration of porcine growth hormone1, Journal of Animal

Science 68 (9) (1990) 2674–2681. doi:10.2527/1990.6892674x. URL https://dx.doi.org/10.2527/1990.6892674x

[32]B. Nitzsche, H. Barthel, D. Lobsien, J. Boltze, V. Zeisig, A. Y. Dreyer, Focal Cerebral Ischemia by Permanent Middle Cerebral Artery Occlusion in Sheep: Surgical Technique, Clinical Imaging, and Histopathological Results, Springer New York, New York, NY, 2016, pp. 195–225.

[33]I. van der Bom, R. Moser, G. Gao, E. Mondo, D. O'Connell, M. Gounis, S. McGowan, J. Chaurette, N. Bishop, M. Sena-Esteves, C. Mueller, N. Aronin, Finding the striatum in sheep: Use of a multi- modal guided approach for convection enhanced delivery, Journal of Huntington's disease 2 (1) (2013) 41–45. doi:https://doi.org/10.3233/JHD-130053.

[34]W. Kucharczyk, M. Bernstein, Do the benefits of image guidance in neurosurgery justify the costs? from stereotaxy to intraoperative mr., American Journal of Neuroradiology 18 (10) (1997) 1855–1859. arXiv:http://www.ajnr.org/content/18/10/1855.full.pdf. URL http://www.ajnr.org/content/18/10/1855

[35]S. Dhawan, Y. He, J. Bartek, A. A. Alattar, C. C. Chen, Comparison of frame-based versus frameless intracranial stereotactic biopsy: Systematic review and meta-analysis, World Neurosurgerydoi: https://doi.org/10.1016/j.wneu.2019.04.01

In vivo diffusion tensor magnetic resonance tractography of the sheep brain: an atlas of the ovine white matter fiber bundles

(Published in Frontiers in Veterinary Science DOI: doi.org/10.3389/fvets.2019.00345)

In vivo diffusion tensor magnetic resonance tractography of the sheep brain: an atlas of the ovine white matter fiber bundles

Valentina Pieri1, Marco Trovatelli2, Marcello Cadioli3, Davide Danilo Zani4, Stefano Brizzola4, Giuliano Ravasio4, Fabio Acocella2, Mauro Di Giancamillo4, Luca Malfassi5, Mario Dolera5, Marco Riva6,7, Lorenzo Bello7,8, Andrea Falini1, Antonella Castellano1

[1]*Neuroradiology Unit and CERMAC, Vita-Salute San Raffaele University and IRCCS San Raffaele Scientific Institute, Milano, Italy*

[2]*Department of Health, Animal Science and Food Safety, Faculty of Veterinary Medicine, University of Milan, Milan, Italy*

[3]*Philips Healthcare, Italy*

[4]*Department of Veterinary Medicine, Università degli Studi di Milano, Milan, Italy*

[5]*Fondazione La Cittadina Studi e Ricerche Veterinarie, Romanengo (CR), Italy*

[6]*Department of Medical Biotechnology and Translational Medicine, Università degli Studi di Milano, Milan, Italy*

[7]*Neurosurgical Oncology Unit, Humanitas Clinical and Research Center – IRCCS, Rozzano (MI), Italy*

[8]*Department of Oncology and Hemato-Oncology, Università degli Studi di Milano, Milan, Italy*

* Correspondence:

Corresponding Author: Antonella Castellano, MD, PhD

Neuroradiology Unit and CERMAC,

Vita-Salute San Raffaele University and IRCCS San Raffaele Scientific Institute

Via Olgettina, 60

20132 Milano, Italy

e-mail: castellano.antonella@hsr.it

Keywords: Diffusion Tensor Imaging, DTI Tractography, sheep, brain, atlas

Abstract

Diffusion Tensor Magnetic Resonance Imaging (DTI) allows to decode the mobility of water molecules in cerebral tissue, which is highly directional along myelinated fibres. By integrating the direction of highest water diffusion through the tissue, DTI Tractography enables a non-invasive dissection of brain fibre bundles. As such, this technique is a unique probe for *in vivo* characterization of white matter architecture. Unravelling the principal brain texture features of preclinical models that are advantageously exploited in experimental neuroscience is crucial to correctly evaluate investigational findings and to correlate them with real clinical scenarios. Although structurally similar to the human brain, the gyrencephalic ovine model has not yet been characterized by a systematic DTI study. Here we present the first *in vivo* sheep (*ovis aries*) tractography atlas, where the course of the main white matter fibre bundles of the ovine brain has been reconstructed. In the context of the EU's Horizon EDEN2020 project, *in vivo* brain MRI protocol for ovine animal models was optimized on a 1.5T scanner. High resolution conventional MRI scans and Diffusion Tensor Imaging (DTI) sequences (b-value=1000 s/mm^2, 15 directions) were acquired on ten anesthetized sheep *ovis aries*, in order to define the diffusion features of normal adult ovine brain tissue. Topography of the ovine cortex was studied and DTI maps were derived, to perform DTI tractography reconstruction of the corticospinal tract (CST), corpus callosum (CC), fornix (FX), visual pathway (VP) and occipitofrontal fascicle (OF), bilaterally for all the animals. Binary masks of the tracts were then coregistered and reported in the space of a standard stereotaxic ovine reference system, to demonstrate the consistency of the fibre bundles and the minimal inter-subject variability in a unique tractography atlas.

Our results determine the feasibility of a protocol to perform *in vivo* DTI tractography of the sheep, providing a reliable reconstruction and 3D rendering of major ovine fibre tracts underlying different neurological functions. Estimation of fibre directions and interactions would lead to a more comprehensive understanding of the sheep's brain anatomy, potentially exploitable in preclinical experiments, thus representing a precious tool for veterinaries and researchers.

1. Introduction

The organization of white matter microstructure and brain connections can be depicted *in vivo* by Diffusion Tensor Imaging (DTI), an advanced Magnetic Resonance (MR) technique which provides a unique probe to noninvasively quantify the directional, *anisotropic* mobility of water molecules within tissues (Basser and Pierpaoli, 1996). In cerebral white matter, water mobility is hindered along the main direction of the fibres by the multiple layers of myelin around the axons; therefore, the principal axis of the diffusion tensor aligns with the predominant fibre orientation within the tissue (Winston, 2012;Le Bihan, 2014). One of the most important applications of DTI technique is MR tractography, or fibre-tracking, a method that can be used for the virtual dissection of the relevant myelin-sheathed fibre bundles within the brain. MR tractography is the process of integrating fibre orientations within tissue into a trajectory connecting remote brain areas, starting from anatomical seed regions and following the directions of highest water diffusion until stopping criteria are met (Mori and van Zijl, 2002).

DTI and tractography have broadened the understanding of the white matter pathways hidden within the brain tissue, complementing anatomical information from conventional MRI. Furthermore, the increasing exploitation of these technique in clinical studies has revealed their great potential for understanding healthy and pathological brain anatomy in humans, paving the way toward their application also in preclinical animal models. Therefore, translational researchers are increasingly embracing these techniques for a comprehensive description of white matter fiber distribution in healthy animals as well as to study developmental pathologies, exposure to teratogens, or the effects of malnutrition and hypoxia in the prenatal environment (Oguz et al., 2012).

Remarkably, the evaluation of brain structural and ultrastructural features with DTI in preclinical models offers the possibility of validating the imaging-derived information by comparing them to histological sections with precise spatial correlation, once the animals have been sacrificed. Different animal models have been investigated with DTI, such as ferrets (Hutchinson et al., 2016;Hutchinson et al., 2017), rats (Li et al., 2011;Van Camp et al., 2012), tree shrew (Dai et al., 2017) and mice (Harsan et al., 2010;Jiang and Johnson, 2010). Nonetheless, it is worth of note that most of DTI studies on larger animals have been performed on formalin-fixed brain sections and not *in vivo*, thus potentially invalidating the diffusion properties of brain tissue. This has been the case

of studies on non-human primates (Makris et al., 2010;Rane et al., 2010;Uematsu et al., 2017), dolphins (Berns et al., 2015), dogs (Jacqmot et al., 2013;Anaya Garcia et al., 2015) and cats (Takahashi et al., 2011).

On the other hand, the application of DTI and tractography has been extremely deficient in other species considered as relevant models in translational research, including sheep. Sheep offer a great degree of research translatability into basic brain functions as they have a long lifespan, have rudimentary and well-established housing demands and are safer than primates to be managed in experimental settings, especially because they do not have hands to interfere with equipment (Perentos et al., 2017). Most importantly, the gyrencephalic ovine brain is anatomically and functionally more similar to human brain if compared to the lissencephalic brain of rodents and rabbits, due to its relatively large size and the presence of sulci (Finnie, 2001). Further similar features to humans are evident in electroencephalographic records, neuroradiological features, and neurovascular structures (Morosanu et al., 2019), thus making the ovine model of particular relevance in the field of experimental neuroscience. For example, it has been studied in the context of epilepsy (Stypulkowski et al., 2014), neuropsychiatry (Nestler and Hyman, 2010), traumatic brain injury (Dai et al., 2018) and neurodegenerative diseases (Karageorgos et al., 2016;Reid et al., 2017). The similarities between caudate, putamen and substantia nigra in the sheep and human brains, in fact, provide a valuable and valid tool for modelling basal ganglia diseases (Murray et al., 2019). Intriguingly, studies recently demonstrated neurofibrillary accumulation in normal aged sheep, extremely similar to the tau deposits associated to Alzheimer's disease (AD) in humans, so that researchers are now testing the fitness of the ovine for future genetic manipulation to generate AD animal model (Reid et al., 2017).

Furthermore, due to these similarities with human brain, the ovine model can be particularly valuable in the context of neurosurgical research to test new devices and peri-operative technologies. In this scenario, the possibility to explore *in vivo* the imaging features of the ovine brain becomes relevant for pre-surgical planning and intraoperative neuronavigation. Despite the growing interest in using sheep as a model of large mammals with complex central nervous system, comprehensive ovine MRI studies are rather limited, presumably because they are hardly feasible and require a well-organized and specialized multidisciplinary team (Capitanio and Emborg, 2008). The main efforts have been focused on defining MRI templates and atlases of the ovine brain based on conventional T1- and T2-weighted MR images, and to build up a standard stereotaxic ovine

reference system (Ella and Keller, 2015;Nitzsche et al., 2015;Ella et al., 2017). On the other hand, advanced MR imaging studies including DTI on sheep are even rarer and on a small number of animals. To our knowledge, the only work on the applicability of DTI on living healthy sheep has been conducted by Lee et al., on a limited sample of 6 sheep (Lee et al., 2015). They exploited functional MRI (fMRI) to visualize the sensorimotor and visual cortex activated by external sensory stimuli, then performed DTI tractography to reconstruct corticospinal tract and optic radiations starting from the activated cortical areas (Lee et al., 2015). Despite representing a step forward for advanced MRI of the ovine models, a comprehensive

analysis of the ovine white matter organization using DTI is still lacking. Furthermore, an ovine population-averaged MR tractography atlas within a stereotaxic space has not been reported yet. Hence, the aim of the present work is to demonstrate the feasibility and reproducibility of DTI tractography in living sheep by reconstructing the main white matter fibre bundles of the ovine brain.

Moreover, the registration of every tract of all the animals were performed and the integration of these population-averaged tractography data within a standard stereotaxic ovine reference system (Nitzsche et al., 2015) was implemented to generate the first healthy sheep brain tractography atlas *in vivo*.

2 Materials and Methods

2.1 Study population and ethics

A total of ten adult female adult sheep *ovis aries* (Bergamasca, weight = 72,2 ± 5,4 kg) were used in this study, carried on in the context of the European Union's EU Horizon EDEN2020 project (https://www.eden2020.eu/) that has the final aim of testing an integrated technology platform for minimally invasive brain surgery on ovine models. Sheep have been selected due to their anatomy, physiology, and neurological development. The choice of female gender was due to the size, weight and to the social behaviour characterized by a low agonist component, favoring housing and handling.

For all subjects, a detailed clinical and physiological score was daily reported in an *ad-hoc* ethogram (Supplementary Table 1). The sheep were fasted but with free access to water 24 hours prior to each imaging session. All animals were treated in accordance with the European Communities Council directive (2010/63/EU), to the laws and regulations on animal welfare enclosed in D.L.G.S. 26/2014.

Ethical approval for this study was obtained by the Italian Health Department with authorization n 136 635/2017.

2.2 Anesthesia and *in vivo* MR Imaging

Animals were anesthetized via the intravenous administration of Diazepam 0,25 mg/Kg + Ketamine 5 mg/Kg, intubated and then maintained under general anesthesia with isoflurane 2% and oxygen 2L.

They were transported to the imaging facility and placed in prone position, with the head located in a MRI-compatible headframe (Renishaw®) specifically made for the EDEN2020 project. MR imaging was performed on a 1.5T clinical scanner (Achieva, Philips Healthcare) in a veterinary imaging facility [Fondazione La Cittadina Studi e Ricerche Veterinarie, Romanengo (CR), Italy]. Small and medium flex coils fixed over both hemispheres were used. Diffusion Tensor Imaging (DTI) data were obtained from all the animals by using a single-shot echo planar sequence with parallel imaging (SENSE factor R=2). Diffusion gradients were applied along 15 non-collinear directions, using a b-value of 1000 s/mm2. The detailed imaging parameters for DTI were: TR/TE 6700 ms/84 ms; acquisition isotropic voxel size 2 × 2 × 2 mm; 45 slices. Two signal averages (NSA=2) were obtained, for a total scan time of 5 minutes 34 seconds. A T1-weighted volumetric scan was also acquired from each animal by using a three-dimensional fast-field-echo (3D-T1 FFE) sequence with the following parameters: TR/TE 25 ms/5 ms; flip angle 40°; voxel size 0.667 × 0.667 × 1.4 mm; SENSE factor R=2; 150 slices; acquisition time 8 min 40 s. All the MRI sequences were oriented perpendicular to the longitudinal axis of the scanner. Other structural/anatomical MR imaging sequences were acquired for purpose of neuronavigation in the context of the EDEN2020 project, including T2-weighted turbo spin-echo (TSE), three-dimensional high-resolution time-of-flight (TOF) MR angiography, Susceptibility- Weighted Imaging (SWI) and phase-contrast images (PCA) for MR venography. The detailed parameters of these sequences are listed in Supplementary Table 2, but they were not used for the herein presented study.

2.3 DTI data analysis and tractography reconstructions

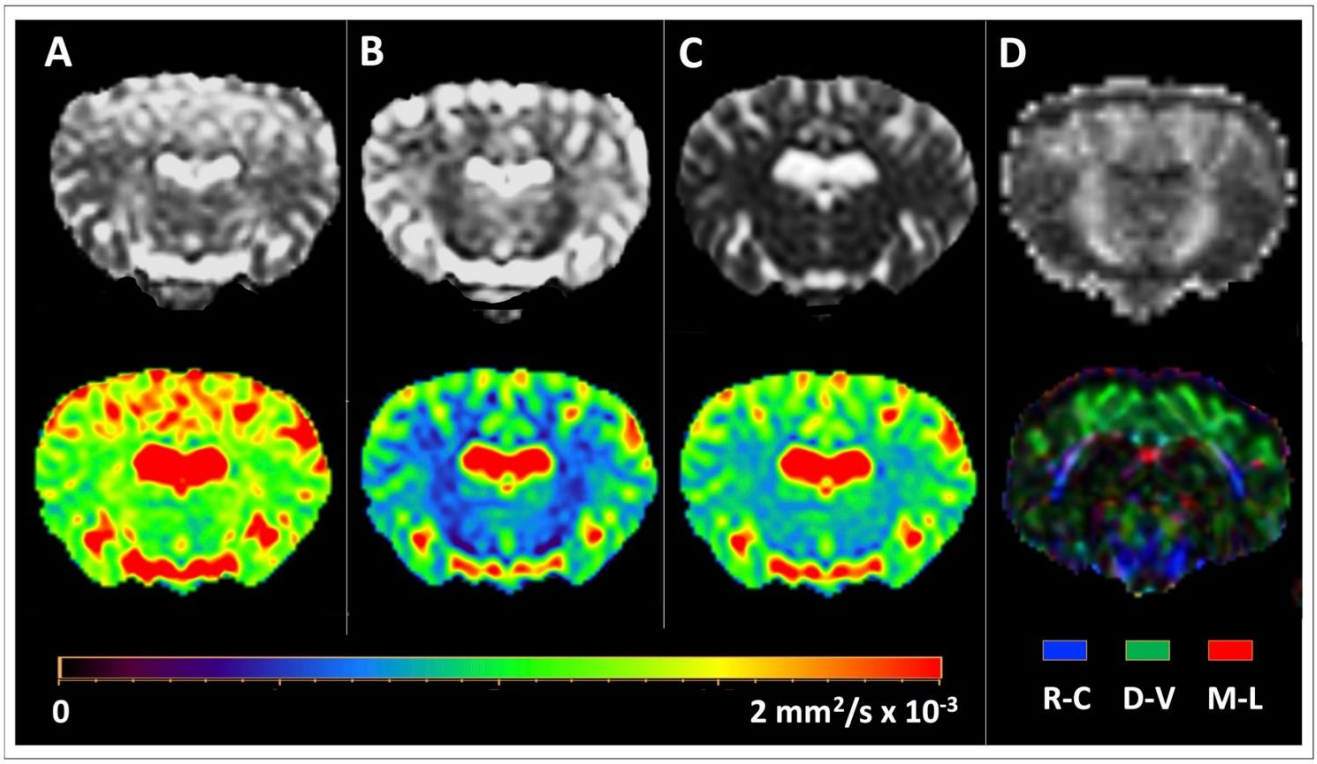

Figure 1 – DTI-derived maps for a representative ovine brain
Computed maps of diffusion ($mm^2/s \times 10^{-3}$) are shown in gray scale (upper row) and color LUT (Look Up Tables) display (lower row). (A) The Axial Diffusivity (AD) map shows the diffusion along the principal axis of the diffusion tensor. (B) The Radial Diffusivity (RD) map shows the diffusion perpendicular to the main axis of the tensor. Notably, low values in correspondence of the ovine internal capsule indicate the dominance of the principal direction in that region. (C) The Mean Diffusivity (MD) map shows the the orientation-averaged apparent diffusivity, averaged on the diffusion orientations. (D) The Fractional Anisotropy (FA) map shows the scalar value of the fraction of anisotropic diffusion over the total diffusion, and range between 0 and 1 (upper row). From the combination of the FA and principal eigenvector ε_1, color maps are derived with conventional color-coding (Pajevic and Pierpaoli, 1999) (lower row), displaying fibers with rostral-caudal (R-C) direction in blue, fibers with dorsal-ventral (D-V) direction in green, and fibers with medial-lateral (M-L) in red.

DTI data were analyzed with the Philips IntelliSpace Portal software platform, version 8.0 (Philips Healthcare, Best, The Netherlands). DTI datasets were firstly corrected for motion artifacts by applying affine alignment of each diffusion-weighted image to the b=0 image, then the DTI sequence was aligned to the volumetric T1 sequence by means of the Local Correlation tool of the Philips IntelliSpace Portal software platform v8.0. Diffusion tensor element were calculated and diagonalized at each voxel using the MR Diffusion tool of the Intellispace Portal software platform, obtaining the three eigenvectors (ε_1, ε_2, ε_3), and diffusivities (λ_1, λ_2, λ_3) along these vectors. From these, Mean Diffusivity (MD), Axial Diffusivity (AD), Radial Diffusivity (RD) and

Fractional Anisotropy (FA) maps were computed for each sheep (Figure 1). MD is a measure of the orientation-averaged apparent diffusivity within a voxel, while AD and RD respectively measure water diffusion parallel and perpendicular to the main axis of the tensor. The Fractional Anisotropy (FA) map describes the degree of diffusion anisotropy within a voxel, being a scalar value between 0 and 1. From the combination of the FA and principal eigenvector ε_1, color maps were generated with conventional color-coding (Pajevic and Pierpaoli, 1999). Color-coded FA maps emphasizes the directionality of diffusion by displaying fibers with rostral-caudal (R-C) direction in blue, fibers with dorsal-ventral (D-V) direction in green, and fibers with medial-lateral (M-L) in red (Figure 1D).

Whole brain deterministic tractography was performed using the MR Fiber Trak tool of the IntelliSpace Portal software through the fiber assignment by continuous tracking algorithm, with an FA threshold of 0.15 and an angle threshold of 27°. Inclusive and exclusive seed regions-of-interest (ROIs) were manually delineated on the color-coded FA maps for a virtual dissection of the main ovine white matter tracts. High resolution T1-weighted volumetric images were superimposed to the color-coded FA maps to facilitate the identification of the main anatomical structures in the sheep. For each tract, seed ROIs were placed in different anatomical positions according to the different fiber tracts *in consensus* by an expert neuroradiologist (A.C. with 15 years of experience in DTI tractography reconstructions), a PhD student in neuroimaging (V.P., with two years of experience in DTI tractography analysis) and a PhD student in veterinary sciences with a specific training on anatomical dissection of ovine brain (M.T., with four years of experience). White matter tracts were identified on the basis of the ovine neuroanatomical literature (Clarke and Whitteridge, 1976;Bortolami and Callegari, 2001;Barone 2010;Ozdemir, 2015;John et al., 2017), human DTI atlas (Wakana et al., 2004;Catani and Thiebaut de Schotten, 2008) and gross dissections of ovine brain (Grisham, 2006). ROIs were selected to encompass the tract cross-section and were labelled as *inclusive* for start tracking, both in forward ad in backward directions (Figure 2A-E). Raw tracts resulting from the first tracking procedure were then refined on the basis of anatomical knowledge, by removing eventual contaminating fibers with *exclusion* ROIs (Figure 2F). Five eloquent white matter tracts were reconstructed bilaterally in each sheep: corticospinal tract (CST), corpus callosum (CC), visual pathway (VP), fornix (FX) and occipitofrontal fasciculus (OF). These tracts were chosen as they represent the main fiber bundles of the ovine brain, that can be reconstructed for neurosurgical planning purposes in typical *in vivo* DTI studies. Fiber tracts were finally displayed as volumes in different colors, and were overlaid as binary masks onto the T1-weighted volumetric images of each sheep, previously coregistered with the DTI

sequence. These binary images were saved in the Surgical Navigation-compatible DICOM (Digital Imaging and Computing in Medicine) format of the Intellispace software.

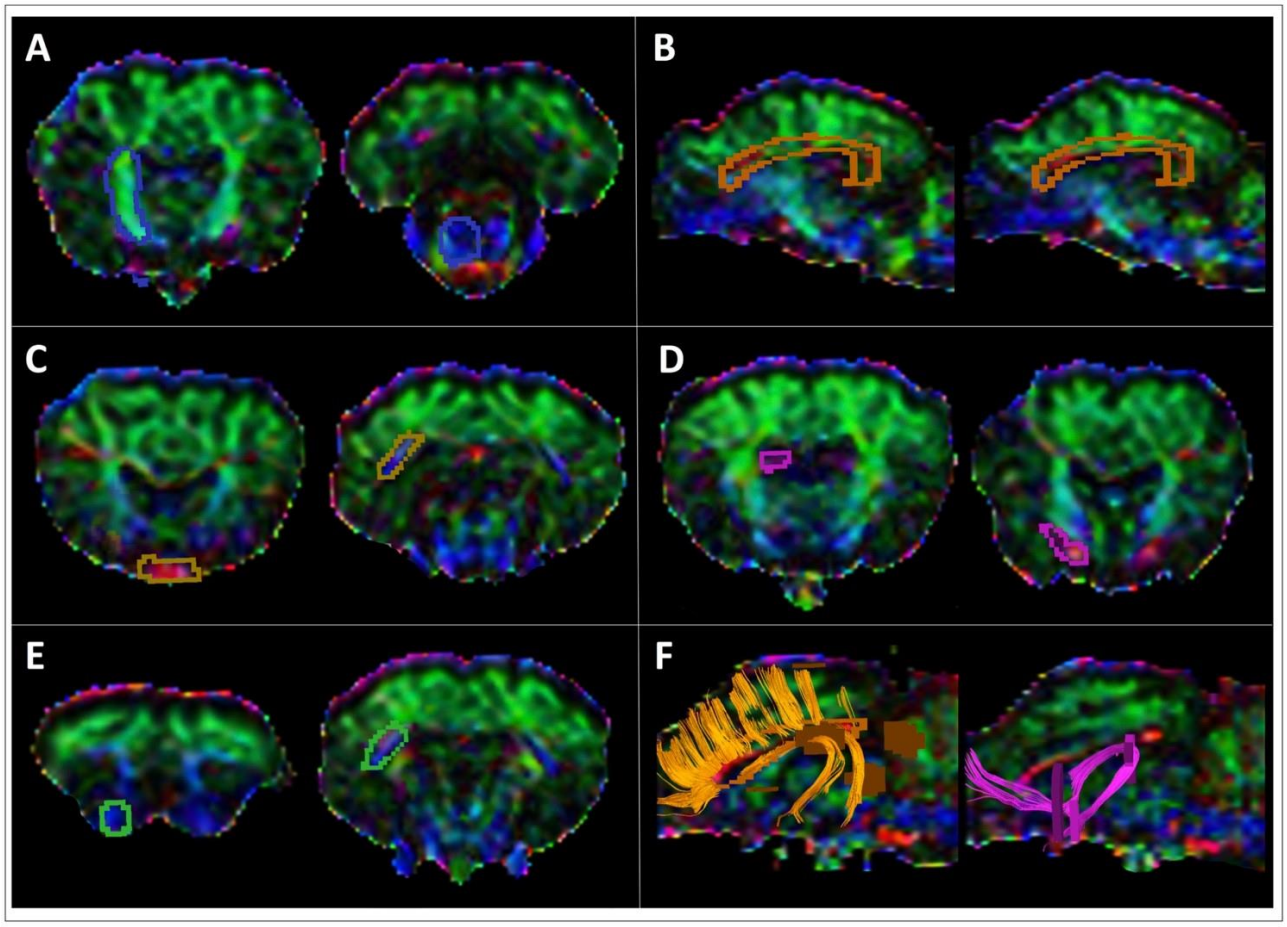

Figure 2 – Location of the ROIs for tractography reconstructions

Seed regions-of-interest (ROIs) for each tract were manually delineated on the color-coded directional FA maps. From these ROIs the deterministic tractography algorithm started reconstructing ovine WM tracts. The ROIs were contoured in precise anatomical positions selected to encompass the tract cross-section, according to the location of different fiber tracts. (A) ROIs for CST tractography reconstruction were placed on the transverse plane. The first ROI was placed in the genu of the internal capsule, that it is known to comprehend the ovine pyramidal tract and is found between the caudate nucleus and the putamen. The other ROI included the ventral mesencephalic plane, where the pons is located. (B) ROIs for CC tractography reconstruction were placed on the sagittal plane. ROIs were carefully positioned on two slices to contain a section of the fiber tract of interest in 3D space. In particular, the corpus callosum at the level of septum pellucidum was contoured by a ROI extending from the infrasplenial sulcus to the genual sulcus. (C) ROIs for VP tractography reconstruction were placed on the transverse plane. The ROI including the chiasm was set between the rostral encephalic longitudinal fissure and the posterior tuber cinereum. The optic radiations are known to run in the retrolentiform portion of the internal capsule and to diverge caudally before reaching the occipital cortex. Thus, a ROI has been placed just above the caudal portion of the lateral ventricle. (D) ROIs for FX tractography reconstruction were placed on the transverse plane. The first ROI encompassed the white matter medial to the genu of the internal capsule, rostral to the anterior horns of the lateral ventricles. The other ROI has been contoured posteriorly to the optic chiasm, external to the rostral arm of the internal capsule. (E) ROIs for OF tractography reconstruction were placed on the transverse plane. The rostral ROI was placed in the orbital gyrus, just posterior to the olfactory bulbs. The caudal ROI has been placed just above the caudal portion of the lateral ventricle, exactly as for the optic radiations that are known to be closely surrounded by the OF fibers. (F) Example of raw CC and FX tracts resulting from the first tracking procedures, that were successively refined by

inserting exclusion ROIs that allowed the removal of spurious fibers.

2.4 Ovine Brain Tractography Atlas creation

For each sheep, the DICOM images of the T1-weighted volumetric series and of the coregistered tracts' binary masks were converted to the NIfTI (Neuroimaging Informatics Technology Initiative) format using the dcm2nii tool (https://people.cas.sc.edu/rorden/mricron/dcm2nii.html). The whole brain of each sheep was extracted from the original T1-weighted volumetric images using the FMRIB Software Library (FSL, University of Oxford, https://fsl.fmrib.ox.ac.uk/fsl/) brain extraction tool (BET). Then, the original T1-weighted volumetric series of each sheep was registered to the publicly available T1- weighted stereotaxic ovine brain template developed by (Nitzsche et al., 2015) by using an affine transformation with the FLIRT tool of FMRIB Software Library (FSL, https://fsl.fmrib.ox.ac.uk/fsl/). The derived transformation matrix was consequently applied to all the reconstructed tracts. All the tracts in the stereotaxic atlas space were finally converted into binary mask images using ITK-SNAP (V3.6.0) software (http://www.itksnap.org/pmwiki/pmwiki.php). In each mask image, the voxels containing at least one streamline of the tract are associated with value 1, the others with value 0. The binary mask images of each tract in the stereotaxic space were eventually summed by means of the 'fslmaths' function of FSL into a single mask, representing voxel-by-voxel probability of the presence of the tract in the 10 animals, thus ranged between 0 and 10.

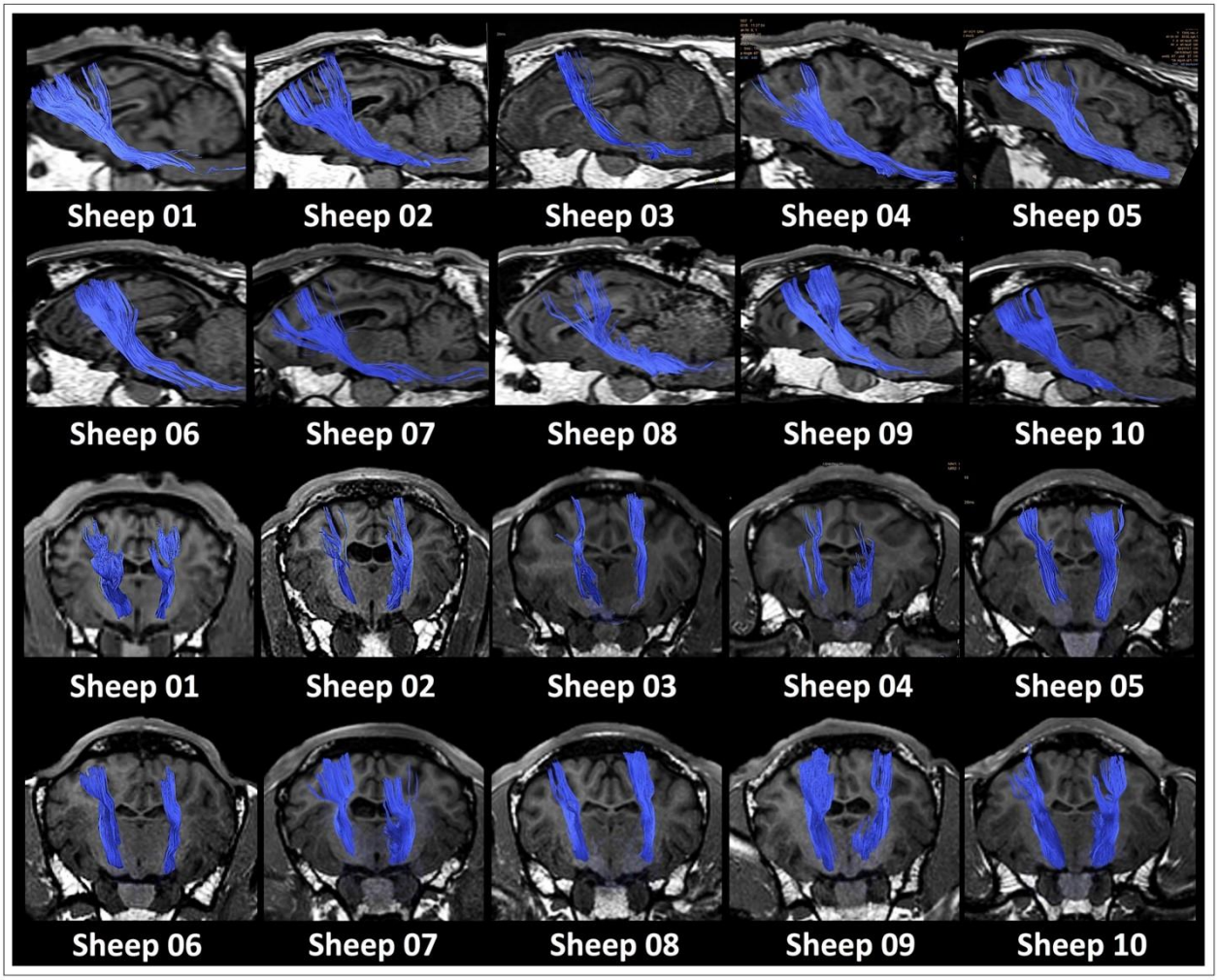

Figure 3 – Reproducibility of CST tractography reconstruction in all the 10 sheep

The anatomical course of the corticospinal tract (CST, blue) is shown as three-dimensional rendering in a sagittal (A) and frontal (B) view for each of the ten sheep. At a qualitative, visual assessment the course of tracts appears very similar across the 10 animals, thus highlighting the reproducibility of the tractography pipeline

3 Results

3.1 DTI Tractography analysis in individual sheep

DTI data acquisition was performed in all the ovine models, and DTI datasets were successfully post-processed in all the cases, allowing the *in vivo* dissection of the main projection, associative and commissural fibers in the ovine brain. Reconstruction of the corticospinal tract (CST), corpus callosum (CC), visual pathway (VP), fornix (FX) and occipitofrontal fasciculus (OF) was feasible in all the ten sheep. A detailed description of seed ROIs' position for each tract has been reported in Figure 2. The

course of tracts was reproducible and consistent across all the animals. Figure 3 shows an example of the whole anatomical course of the CST both in the sagittal and frontal view for each of the ten sheep, revealing a minimal inter-sheep variability at a qualitative, visual assessment.

3.1.1 Corticospinal tract (CST)

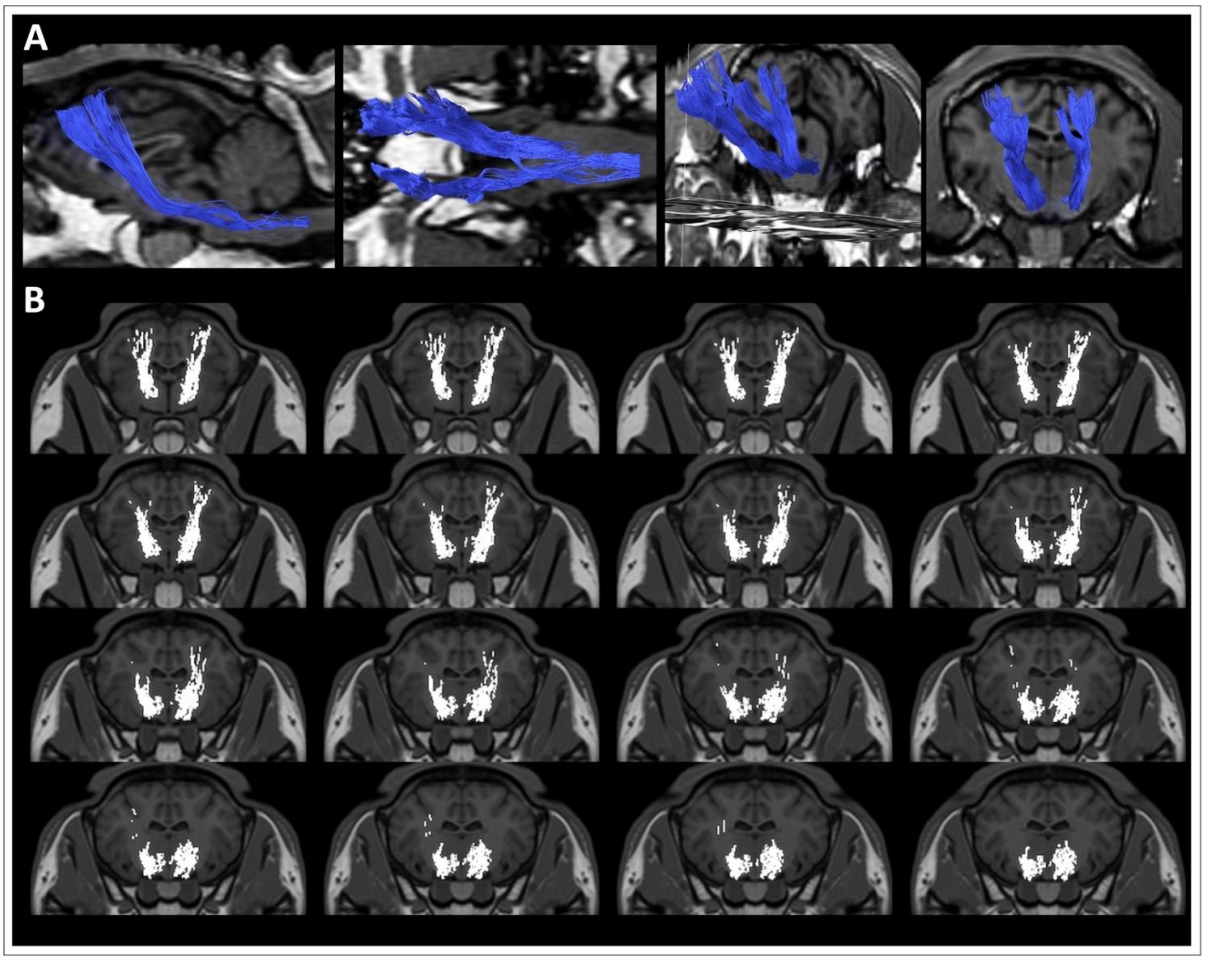

Figure 4 – Details of the course of the CST in a representative sheep

(A) CSTs are displayed as volumes on the corresponding T1-weighted anatomical image. (B) CSTs are overlaid as binary masks onto the T1-weighted volumetric images, previously coregistered with the DTI sequence by means of of the Local Correlation tool of the Philips IntelliSpace Portal software platform v8.0.

The ovine primary motor cortex lays in the precruciate gyrus, immediately anterior to the cruciate fissure, and the CST is the main efferent bundle that connects it to the spinal cord (Figure 3 and 4). Along its course, the CST reaches the corona radiata and its fibers intersect the radiation of the corpus callosum at the level of centrum semiovale. Then, it passes through the posterior limb of

the internal capsule and continues to the medial portion of cerebral peduncle, reaching the lateral funiculus. After the pontine nuclei, the white matter bundles converge in the pyramidal tract on the ventral bulbi surface.

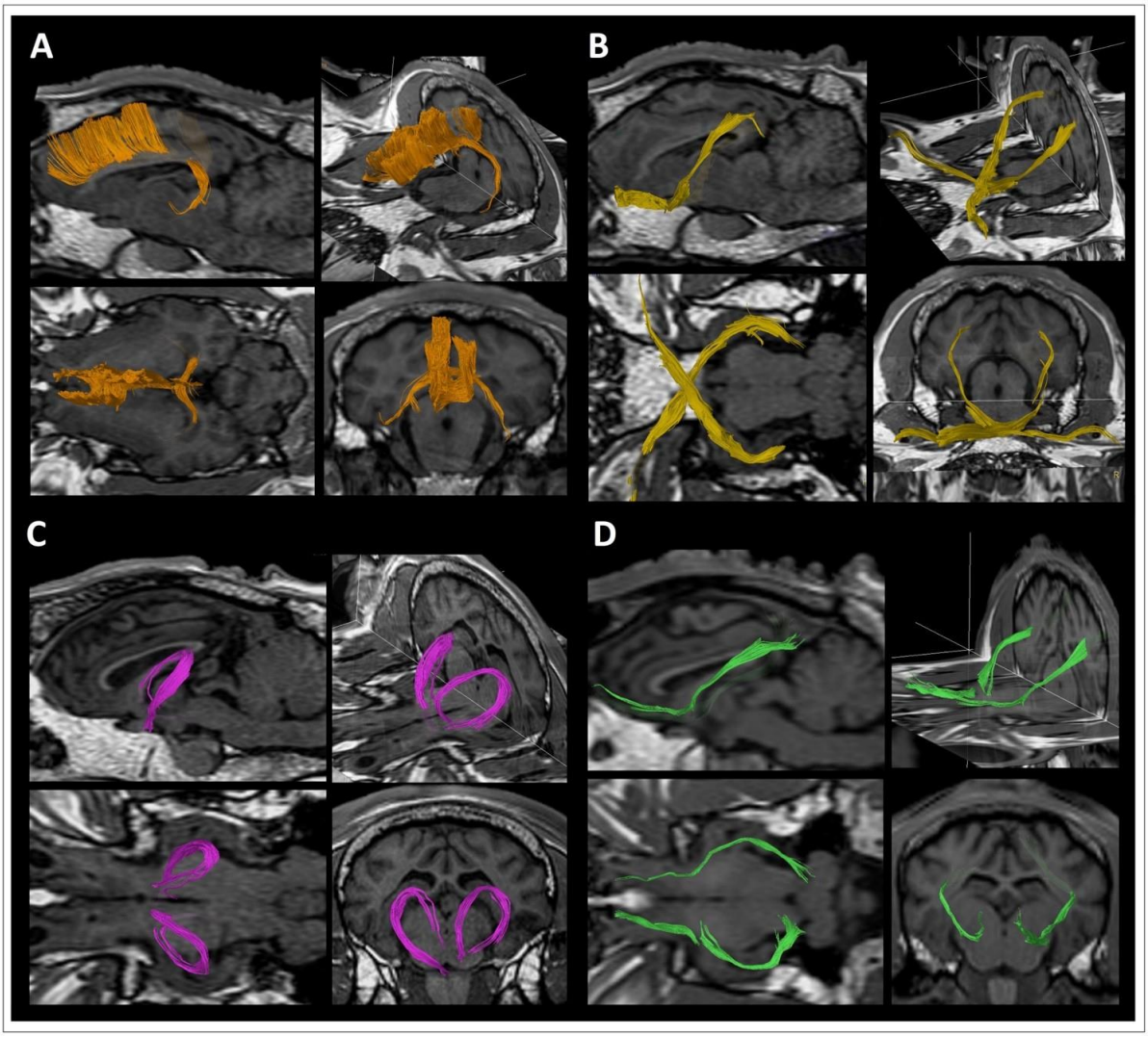

Figure 5 – Details of the course of the main ovine white matter fiber bundles in a representative sheep
Tracts are displayed as volumes onto high-resolution T1 anatomical images and showed in sagittal, lateral, coronal and transverse views (A) Corpus callosum (CC, orange): commissural bundle, connecting the right and left hemispheres, responsible for the integration between motor and cognitive functions. (B) Visual pathway (VP, yellow): constituted by the optic nerves, chiasm, optic tracts and optic radiations, responsible for visual function. (C) Fornix (FX, pink): part of the limbic system, responsible for memory-relatedfunctions. (D) Occipitofrontal fasciculus (OF, green): associative tract, whose precise function in sheep has not been exhaustively identified yet.

3.1.2 Corpus callosum (CC)

The ovine CC is a large band of fibers constituting the main commissural structure of the brain and it links homologous frontal motor areas from the two different hemispheres. Its medial part, the body, is located along the brain midline and forms the roof of large part of the lateral ventricles, then dispersing its fibers at the level of centrum semiovale, crossing the corona radiata. Anteriorly, the

genu of CC is identifiable as sharply bent white matter bundles, that narrow into the rostrum as the genu turns under. It connects the frontal cortex bilaterally, generating an arch path known as forceps minor. Posteriorly, the CC ends in the splenium: fiber bundles reach the parieto-occipital lobes bilaterally, generating an arch path known as forceps major that links parietal sensitive homologues areas. The callosal sulcus separates the CC from the adjacent midline cortex, the cingulate gyrus (Figure 5A).

3.1.3 Visual pathway (VP)

The VP in ovine crosses the brain rostro-caudally. Initially, the optic nerve connects the retina to the optic chiasm, which is surrounded by the Circle of Willis, allowing communications between the carotid and vertebral or basilar supplies to the brain. From the chiasm, optic tracts depart passing lateral to the cerebral peduncles and ending in the thalamic lateral geniculate nuclei (LGN). These nuclei constitute the thalamic receiving area for vision and are sidelong the medial geniculates, the thalamic relay nuclei for auditory fibers. From LGN, fibers are conveyed via the geniculocalcarine tract or optic radiation through the sublenticular portion of the internal capsule, and then to the primary visual cortex in the occipital lobe (Figure 5B).

3.1.4 Fornix (FX)

The FX is composed by an arch of fibers arising from the fimbria below the posterior portion of the corpus callosum and bending downward to dive below the surface, in route to the mammillary bodies. The FX constitutes part of the dorsal and rostral limit of the thalamus and is divided by a commissure which connects the two hippocampi, named commissure of fornix. Posteriorly, it is composed by two stripes of white matter that are known as fornix legs and are the extensions of the hippocampus fimbriae. Fornix legs continue rostrally forming the body of the fornix, which then creates two different ropes named fornix columns. The fornix columns proceed ventrally, ending the pathway into the corpi mamillari. The anterior arch of the fornix is adjacent to the anterior commissure, which connects the olfactory bulb, pyriform area and amygdala of the two hemispheres (Figure 5C).

3.1.5 Occipitofrontal fasciculus (OF)

The OF connects the frontal with the occipital lobe, starting rostral to the olfactory bulbs. It is found along the lateral border of the caudate nucleus and on the lateral aspect of the CST. After passing near the deep nuclei, under the external capsule and claustrum, it travels in contiguity with optic radiations and reaches the occipital cortex (Figure 5D).

3.2 The Ovine Brain Tractography Atlas

An ovine brain tractography atlas was successfully obtained by combining every single white matter tract of the ten animals. Figure 6 shows the resulting probability maps for each tract superimposed to the publicly available T1-weighted stereotaxic ovine brain template (Nitzsche et al., 2015). Representative slices are displayed, showing the main course of each tract in all the ten animals (Figure 6 A-E). Tract masks are color-encoded according to the number of animals in which the tract passes through each voxel. Voxel values range from 1 (meaning that the voxel is occupied by the tract of a single sheep) to progressive numbers the more the tract is consistent between the animals, up to a value of 10 in voxels occupied by the tracts of all the 10 sheep. The complete set of probability maps throughout the whole the rostro-caudal extent of the atlas is available for download at https://www.eden2020.eu/data-sets/. Intensity values can be visualized in gray or in color scales with FSLeyes (https://fsl.fmrib.ox.ac.uk/fsl/fslwiki/FSLeyes). As an example, in Figure 6 the intensity values are shown in color scales, excluding the voxels less consistent between the animal cohort. In fact, fixing the cutoff at 4 allows to visualize only the fibers that are consistent in at least 4 sheep out of 10.

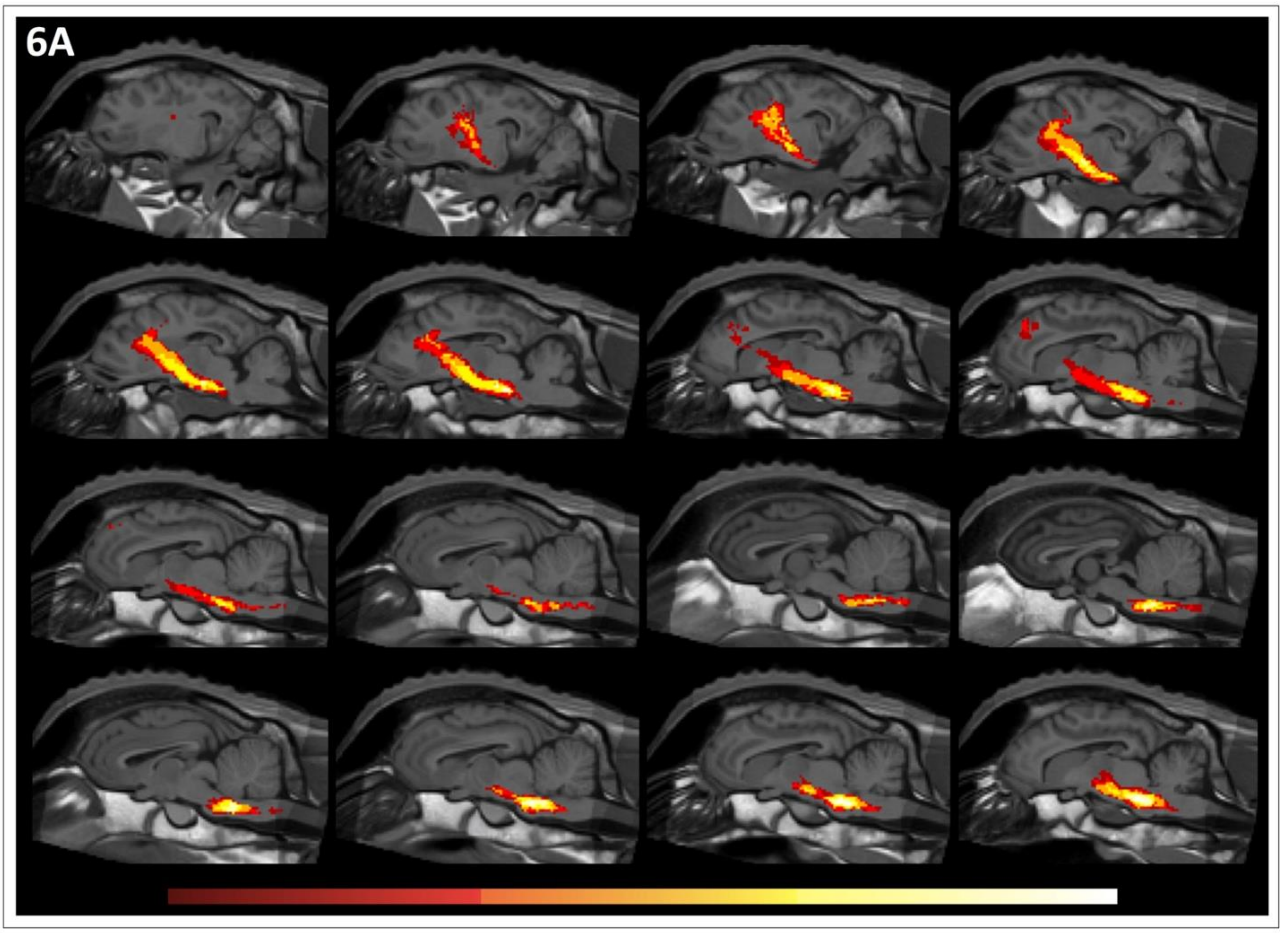
6A

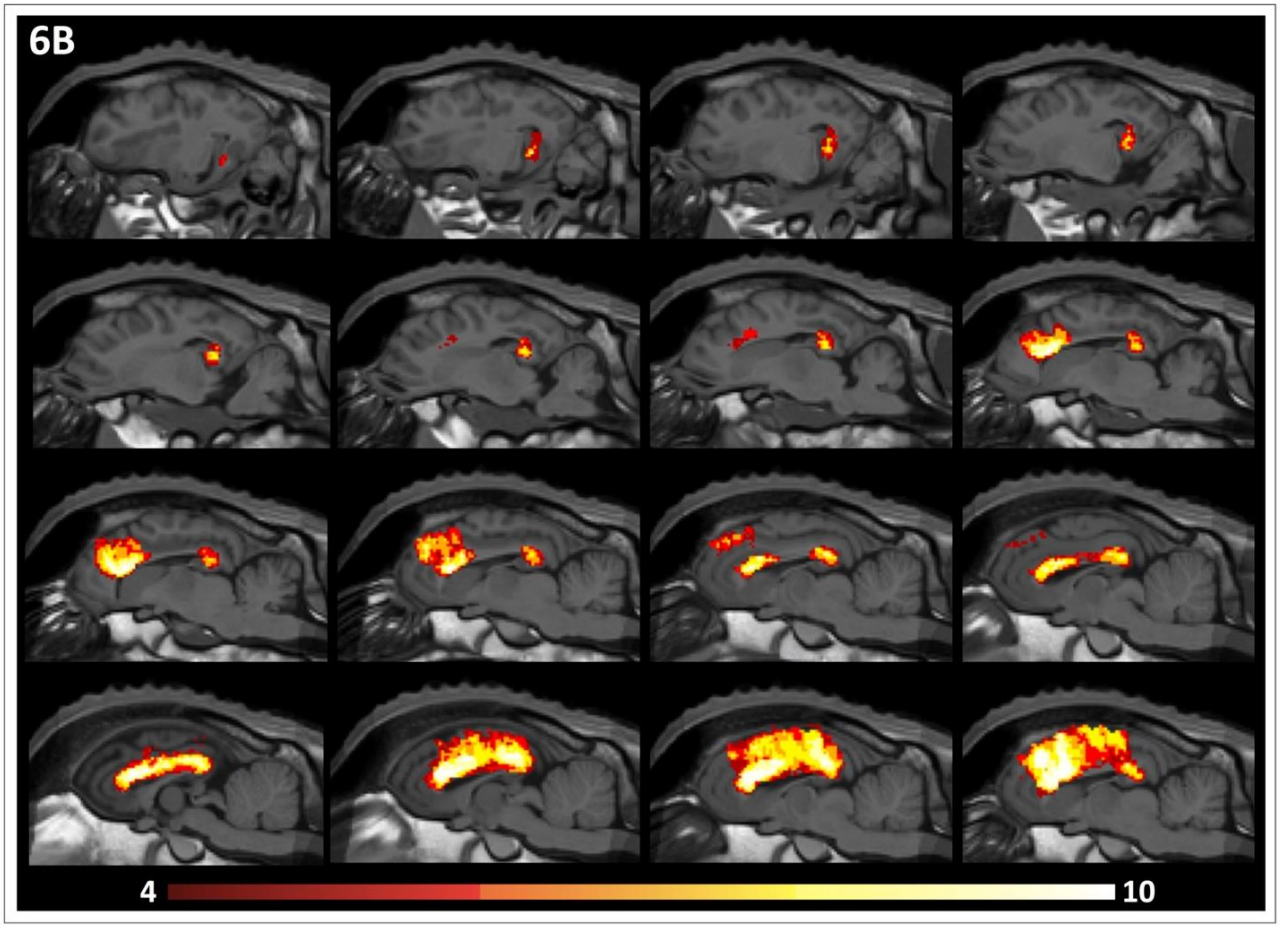
6B
4
10

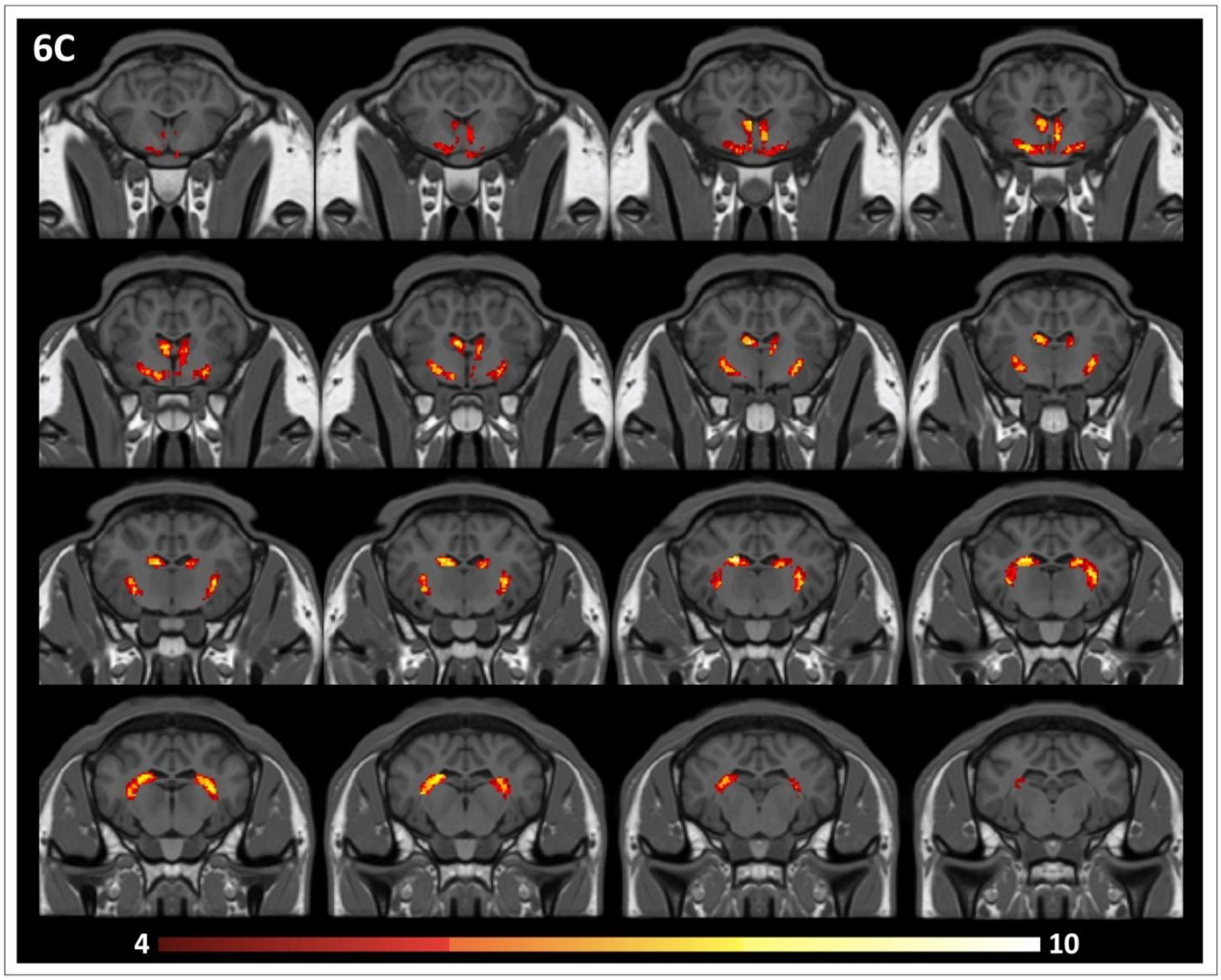

Figure 6 – Representative images from the ovine tractographic atlas

The tractography atlas of the five ovine tracts is visualized by means of FSLeyes in sagittal view for CST (6A) and CC (6B), transverse view for FX (6C) and coronal view for VP (6D) and OF (6E), overlaid onto the publicly available stereotaxic T1-weighted ovine brain atlas 0.5 mm. The origin of the reference system with the xyz- values (0;0;0) is a vertical line perpendicularly intersecting the superior aspect of the rostral commissure. All coordinates are given in millimeters (mm). Values of the x-axis increase from left to right, values of the y-axis increase from rostral to caudal, while values of the z-axis increase in the dorsal direction (Nitzsche, 2015).

(6A) sagittal view for CST: on x axis, from -12.9 to 5.1mm (slice spacing: 1.2mm)

(6B) sagittal view for CC: on x axis, from -14.6 to 3.4mm (slice spacing: 1.2mm)

(6C) transverse view for FX: on y axis, from 3.65 to -17.35mm (slice spacing: 1.4mm)

(6D) coronal view for VP: on z axis, from -11.1 to 15.9mm (slice spacing: 1.8mm)

(6E) coronal view for OF: on z axis, from -6.225 to 17.025mm (slice spacing: 1.55 mm)

A binary mask of each tract was firstly obtained from every sheep. The binary mask images of each tract in the stereotaxic space were summed into a single mask, in which the value of every voxel represents the number of animals in which the tract passes trough that voxel. By fixing the cutoff value at 4, only the fibers that are consistent in at least 4 sheep out of 10 are shown

4 Discussion

In this work we demonstrate the feasibility of a protocol to perform in vivo DTI tractography of the sheep model, providing a reliable reconstruction and 3D rendering of major ovine fiber tracts responsible for different functions. A detailed pipeline for DTI data acquisition, preprocessing and analysis, as well as for the identification of seed ROIs for tractography, has been implemented in order to reconstruct the location and trajectory of five eloquent white matter tracts representative of the main fiber bundles included in typical *in vivo* DTI studies, namely the corticospinal tract (CST), corpus callosum (CC), visual pathway (VP), fornix (FX) and occipitofrontal fasciculus (OF). In fact, exclusively the ovine motor pathway (Lee et al., 2015;Peruffo et al., 2019) and optic radiations (Lee et al., 2015) have been previously described in DTI studies on the sheep model, with a limited number of subjects. Our analysis improved the anatomical understanding of the normal appearance of these ovine white matter bundles and allowed a comparison to the homologous structures of human and other mammals, which is pivotal for the translational purpose of using sheep models in neuroscience. Indeed, white matter fibers have been conventionally classified into different categories depending on their paths, both in humans and in animals (Jacqmot et al., 2013;Anaya Garcia et al., 2015). For instance, tracts in the brainstem comprise the motor fibers of the CST and its cerebellar connections, while projection fibers include the suprathalamic portion of CST that connects cortical to subcortical white matter. With respect to the other primates, the CST in sheep is smaller and composed of thinner fibers (John et al., 2017). It is interesting to highlight that the ovine motor cortex is mesial, constituted by the precruciate gyrus that is located before the cruciate fissure. The latter corresponds to the human fissure of Rolando or central sulcus, and intersects the medial longitudinal fissure to mark off the anterior third of the cortex (Grisham, 2006). Due to the para-sagittal disposition of the motor cortex, along the longitudinal fissure, the sheet of the corona radiata can be appreciated on the sagittal plane. Conversely, the human motor cortex extends along the central sulcus in the precentral gyrus, thus the corona radiata fans out in an arc on the coronal plane (Wakana et al., 2004). Another white matter category includes commissural tracts that connect the right and left hemispheres and are responsible both for homologous and heterotopic associations, as the CC. It consists of a flat bundle of fibers both in sheep and humans, spanning part of the longitudinal fissure (Barone 2010). Additional eloquent tracts that we managed to reconstruct in the ovine model are the VP for the eyesight and the FX, that is part of the limbic system. In the ovine VP, the same components that carry visual information from

the environment to the brain in humans are identifiable, including the optic nerve, optic chiasm, optic tract, lateral geniculate nucleus, optic radiations and visual cortex, located in the occipital lobe as already described in the literature (Clarke and Whitteridge, 1976). Notably, the percentage of fibers that do not cross in the contralateral optic tract represents a recent filogenetic acquisition that allows a stereoscopic vision, thus it reaches only 11% in ovine, while 47% in humans (Barone 2010). Moreover, in sheep, a small supplementary bundle of fibers defined as *fasciculus paraopticus* runs along the medial margin of the optic tract. It groups fibers coming from the contralateral retina and can be considered an isolated portion of the medial root of the optic tract (Barone 2010). As far as the FX is concerned, it appears particularly trophic in sheep and emerges from the hippocampus as a C-shaped fiber bundle. It carries fibers from the hippocampus to the mammillary bodies (via the postcommissural fornix) and septal nuclei (via the precommissural fornix), and fibers from septal nuclei to hippocampus, thus seeming associated to sheep memory formation (Barone 2010), exactly as in humans. Eventually, a further category of white matter bundles is represented by the associative fibers, that connect two different cortical areas. In humans, they include the Inferior Fronto Occipital Fascicle, Uncinate Fascicle, Cingulum, Inferior Longitudinal fascicle, Superior Longitudinal Fascicle and Arcuate Fascicle, and are responsible for higher functions such as language production and comprehension. Since associative fibers have been described in dogs (Jacqmot et al., 2013;Anaya Garcia et al., 2015) bovines (Yaman et al., 2014) and dolphins (Wright et al., 2018), we expected to find the OF also in sheep, even if its precise function has not been completely elucidated in animals. Our study also aimed at evaluating the reproducibility of the sheep tractography pipeline. To this end, it was firstly figured out that the ROIs identified as appropriate seeds for the tracking algorithm could be consistently contoured in every animal, by taking into account an accurate examination of the prior knowledge on sheep neuroanatomy (Clarke and Whitteridge, 1976;Bortolami and Callegari, 2001;Barone 2010;Ozdemir, 2015;John et al., 2017), human DTI atlas (Wakana et al., 2004;Catani and Thiebaut de Schotten, 2008) and gross dissections of ovine brain (Grisham, 2006). At a qualitative, visual assessment the course of tracts appears very similar across the 10 animals, thus highlighting the reproducibility of the tracking pipeline, adding strength and consistency to our findings.

Furthermore, in order to precisely quantify inter-sheep similarity and to provide an information regarding the average position of each tract and the normal variability across sheep, the ten individual MRI datasets were separately analyzed and then coregistered to a publicly available stereotaxic T1- weighted ovine brain atlas (Nitzsche et al., 2015) in a standard coordinate system.

A population- averaged atlas representing the five most eloquent white matter ovine fiber bundles was generated, providing a standard sheep brain tractography template that can be easily overlaid onto the aforementioned reference space. As confirmed by many researchers (Ella and Keller, 2015), the possibility to integrate our tractography reconstructions into other publicly available databases is of striking significance, since the availability of a common reference space for standardization is the basis for any future significant neuroimaging study. In fact, the atlas would offer to veterinaries and researchers the possibility to incorporate tractography in the study of numerous brain diseases in the ovine translational models, even if DTI acquisitions are not available. For example, Staudacher et al. pointed out that new technologies and tools are needed to improve the accuracy in brainstem biopsies essential for histopathological diagnoses (Staudacher et al., 2014), and the atlas could be fundamental to this purpose, precisely locating the CST pyramids. Furthermore, despite the possibility to identify ischemic injuries in ovine white matter by means of conventional MRI (Ferriero, 2006;Fraser et al., 2007), tractography would add specificity to the study of the complex pathophysiology of white matter damages, allowing researchers to focus their analyses on the core of the fiber bundles. From a more general perspective, then, the tractography atlas will facilitate the localization of different sheep cortical areas, implementing future studies on acute mapping procedures and possibly allowing the recording of motor potentials besides the sensory ones elicited by Gierthmuehlend et al. in a recent study (Gierthmuehlen et al., 2014).

Key features of the proposed tractography atlas include also its versatility and adaptability to various clinical contexts. Indeed, the atlas consists in masks of white matter tracts that are not binary, but that are weighted from 1 to 10 according to the number of fiber bundles present in every specific voxel. The comprehensive tract masks that we generated for CST, CC, VP, FX and OF, in fact, derived from the sum of the corresponding fibers of 10 individual sheep previously coregistered to the same reference space. Therefore, their central core resulted common to all the animals, while subtle anatomical variations could be appreciated for more external fibers. Specifically, all the comprehensive masks can be thresholded for any value from 1 to 10 according to particular experimental needs, so to visualize and consider different levels of inter-subject variability. As an example, in the field of neurosurgical research, presurgical planning on sheep must be precisely tuned depending on the final aim of the procedure, both in the clinical veterinary routine as well as in experimental settings, in order to faithfully reproduce the human patient scenario. On one hand, if the ultimate goal of the surgery is to precisely target WM tracts with

electrical stimulation, the operator would probably want to consider only fibers that we tracked in 8-10 out of the total of 10 sheep, to rely just on the tract portion more preserved across different animals. The study conducted by Stypulkowski et al. represents a fitting example in which the tractography atlas would have been valuable, since they stimulated the Papez circuit with deep brain stimulation (DBS) targeting the fornix only on the basis of anatomical notions, without the specificity of tractography reconstructions (Stypulkowski et al., 2017).

On the other hand, if the final purpose of the procedure is to safely remove a mass lesion without compromising the sheep's quality of life, the operator would probably prefer to consider all the possible fibers passing through the area of interest, to remain more conservative and spare eloquent structures.

For example, the atlas could intriguingly implement the cerebral tumor model based on the injection of agar into sheep brain, proposed by Kamp et al. for the training of young neurosurgeons (Kamp et al., 2015). In this case, the mask threshold can be fixed around 3, in order to visualize white matter fibers present in at least 3 sheep out of the total of 10, to compute a realistic integration of WM obstacles in the simulation setting and to challenge neurosurgeons in sparing pivotal functions such as movement and vision. Ultimately, regardless of the context-dependent mask-threshold chosen by the operator, a detailed representation of white matter structures is essential for the study of many brain pathologies, from developmental ones to degenerative ones, so the exploitation of our atlas could be precious in several contexts, both for translational research in humans and in the veterinary application *per se*.

A possible limitation of this study relies on the clinically-compatible MRI acquisitions on a 1.5T scanner, that may impede to depict fine anatomical details of the tracts. Recent studies have exploited DTI at 3T for tractography of white matter tracts of large animal models (Jacqmot et al., 2013;Lee et al., 2015;Wright et al., 2018). However, 3T scanners are rarely available for veterinary cases. Nonetheless, in our study high-quality images have been obtained in clinically compatible scanning duration, without the need of keeping the sheep anesthetized for long time. Both diffusion maps and tractography reconstructions have been feasible with our datasets, and can be easily implemented in preclinical studies aimed at evaluating multiple time-points *in vivo* in an experimental setting resembling a clinical scenario.

Finally, the possible inaccuracy derived from anatomical variability of the animals may be improved even considering other ovine breeds. Future investigation will be aimed at exploring the degree

of heterogeneity in brain anatomy between different ovine varieties, possibly leading toward a more accurate representation of pivotal neuroanatomical structures in exceptionally detailed atlases (Liyanage et al., 2016).

5 Conclusion

The present work built an innovative ovine tractography atlas, demonstrating that multiple white matter fiber tracts can be consistently reconstructed in sheep. Minimal inter-subject variability proves the reproducibility of our image post-processing, ROIs identification and fiber tracking. Additionally, the population-averaged atlas can be integrated into publicly available imaging software, paving the way toward space standardization of ovine imaging analyses. It will enable to design homogeneous studies considering the direction and reciprocal position of white matter fiber bundles, that will significantly support the meticulous study of numerous brain pathologies. In conclusion, the ovine tractography atlas can be considered as a valuable tool to implement the knowledge of sheep's brain anatomy and to improve the activity of clinicians and researchers using this animal model in neuroscience studies.

6 Acknowledgments

This work has been carried out in the context of the EDEN2020 (Enhanced Delivery Ecosystem for Neurosurgery in 2020) project, that received funding from the European Union's EU Research and Innovation programme Horizon 2020 under Grant Agreement no. 688279.

7 References

Anaya Garcia, M.S., Hernandez Anaya, J.S., Marrufo Melendez, O., Velazquez Ramirez, J.L., and Palacios Aguiar, R. (2015). In vivo study of cerebral white matter in the dog using diffusion tensor tractography. *Vet Radiol Ultrasound* 56**,** 188-195.

Barone , R. (2010). *Anatomie comparée des mammifères domestiques : Tome 6, Neurologie I.* Bologna: Edagricole.

Basser, P.J., and Pierpaoli, C. (1996). Microstructural and physiological features of tissues elucidated by quantitative-diffusion-tensor MRI. *J Magn Reson B* 111**,** 209-219.

Berns, G.S., Cook, P.F., Foxley, S., Jbabdi, S., Miller, K.L., and Marino, L. (2015). Diffusion tensor imaging of dolphin brains reveals direct auditory pathway to temporal lobe. *Proc Biol Sci* 282.

Bortolami , R., and Callegari, E. (2001). *Neurologia ed estesiologia degli animali domestici* Bologna: Edagricole. Capitanio, J.P., and Emborg, M.E. (2008). Contributions of non-human primates to neuroscience research. *Lancet* 371**,** 1126-1135.

Catani, M., and Thiebaut De Schotten, M. (2008). A diffusion tensor imaging tractography atlas for virtual in vivo dissections. *Cortex; a journal devoted to the study of the nervous system and behavior* 44**,** 1105-1132.

Clarke, P.G., and Whitteridge, D. (1976). The cortical visual areas of the sheep. *J Physiol* 256**,** 497- 508.

Dai, J.K., Wang, S.X., Shan, D., Niu, H.C., and Lei, H. (2017). A diffusion tensor imaging atlas of white matter in tree shrew. *Brain Struct Funct* 222**,** 1733-1751.

Dai, J.X., Ma, Y.B., Le, N.Y., Cao, J., and Wang, Y. (2018). Large animal models of traumatic brain injury. *Int J Neurosci* 128**,** 243-254.

Ella, A., Delgadillo, J.A., Chemineau, P., and Keller, M. (2017). Computation of a high-resolution MRI 3D stereotaxic atlas of the sheep brain. *J Comp Neurol* 525**,** 676-692.

Ella, A., and Keller, M. (2015). Construction of an MRI 3D high resolution sheep brain template. *Magn Reson Imaging* 33**,** 1329-1337.

Ferriero, D.M. (2006). Can we define the pathogenesis of human periventricular white-matter injury using animal models? *J Child Neurol* 21**,** 580-581.

Finnie, J. (2001). Animal models of traumatic brain injury: a review. *Aust Vet J* 79**,** 628-633.

Fraser, M., Bennet, L., Helliwell, R., Wells, S., Williams, C., Gluckman, P., Gunn, A.J., and Inder, T. (2007). Regional specificity of magnetic resonance imaging and histopathology following cerebral ischemia in preterm fetal sheep. *Reprod Sci* 14**,** 182-191.

Gierthmuehlen, M., Wang, X., Gkogkidis, A., Henle, C., Fischer, J., Fehrenbacher, T., Kohler, F., Raab, M., Mader, I., Kuehn, C., Foerster, K., Haberstroh, J., Freiman, T.M., Stieglitz, T., Rickert, J., Schuettler, M., and Ball, T. (2014). Mapping of sheep sensory cortex with a novel microelectrocorticography grid. *J Comp Neurol* 522**,** 3590-3608.

Grisham, W. (2006). Resources for teaching Mammalian neuroanatomy using sheep brains: a review. *J Undergrad Neurosci Educ* 5**,** R1-6.

Harsan, L.A., Paul, D., Schnell, S., Kreher, B.W., Hennig, J., Staiger, J.F., and Von Elverfeldt, D.

(2010). In vivo diffusion tensor magnetic resonance imaging and fiber tracking of the mouse brain. *NMR Biomed* 23**,** 884-896.

Hutchinson, E.B., Schwerin, S.C., Radomski, K.L., Irfanoglu, M.O., Juliano, S.L., and Pierpaoli, C.M. (2016). Quantitative MRI and DTI Abnormalities During the Acute Period Following CCI in the Ferret. *Shock* 46**,** 167-176.

Hutchinson, E.B., Schwerin, S.C., Radomski, K.L., Sadeghi, N., Jenkins, J., Komlosh, M.E., Irfanoglu, M.O., Juliano, S.L., and Pierpaoli, C. (2017). Population based MRI and DTI templates of the adult ferret brain and tools for voxelwise analysis. *Neuroimage* 152**,** 575-589.

Jacqmot, O., Van Thielen, B., Fierens, Y., Hammond, M., Willekens, I., Van Schuerbeek, P., Verhelle, F., Goossens, P., De Ridder, F., Clarys, J.P., Vanbinst, A., and De Mey, J. (2013). Diffusion tensor imaging of white matter tracts in the dog brain. *Anat Rec (Hoboken)* 296**,** 340-349.

Jiang, Y., and Johnson, G.A. (2010). Microscopic diffusion tensor imaging of the mouse brain. *Neuroimage* 50**,** 465-471.

John, S.E., Lovell, T.J.H., Opie, N.L., Wilson, S., Scordas, T.C., Wong, Y.T., Rind, G.S., Ronayne, S., Bauquier, S.H., May, C.N., Grayden, D.B., O'brien, T.J., and Oxley, T.J. (2017). The ovine motor cortex: A review of functional mapping and cytoarchitecture. *Neurosci Biobehav Rev* 80**,** 306-315.

Kamp, M.A., Knipps, J., Steiger, H.J., Rapp, M., Cornelius, J.F., Folke-Sabel, S., and Sabel, M. (2015). Training for brain tumour resection: a realistic model with easy accessibility. *Acta Neurochir (Wien)* 157**,** 1975-1981; discussion 1981.

Karageorgos, L., Hein, L., Rozaklis, T., Adams, M., Duplock, S., Snel, M., Hemsley, K., Kuchel, T., Smith, N., and Hopwood, J.J. (2016). Glycosphingolipid analysis in a naturally occurring ovine model of acute neuronopathic Gaucher disease. *Neurobiol Dis* 91**,** 143-154.

Le Bihan, D. (2014). Diffusion MRI: what water tells us about the brain. *EMBO Mol Med* 6**,** 569-573.

Lee, W., Lee, S.D., Park, M.Y., Foley, L., Purcell-Estabrook, E., Kim, H., and Yoo, S.S. (2015). Functional and diffusion tensor magnetic resonance imaging of the sheep brain. *BMC Vet Res* 11**,** 262.

Li, J., Li, X.Y., Feng, D.F., and Gu, L. (2011). Quantitative evaluation of microscopic injury with diffusion tensor imaging in a rat model of diffuse axonal injury. *Eur J Neurosci* 33**,** 933-945.

Liyanage, K.A., Steward, C., Moffat, B.A., Opie, N.L., Rind, G.S., John, S.E., Ronayne, S., May, C.N., O'brien, T.J., Milne, M.E., and Oxley, T.J. (2016). Development and Implementation of a Corriedale Ovine Brain Atlas for Use in Atlas-Based Segmentation. *PLoS One* 11**,** e0155974.

Makris, N., Kennedy, D.N., Boriel, D.L., and Rosene, D.L. (2010). Methods of MRI-based structural imaging in the aging monkey. *Methods* 50**,** 166-177.

Mori, S., and Van Zijl, P.C. (2002). Fiber tracking: principles and strategies - a technical review. *NMR Biomed* 15**,** 468-480.

Morosanu, C.O., Nicolae, L., Moldovan, R., Farcasanu, A.S., Filip, G.A., and Florian, I.S. (2019).

approaches and techniques - a systematic review of the current literature. *Neurol Neurochir Pol* 53**,** 8-

Murray, S.J., Black, B.L., Reid, S.J., Rudiger, S.R., Simon Bawden, C., Snell, R.G., Waldvogel, H.J., and Faull, R.L.M. (2019). Chemical neuroanatomy of the substantia nigra in the ovine brain. *J Chem Neuroanat* 97**,** 43-56.

Nestler, E.J., and Hyman, S.E. (2010). Animal models of neuropsychiatric disorders. *Nat Neurosci* 13**,** 1161-1169.

Nitzsche, B., Frey, S., Collins, L.D., Seeger, J., Lobsien, D., Dreyer, A., Kirsten, H., Stoffel, M.H., Fonov, V.S., and Boltze, J. (2015). A stereotaxic, population-averaged T1w ovine brain atlas including cerebral morphology and tissue volumes. *Front Neuroanat* 9**,** 69.

Oguz, I., Mcmurray, M.S., Styner, M., and Johns, J.M. (2012). The translational role of diffusion tensor image analysis in animal models of developmental pathologies. *Dev Neurosci* 34**,** 5-19.

Ozdemir, N.G. (2015). The Anatomy of the Posterior Commissure. *Turk Neurosurg* 25**,** 837-843.

Pajevic, S., and Pierpaoli, C. (1999). Color schemes to represent the orientation of anisotropic tissues from diffusion tensor data: application to white matter fiber tract mapping in the human brain. *Magn Reson Med* 42**,** 526-540.

Perentos, N., Nicol, A.U., Martins, A.Q., Stewart, J.E., Taylor, P., and Morton, A.J. (2017). Techniques for chronic monitoring of brain activity in freely moving sheep using wireless EEG recording. *J Neurosci Methods* 279**,** 87-100.

Peruffo, A., Corain, L., Bombardi, C., Centelleghe, C., Grisan, E., Graic, J.M., Bontempi, P., Grandis, A., and Cozzi, B. (2019). The motor cortex of the sheep: laminar organization, projections and diffusion tensor imaging of the intracranial pyramidal and extrapyramidal tracts. *Brain Struct Funct* 224**,** 1933-1946.

Rane, S., Nair, G., and Duong, T.Q. (2010). DTI at long diffusion time improves fiber tracking. *NMR Biomed* 23**,** 459-465.

Reid, S.J., Mckean, N.E., Henty, K., Portelius, E., Blennow, K., Rudiger, S.R., Bawden, C.S., Handley, R.R., Verma, P.J., Faull, R.L.M., Waldvogel, H.J., Zetterberg, H., and Snell, R.G. (2017). Alzheimer's disease markers in the aged sheep (Ovis aries). *Neurobiol Aging* 58**,** 112-119.

Staudacher, A., Oevermann, A., Stoffel, M.H., and Gorgas, D. (2014). Validation of a magnetic resonance imaging guided stereotactic access to the ovine brainstem. *BMC Vet Res* 10**,** 216.

Stypulkowski, P.H., Stanslaski, S.R., and Giftakis, J.E. (2017). Modulation of hippocampal activity with fornix Deep Brain Stimulation. *Brain Stimul* 10**,** 1125-1132.

Stypulkowski, P.H., Stanslaski, S.R., Jensen, R.M., Denison, T.J., and Giftakis, J.E. (2014). Brain stimulation for epilepsy--local and remote modulation of network excitability. *Brain Stimul* 7**,** 350-358.

Takahashi, E., Dai, G., Rosen, G.D., Wang, R., Ohki, K., Folkerth, R.D., Galaburda, A.M., Wedeen,

V.J., and Ellen Grant, P. (2011). Developing neocortex organization and connectivity in cats revealed by direct correlation of diffusion tractography and histology. *Cereb Cortex* 21**,** 200-211.

Uematsu, A., Hata, J., Komaki, Y., Seki, F., Yamada, C., Okahara, N., Kurotaki, Y., Sasaki, E., and Okano, H. (2017). Mapping orbitofrontal-limbic maturation in non-human primates: A longitudinal magnetic resonance imaging study. *Neuroimage* 163**,** 55-67.

Van Camp, N., Blockx, I., Camon, L., De Vera, N., Verhoye, M., Veraart, J., Van Hecke, W., Martinez, E., Soria, G., Sijbers, J., Planas, A.M., and Van Der Linden, A. (2012). A complementary diffusion tensor imaging (DTI)-histological study in a model of Huntington's disease. *Neurobiol Aging* 33**,** 945-959.

Wakana, S., Jiang, H., Nagae-Poetscher, L.M., Van Zijl, P.C., and Mori, S. (2004). Fiber tract-based

Winston, G.P. (2012). The physical and biological basis of quantitative parameters derived from diffusion MRI. *Quant Imaging Med Surg* 2**,** 254-265.

Wright, A.K., Theilmann, R.J., Ridgway, S.H., and Scadeng, M. (2018). Diffusion tractography reveals pervasive asymmetry of cerebral white matter tracts in the bottlenose dolphin (Tursiops truncatus). *Brain Struct Funct* 223**,** 1697-1711.

Yaman, M., Izdes, M., Şentürk, S., Ozturk, Y., and Kazanci, A. (2014). *Fiber Dissection Training Model for Neurosurgical Practice: White Matter Fiber Dissection with Klingler's technique in Bovine Brain.*

Supplementary Material

1 Supplementary Tables

1.1 Supplementary Table 1 - Example of the detailed ethogram

For all sheep, a dedicated ethogram was daily filled in during the entire housing period. Detailed scores for clinical and physiological parameters were reported in order to guarantee the animal wellbeing and to intervene if the animal balance is compromised

Date **Sheep n°** **Weight**	**Score**	**Date/Hour**
Sensorium	0/3	
Eating	Y/N	
Ruminating	Y/N	
Drinking	Y/N	
Lameness	0-3	
Rectal Temperature (39-40°C)	0/3	
Respiratory frequency (12-20 breaths per min)	0/3	
Cardiac frequency (70-80 beat per min)	0/3	
Body condition score (BCS)*	0/5	

Table legend on animal welfare (degree of severity):

- Sensorium: Normal: 0 = no grade (normal behaviour), 1= low activity (reduction of motility, lethargy), 2 = no activity (stillness or reluctance to move), 3 = persistent decubitus or coma
- Lameness: 0 = no grade, 1 = mild, 2 = moderate, 3= severe
- Body temperature: 0 = normothermia, 1 = hypothermia, 2 = hyperthermia
- Respiratory frequency: 0 = eupneic, 1 = bradypneic, 2 = tachypneic, 3 = dyspneic
- Cardiac frequency: 0 = normocardia 1= bradycardia, 2=tachycardia, 3=tachyarrhythmia 677
- Y/N= YES/NO
- *BSC: 0 = emaciated, 1 = very thin, 2 = thin, 3 = moderate (ideal), 4 = fleshy, 5 = very fleshy

1.2 Supplementary Table 2 – Complete MRI protocol acquired in sheep

Technical parameters of the MR sequences acquired in sheep are herein reported

	3D T1	T 2	SWI	PCA	TOF HR	DTI15
Sequence	sT1w_3D_FFE	T2W_TSE	SWIp	s3D_PCA_SAG	TOF	DTI15
TR (ms)	25	7557	52	12	25	6700
TE (ms)	5	110	0	7	7	84
Flip Angle	40	90	20	10	20	90
Acquisition Matrix	288x288	512x512	192x192	256x256	320X320	96x96
Voxel size (mm)	0.667x0.667	0.314x0.314	1x1	0.898x0.898	0.562x0.562	2x2
Slice Thickness (mm)	1.4	3	2	1.6	1.2	2
Slice number	150	34	56	76	120	45
SENSE factor	2	1	2	1.8	2	2
***b*-value (s/mm^2)**	-	-	-	-	-	0 1000 (15 dir)
Acquisition Time	8 min 40 sec	5 min 41 sec	4 min 34 sec	3 min 52 sec	4 min 5 sec	5 min 34 sec

Cytoarchitecture of commissural, association and projection fibres: a comparative study

(the manuscript reported here is still in preparation)

Cytoarchitecture of commissural, association and projection fibres: a comparative study

Andrea Bernardini[1] and Marco Trovatelli[2], Michal Klosowski[3], Matteo Pederzani[4], Fabio Acocella[2], Davide Danilo Zani[5], Stefano Brizzola[5], Alexandra Porter[1], Ferdinando Rodriguez y Baena[1], Daniele Dini[1*]

[1]Department of Mechanical Engineering, Imperial College London – UK
[2]Department of Health, Animal Science and Food Safety, Università degli Studi di Milano, Italy
[3]Department of Mechanical Materials, Imperial College London – UK
[5]Department of Veterinary Medicine, Università degli Studi di Milano, Milan, Italy

Abstract

This study is a first attempt to characterise the cytoarchitecture of commissural, long association and projection fibre, namely: the corpus callosum, the fornix and the corona radiata. Ovine samples from three different subjects have been stained with osmium tetroxide, embedded in resin and then imaged using scanning electron microscope combined with focused ion beam milling. Particular focus has been given to the characteristic cytological feature of the white matter: the axons. Via 2D images it has been estimated a homogeneous myelination via detection of ~40% content of lipids in all the different fibre tracts. Additionally, for each tract, a 3D reconstruction of volumes (average dimensions of 15x15x15µm) has been performed. Namely, outer axonal ellipticity, outer axonal cross sectional area and its relative perimeter have been measured. This study provides useful insight into the fibrous organisation of the tissue that can be described as composite material presenting elliptical tubular fibres with an average cross-sectional area of circa 0.52µm^2 and an estimated mean diameter of 1.15µm.

Introduction

(Brain)

Brain is a delicate, complex and still quite unknown organ. A multitude of cells constitute cerebral matter and cooperate toward its functionalities. Neurons, astrocytes, oligodendrocytes, and microglia are the main cellular bodies present in the brain (Fitzgerald, Greuner and Mtui, 2012). Overall they can be classified in neurons and non-neurons namely, glial cells. These serve as accessory cells with different supportive roles such as soft scaffolds, biochemical producers and blood-brain-barrier building blocks (von Bartheld, Bahney and Herculano-Houzel, 2016).

(GM and WM)

The biggest difference between the neurons and the glial cells is that the latter do not present myelinated portions. In fact neurons have long projections called axons that serve as a connecting network for electric signals. Because of this, an insulation for such signals is needed and myelin is the biological answer to it. This lipidic sheath is produced by oligodendrocytes (von Bartheld, Bahney and Herculano-Houzel, 2016) in the white matter (WM) of the central nervous system (CNS). The white colour is due to the high concentration of this fatty insulator and it appears as a striking visual

contrast when comparing the cortex made of grey matter (GM) and the WM. GM is rich in axonal bodies, glial cells and synaptic buttons, WM is rich in axonal protrusions, myelin and unmyelinated glia cells.

(Myelin)

As previously mentioned, myelin is a typical axonal feature made at 20% of proteins and at 80% of different lipids that give the axon its insulated characteristic. Although there are unmyelinated segments of 1-2µm in length called the Ranvier nodes, most of the axon is myelinated. These areas are called internodal sections and being their length correlated to the outer axon diameter, they range between 0.2mm and 2mm in length (Rushton, 1951). So an average volume of investigation of circa 15x15x15 µm was chosen as a compromise between optimising acquisition time and maximising the chances of characterising solely the myelinated portions of the axons. However, some unmyelinated axons coexist with their myelinated counterparts in the CNS. Their function has not been fully understood yet, and their frequency when compared to the myelinated axons it is relatively small, only the genu of the corpus callosum (CC) showing the highest percentage of unmyelinated axons (Lamantia and Rakic, 1990; Aboitiz *et al.*, 1992). Therefore, in order to minimise their contribution to this investigation, only the mid body of CC has been taken into account for this study.

(Axons)

Axons connect different areas of the CNS and therefore their length varies a lot in humans ranging from millimetres to metres (Schuez and Miller, 2002). They contain various proteins and other macromolecules, structural filaments like microtubules and mitochondria (Fadić, Vergara and Alvarez, 1985; Kubota *et al.*, 2011; Ouyang, Nauman and Shi, 2013). The conductivity speed of the axons is proportional to their diameters but wider axons are energetically more expensive and too bulky in a constrained environment such as the brain, so the presence of small axons is favoured in the cerebral tissue (Honda, Takamatsu and Wei, 1972; Perge *et al.*, 2009). As a result, most of the myelinated axons in the WM areas of the brain show diameters between 0.3µm and 2µm while the rarer bigger axons have been found mostly in the Corpus Callosum and the white matter motor pathways (Lamantia and Rakic, 1990; Aboitiz *et al.*, 1992; Ong *et al.*, 2008).

(Pathways)

Many bundles of axons connect different regions (Gray, 1918; Woolsey, Hanaway and Gado, 2003) and can be divided in:

- Commissural Pathways, such as Corpus Callosum (CC), connect the two different hemispheres
- Association Pathways, such as the long association pathway Fornix (FO), connecting regions that belong to the same hemisphere
- Projection Pathways, such as Corona Radiata (CR), connect the cortex to subcortical structures

These pathways can be seen as brain connections made of bundles of axonal fibres that link different cerebral areas. The diameter of the axons has been shown to vary depending on the linked regions as a result of the different conductivities needed per each area (Innocenti, Vercelli and Caminiti, 2014; Innocenti, Carlén and Dyrby, 2016) and additional differences between different species have been detected when comparing same pathways (Caminiti *et al.*, 2009). However the diameters and their distribution have been consistent among different studies and appear to follow gamma unimodal one-tailed distributions characterised by long right tails reaching the aforementioned upper limits of the axonal diameters (Alexander *et al.*, 2017; Jones *et al.*, 2018; Liewald *et al.*, 2014; Sepehrband *et al.*, 2016) .

(Mechanical reasoning)

Other hints of differences between zones come from biomechanically driven studies. A comprehensive study by Jin and co-workers demonstrates that the mechanical properties of the cerebral tissue are rather complex. Not only it agrees with Franceschini *et al.* on the mechanical rate-dependency qualities and the role of the axons on the mechanical properties of WM (Franceschini *et al.*, 2006). This study also highlighted the mechanical differences among different regions of the brain: CC, brain stem and CR (Jin *et al.*, 2013). Whether these differences are also caused by the geometry of the axons, is not explored being the scale of investigation not at a microscopic level. Looking at the engineering nature of the WM as an extremely soft composite material, not only the orientation but also the geometry of the fibrous component has a major role in the mechanical response and therefore needs to be addressed.

(Histological and Medical Reasoning)

Axonal geometrical data merely extrapolated from MRI and diffusion imaging studies might be misleading. In fact, research from both animal and clinical studies, has demonstrated that with the latest technologies, the minimal discernible values from MRI can range from 2.5-3.5µm (Alexander et al. 2010) to 5µm (Nilsson et al. 2010). As mentioned above, histological studies, many of which involved transmission electron microscopy (TEM), revealed a distribution of diameters of myelinated axons from the CNS peaking below the minimal discernible values from MRIs. So, when characterising the microstructure of the brain, values coming from MRI studies should be handled with care and the resolution limits always highlighted when drawing conclusions.

In addition to the 2D data from TEM studies, also scanning electron microscopy combined with focus ion beam milling (FIB-SEM) can be used to extrapolate geometrical properties from realistic 3D reconstructions of microscopic regions of interest (ROIs) (Villinger et al. 2012; Zaimi et al. 2016; Kubota 2015). Therefore, the geometries of the axons can be fully followed in their evolution over the third dimension and an accurate estimate of their geometrical properties and features would be possible. In fact, the issue of the accurate measurement being dependent on the acquisition plane position relative to the main axonal direction is avoided via 3D reconstruction.

Therefore, this research aims to provide a first tentative of producing a structural database based on investigations at a microscopic scale by subdividing the WM upon the aforementioned fascicle subdivision.

Material and Methods

(Fixing, Embedding, Staining and Sampling)

3 healthy, female *ovis aries* (1 year old, 70 Kg weight) have been used for this study. All animals were treated under the European Communities Council Directive (2010/63/EU), adhering to the laws and regulations on animal welfare enclosed in D.L.G.S. 26/2014 and approved by the Italian Health Department with authorization n° 635/2017. After culling via intravenous potassium chloride overdose following the authorization n° 635/2017 the cerebrum has been immediately removed. The three areas of interest (CC, FO, CR) have been sampled using biopsy punchers of 1mm diameter (see figure 1) from the middle coronal section of each cerebrum. Given the theory of cerebral

laterality (Miller, 1987, 1996; Liewald *et al.*, 2014), a conservative choice of sampling only from the left hemisphere has been taken to avoid any possible difference between left and right hemisphere.

We used a robust preparation protocol for high-rate imaging to obtain a satisfactory contrast for measuring of the geometrical properties of the "outer axon structure" (axon and myelin together). So, the staining and embedding method from Mikula & Dnek (Mikula and Denk, 2015) has been followed with few modifications (Feirabend, Choufoer and Ploeger, 1998) to optimise the aforementioned output. Within [time] from culling, each biopsy sample was fixed for 3 hours at room temperature in 2% formaldehyde in 0.1M sodium phosphate buffer at pH 7.4. After fixation the samples were washed 3 times for 10' in the buffer and left at circa 4°C overnight to remove any fixative remaining within the tissue.

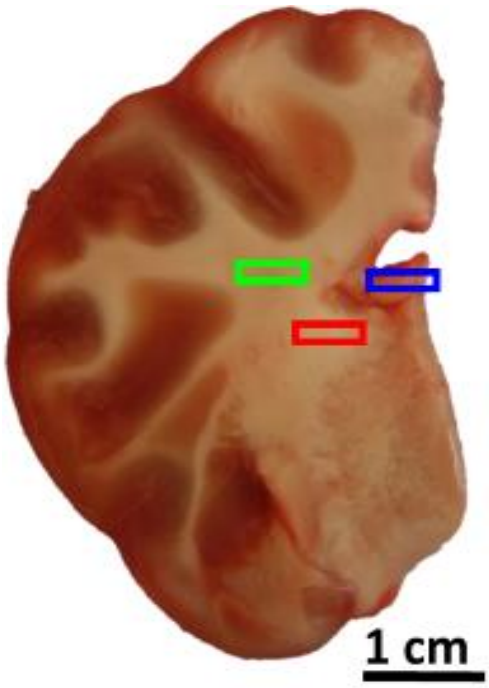

Figure 10 Sampling areas on the left hemisphere, central coronal section of the ovine brain. Red, blue and green boxes highlight the sampling areas .

In order to make visible the myelin layers around the axonal structures under SEM imaging the samples are stained in 0.5% (w/v) osmium tetroxide (OsO_4) for 1h. OsO_4 binds to the lipidic layers of the cytological components of the tissue (White *et al.*, 1976). Excessive stain is removed by washing the samples 3 times for 10' in the buffer. Samples are gradually dehydrated via immersion in ethanol-water solutions, namely at 25%, 50%, 70% and 95% ethanol-water for 15' each. Finally, samples are immersed twice, each time in fresh 100% ethanol for other 15' each time.

Embedding in LRWhite resin is done gradually in three steps. Firstly, samples are left in a 1:1 solution of ethanol and resin for 2h. Secondly, samples are immersed in another 1:3 solution of ethanol and resin. Finally, samples are left in pure LRWhite resin overnight. Anaerobic thermal curing in oven (60°C for 24h) produces the final samples ready for sectioning.

From each embedded sample three subsamples have been excised via microtoming (PTXL PowerTomes, RMC Boekler) using a glass knife. Each sample is then mounted on a stub and gold coated for the subsequent FIB SEM imaging.

(Focused Ion Beam Scanning Electron Microscope Imaging)

Imaging has been performed via a Zeiss Auriga Cross Beam featuring a Schottky field emission gun and a Gemini electron column. The SEM column is coupled with a Ga+ ion FIB.

FIB-SEM series have been taken with FIB milling conditions set to 30 kV and with a beam current of 4 nA corresponding to 150 nm thick slices. SEM imaging has been performed via a beam energy at 1.5 kV to avoid damage of the tissue sample and selective backscattered electron detector was used to image the contrast given by the heavy metal stain (Giannuzzi and Stevie, 2005). 16-bit Black and White images have been acquired via the detector and stored with a resolution of 764x1024 pixel after line averaging collection was performed in order to reduce noise.

On each subsample from each fibre tract sample, three different singular 2D areas have been imaged at random locations (see figure 2). By doing this, the homogenous composition of the sample has been investigated. Finally, for each sample corresponding to each fibre tract, a full 3D scan from one of the subsamples has been acquired per each subject with an average volume of 15x15x15µm. With a final resolution of 0.020µm per pixel, the total acquisition time resulted in ~8 hours per each 3D volume

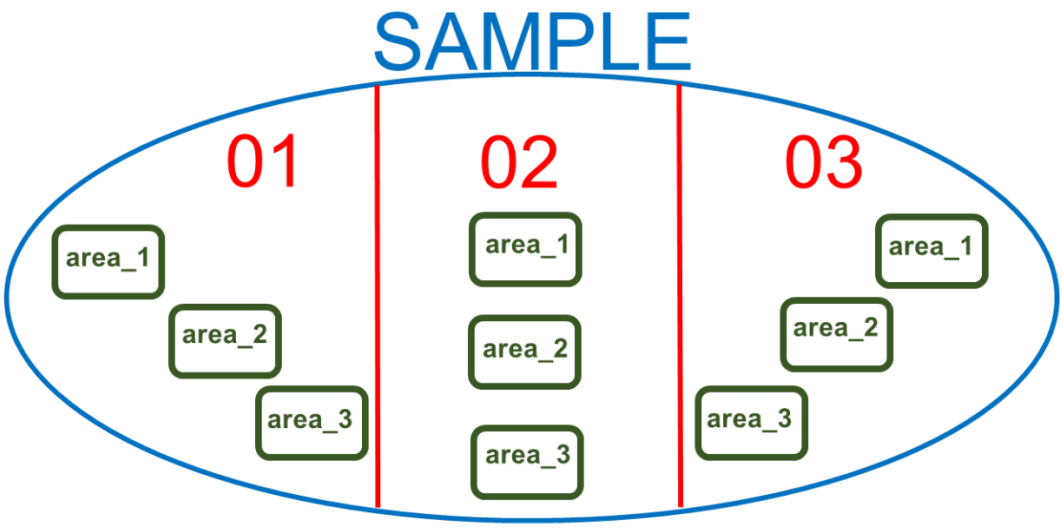

Figure 2 Scheme of the sample subdivision

(Data Analysis)

2D images: qualitative analysis of material composition

The 2D areas have been acquired at random locations and with different plane of cuts relative to the main directionality of the fibre tracts. Therefore, to assess the homogeneity of the sample, a qualitative analysis via pixel counting of the binarised images has been carried out via MATLAB scripts (The Mathworks, 2018). Firstly, the noise has been preliminary reduced in a two-step procedure.

The first step involves a reduction of the “salt and pepper” noise via a median filtering where the median values per each pixel is chosen in the 3x3 neighbourhood. At the boundaries, a symmetrical padding has been adopted. This operation reduces the scatter of the grey values around the mode and therefore reduces the amount of spurious pixels due to noise. Ideally, myelin would be imaged as "continuous rings" therefore isolated white pixels are not representative of the myelin content. The noisy pixels have so been removed via additional morphological operations (such as opening) that remove spurious and isolated pixels.

Uneven background illumination was caused by the different acquisition positions that led the areas of interest differently exposed to the beam. This type of noise would have hindered the direct

relationship between grey levels distribution and the distribution of the material in the sample. Therefore, the uneven background illumination has been reduced in the second step. Via morphological opening the objects in the foreground (the axonal matter) have been removed, the resulting unevenly illuminated background has been subtracted from the original image (see figure 3) reducing so the irregularity.

After reducing the noise, image thresholding operations have been carried out to represent the images in binary form. The MATLAB function adaptthresh has been used as some level of heterogeneously illuminated background still persists. This function is based on the algorithm developed by Bradley and Roth (Bradley and Roth, 2011). The method is based on the adaptive thresholding concept where threshold values are locally computed for each pixel. The method preserves significant contrasts and does not take into account gradient changes counterbalancing so the remaining uneven exposure of the background. After binarization, a calculation of relative frequencies for black and white pixels has been carried out in each image to estimate myelin content.

Figure 3 After filtering salt and pepper noise (1) and subtracting the unevenly illuminated background (2) the image is binarized (3).

A qualitative comparison has been carried out to determine homogeneity in composition of each sample. Firstly, bar plots of the average pixel counts computed from each area (area 1, area 2 and area 3) are compared within each of the three subsampling zones (01 02 03) to check sample homogeneity. This comparison has also been used as proof for the random choice of the 3D imaging sampling site on the sample. Then, per each sample, averages of the results from the total nine areas have been compared to detect possible composition differences between the CC, FO and CR.

(3D images: reconstruction and extrapolation of geometrical data.)

Each stack of FIB SEM images representing a 3D sample has been post-processed via Mimics software (Materialise, 2019). First a manual segmentation of each axon present in the region of interest has been carried out. Then, using the built-in 3D reconstruction algorithm of MIMICS, 3D models have been created by interpolating the different layers. Therefore, from each subject, a full 3D reconstruction of CC, FO and CR has been created.

Because of the cutting plane being not perpendicular to the centreline of the axons, post processing has been carried out to measure the real geometrical properties without distortions due to the relative position of the imaging plane. After calculating a centreline for each axon via the built-in MIMICS function, the subsequent quantities have been measured on the relative planes perpendicular to the centrelines. This allows to measure the real geometrical properties regardless of the position of the acquisition plane relative to the instances. Axonal tortuosity, area, best fit diameter and ellipticity of the cross sections have been measured along each axon, per each axon, in each 3D reconstructed sample.

Results

(2D Images)

1. *(Validation of the sample homogeneity)*

The average numbers of white pixels imaged from each subsampling area show a percentage of circa 40% of white pixels on the total pixel count in all subjects. In each sample the differences between subsampling areas (01 02 03) appear to be minimal. The average values are always within the biggest standard deviation of the three subsamples (see figure 4).

2. *(Differences in the composition between areas)*

For all subjects the relative frequency (see figure 4).

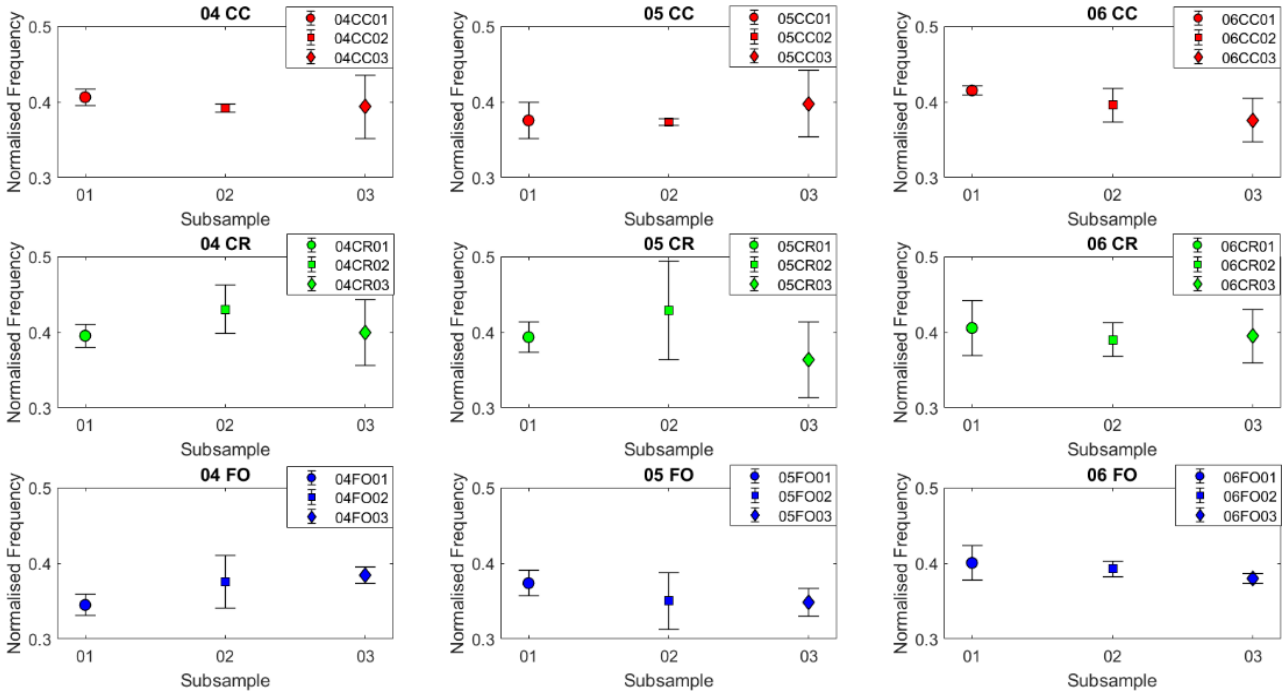

Figure 4 Barplots of the pixel counts per each subsample of each sample

(3D Images)

(Best Fit Diameter)

Average values of the geometrical properties have been calculated from all the slices representing each axon over their whole specific lengths. On all these average values from all the subjects, a lognormal distribution has been fit as suggested by Sepehrband et al. (Sepehrband *et al.*, 2016). The distribution of axonal diameter is similar between CC and CR with peaking values ranging between 1µm and 2µm. The FO shows a more spread distribution and peaking values more towards 2µm. From the fitted lognormal distributions the mode and median values of the different zones have been extrapolated and summed up in the table below (see table 1).

In this study the best fit diameters on the cross-sectional area perpendicular to the centreline of the 3D reconstructed axons have been measured. This ensures constant measurements regardless of the plane of cut relative position to the main direction of the axonal fibres. The best fit diameters of CR and CC seem to overlap in the diameter distribution being respectively 1.00 µm and 1.07µm. The FO shows still the same distributions but with values more spread around a higher mode value of circa 1.4 µm.

		CC	CR	FO
V_0		1.07 µm	1.00 µm	1.41 µm
$\tilde{x}$		1.35 µm	1.3 µm	1.81 µm

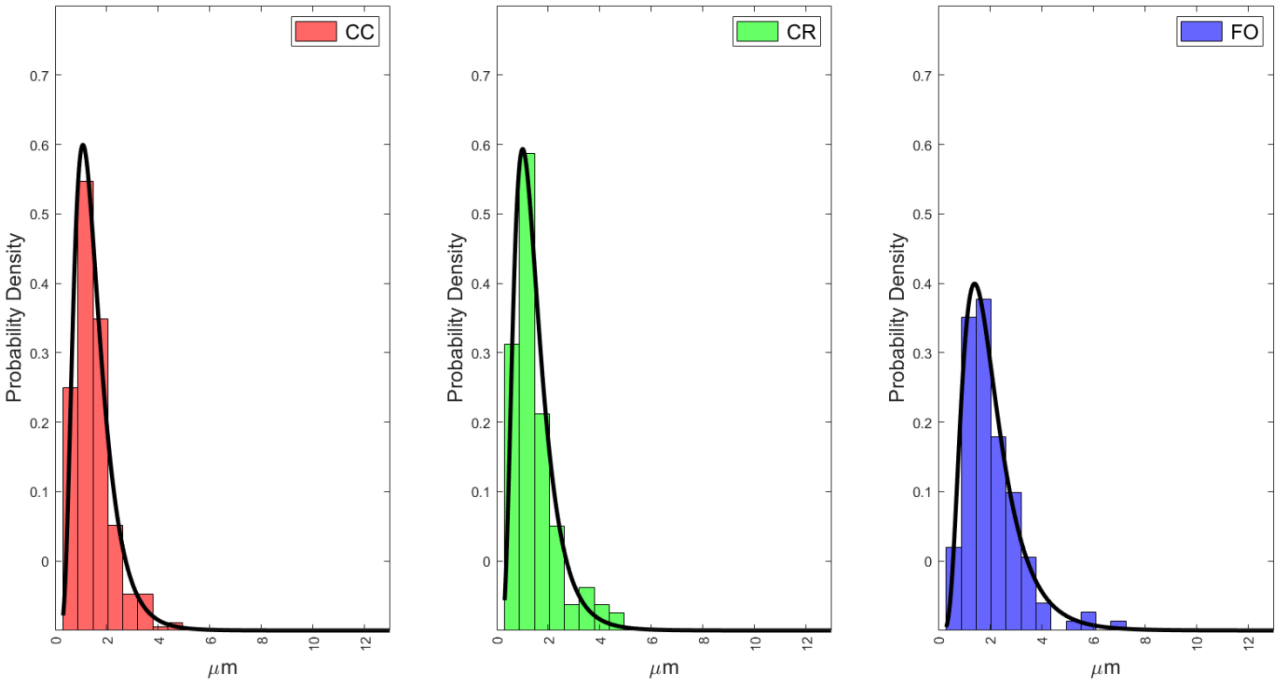

Figure 5 Axonal diameters of CC CR and FO. The data measured is lognormal distributed in all samples.

(AREA)

Cross-sectional areas show a distribution similar to the best fit diameters.. Both CC and CR similarly show a higher concentration of axons with a cross-sectional area of ~0.5µm^2 while FO appears to have a larger spread of axons with a modal area of ~1µm^2 nearly doubling the CR measurements.

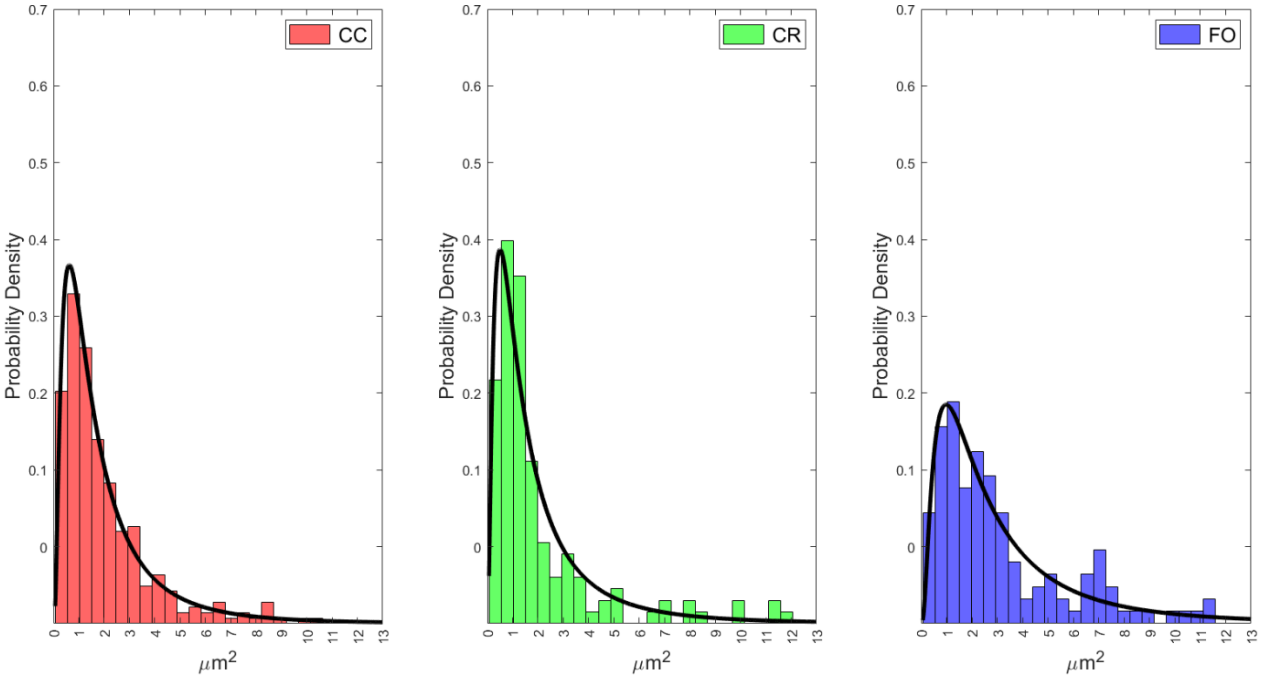

Figure 6 Axonal cross sectional area of CC CR and FO. The data measured is lognormal distributed in all samples.

	CC	*CR*	*FO*
V_0	0.63 µm^2	0.5 µm^2	0.98 µm^2
x̃	1.42 µm^2	1.35 µm^2	2.32 µm^2

(ELLIPTICITY)

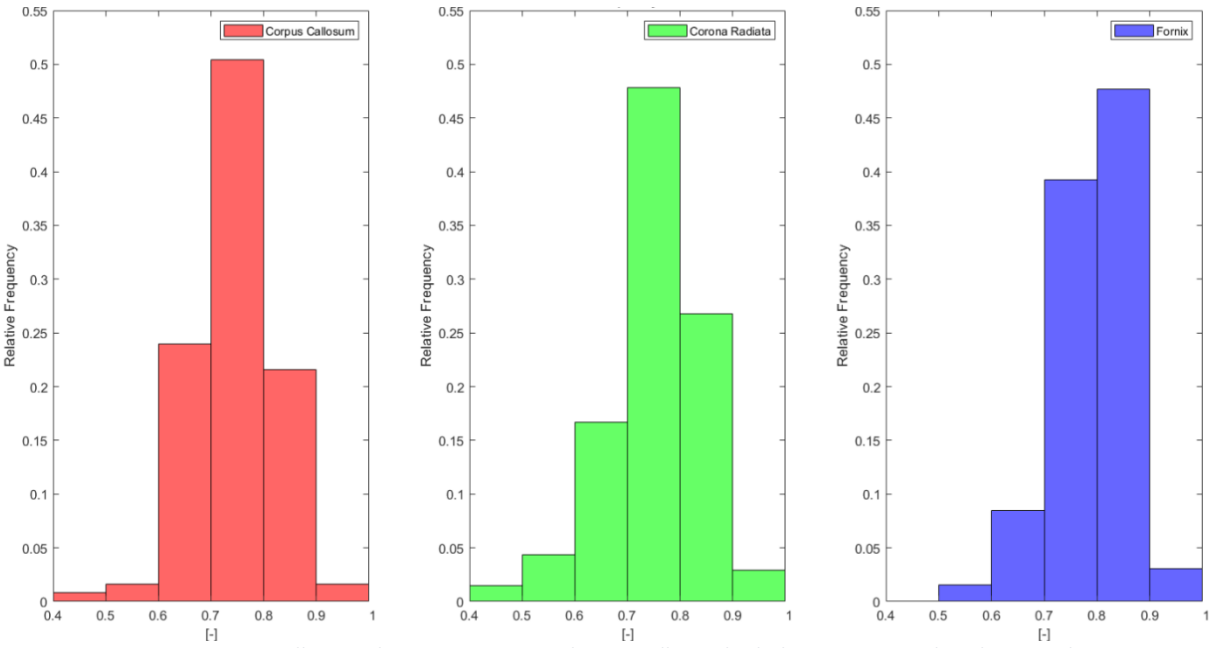

Figure 7 Ellipticity histograms. Axons show an elliptical tubular structure rather than circular

Ellipticity is calculated as $E = \sqrt{\frac{a^2-b^2}{a^2}}$ with a being the semi-major axes and b being the semi-minor axes. For $E = 1$ the semi-major axes is double the semi-minor axis, for $E = 0$ the shape is perfectly circular with the semi-major equal to the semi-minor. In the CC over 90% of measured axons show an ellipticity between 0.6 and 0.9, also the CR shows a similar trend with a slight skewness to the right. The FO displays more elliptic axons with an ellipticity towards the range 0.7-0.9.

(Tortuosity)

The tortuosity of the axons was measured via Mimics following the formula $\tau = 1 - \frac{l}{L}$ where L is the linear distance between the endpoints of the fitted centreline and l is the length of the centreline itself. The measured values give an average tortuosity for the CC of 0.113$\pm$0.109, for the CR 0.0914$\pm$0.07 and FO of 0.130$\pm$0.088.

Additionally, a comparison of the three areas is done via plotting the logarithmic values from each group against a theoretical normal distribution (see figure 9), all the groups seem to follow a lognormal distribution. While CC and CR show a similar distribution, FO differs slightly. Additionally, boxplots show the difference in the median values of the measured quantities, agreeing with the difference noticed between CC and CR against FO (see figure 8).

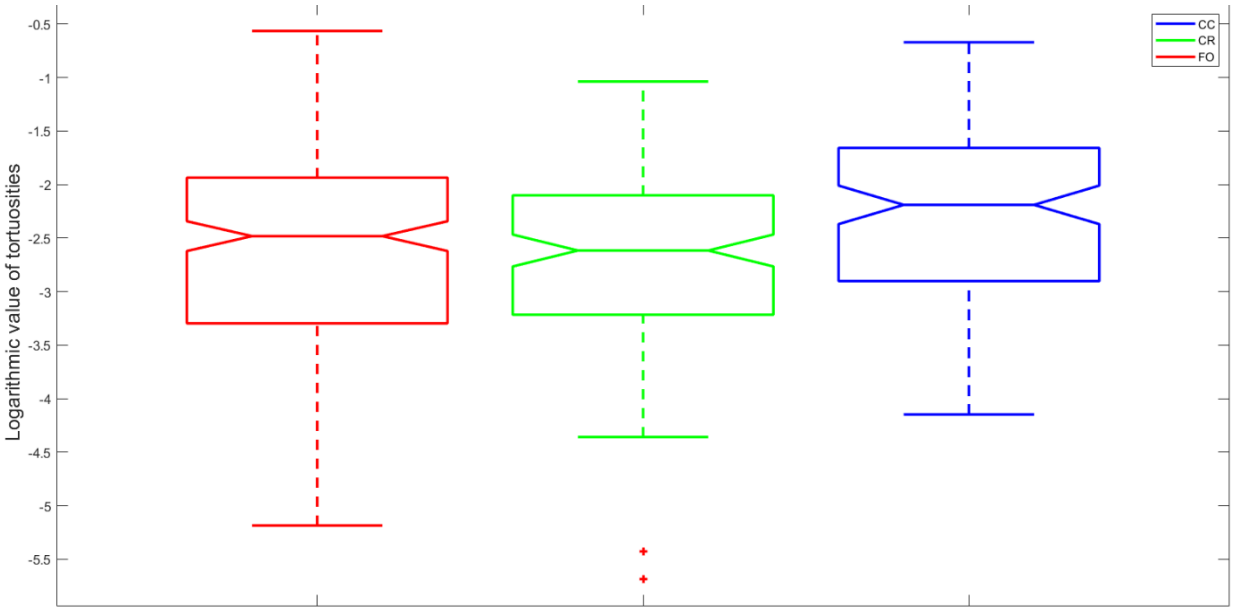

Figure 8 Boxplot of the logarithmic values of tortuosities of axons from CC, CR and FO

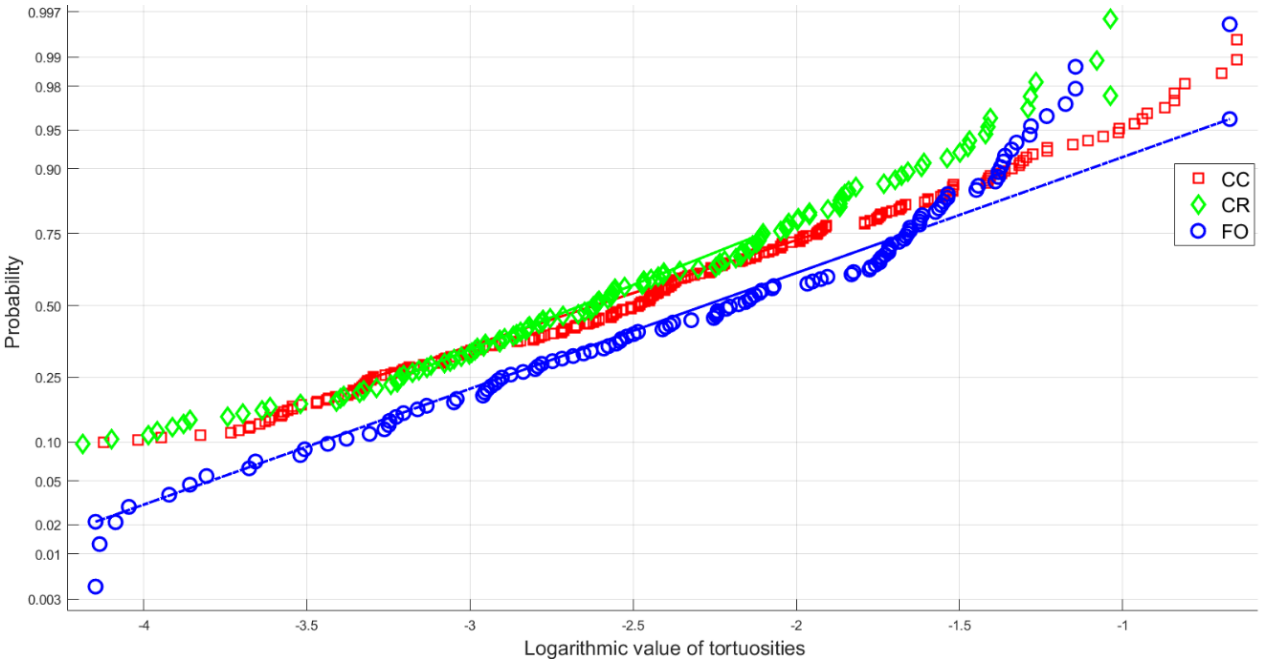

Figure 9 Normal probability plot comparing the distribution of the logarithmic values of tortuosities of axons from CC, CR and FO

(3D AREA)

As per microstructural appearance, the 3D reconstructions showed a unidirectional fibrous arrangement, with little entangling of the axonal fibres. A representative volume, manually reconstructed via MIMICS, is shown in figure 10 together with the initial FIB SEM slices.

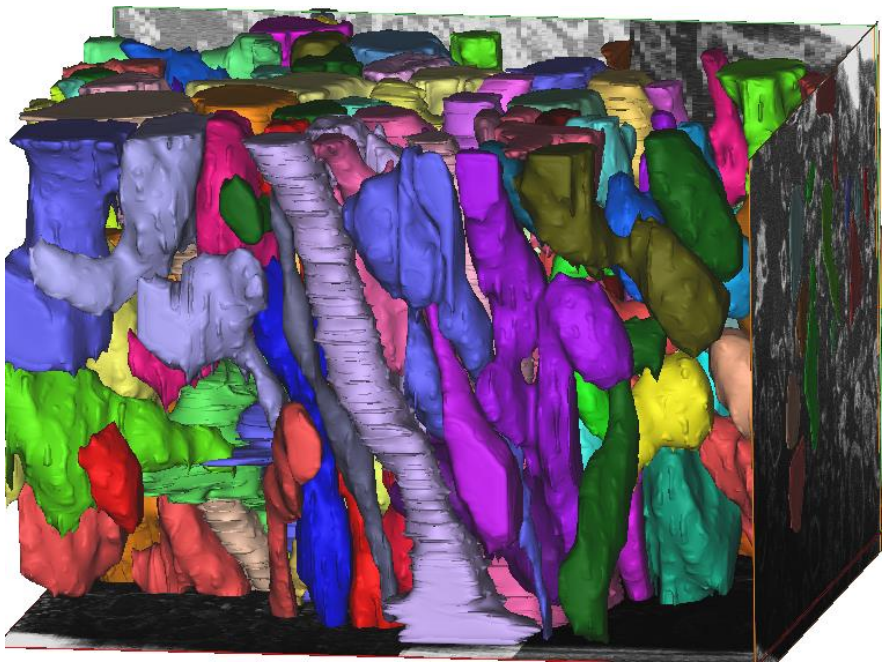

Figure 10 Manually reconstructed 3D volume of a CC.

Discussion

(*2D Images*)

1. *(Validation of the sample homogeneity and goodness of 3D location choice)*

The authors are aware that white pixels do not represent solely the myelin rings. In fact, for example, some images inevitably contained astrocytic cellular bodies. Being the astrocytes the major cells found in the glia of the CNS (Lundgaard *et al.*, 2014; Kıray *et al.*, 2016), their contribution to the pixel count could not always be avoided.

However, the normalised frequency of white pixels can still be taken as an indicative measure of the myelinisation level of the area. In fact the relative frequency of circa 40% of white pixels is in accordance to the relative lipidic content measured in dry weight of white matter samples by O'Brien and Sampson, with an approximate range between 40% and 60%. These numbers are heavily determined by the myelin sheaths. As previously mentioned, dry weight of myelin itself consists of percentages around 70%-80% of different lipids i.e. glycosphingolipids, cholesterol and other long-chain fatty acids (1 O'Brien & Sampson 1965). Another study, estimated the dry weight content of myelin from WM of adult rats to be around the same percentage of 40% (Sanjeeva Reddy, Rajalakshmi and Ramakrishnan, 1983). These converging results come from investigative techniques that differ from the EM used in this study. Therefore, this proves also the goodness of the chosen size of the ROIs that appears to be accurately representative of the material composition of WM.

Additionally, this measured homogeneity of material composition in different, randomly chosen areas across each sample, supports the goodness of the choice of random sampling locations in each samples of the areas that have undergone 3D reconstruction.

As previously mentioned, the samples all come from the CNS where the Oligodendrocytes, not the Schwann cells, contribute to the lipidic content by forming the myelin rings typical of the WM (Duncan and Hoffman, 1997; Salzer, 2015; Kıray *et al.*, 2016). So, the consistency found among all samples could be explained by the uniformity of the cells involved in the myelination of the axons. Additionally, all the sampled fibre tracts belong to the CNS, here the axons are shorter than the ones in the Peripheral Nervous System (PNS) so a uniform level of myelination would be expected

(Fitzgerald, Greuner and Mtui, 2012). Another difference between myelination in the Peripheral Nervous System (PNS) and the CNS is that in the former whole cells entirely wrap around the axons (the Schwann Cells), while in the latter myelination is achieved via wrapped membrane processes of the aforementioned Oligodendrocytes. Their projections of the cellular membrane wraps around several axonal fibres forming myelin sheaths (Moore, Dalley and Agur, 2013; Simons and Nave, 2016). EM images show myelin sheaths as periodically layered areas of electron dense and light dense regions that represent the alternation of intraperiod and dense lines (see red dashed box in figure 10). This feature is where the oligodendrocitic membrane comes into apposition to form the isolating layer (Peters, 1960) . Therefore, the recognition of this feature aides in the correct individuation of myelin rings also in the eventuality of split, degenerated layers.

2. (Goodness of the experimental choices and split myelin)

To minimise trauma to the tissue, a slow and gradual dehydration has been followed as aforesaid. A standard aldehyde-based dehydration method provides a good compromise between practical simplicity and the goodness of the acquired results (Kubota, 2015, Liewald et al. 2014

FIB-SEM is well suited for an automated and high output rate imaging, especially when the high resolution is not required as the smallest resolvable feature are axonal tubular structures with a diameter of 0.2-0.4 µm (Bosch et al., 2015). Therefore, as this study focusses on the 3D cyto-organization of the axonal fibres for modelling purposes, priority to the output quantity has been given at a cost of a lower resolution of the axonal ultrastructure comprising the extra cellular matrix. As a matter of fact, an engineering approach has guided this study throughout where the imaging of the feature of interest responds to a need of measuring the geometrical properties of these fibrous components (the axons) that heavily influence the mechanical characteristics of WM as a composite material (Arbogast and Margulies, 1999; Abolfathi *et al.*, 2009; Karami *et al.*, 2009).

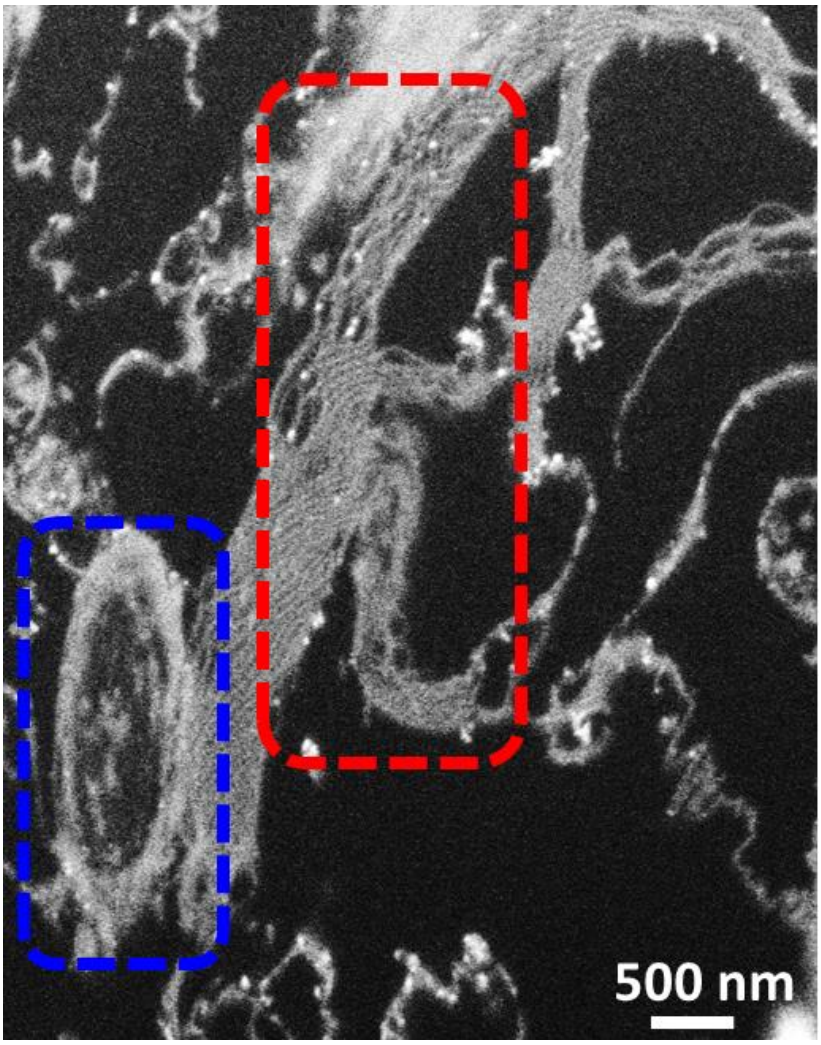

Figure 10 Zoom of a 2D image where a compact myelin sheath (blue dashed box) and a split sheath (red dashed box) are visible. In the split sheath intraperiod and dense lines are visible.

(3D Images)

As previously mentioned, this study aims to create an initial database on the geometrical characteristics of the fibres from specific areas of the WM for micromechanical and CFD purposes. In fact, it has been shown that the WM stiffness is highly related to the axonal presence. Axonal cytoskeletal elements such as microtubules contribute greatly to the axon mechanical response (Ouyang, Nauman and Shi, 2013) and to its relative contribution to the overall tissue stiffness. Also, it has been proved that the content of the myelin wrapping the axons linearly increased the stiffness of the WM tissue (Weickenmeier *et al.*, 2016). Additionally, like in many MRI and diffusivity studies, it has been assumed that axons are impermeable due to their envelope of myelin composed of hydrophobic lipid (Cory and Garroway, 1990; Callaghan *et al.*, 1991; Barazany, Basser and Assaf, 2009; Ong and Wehrli, 2010; Dyrby *et al.*, 2013; Alexander *et al.*, 2017). Also Convection Enhanced Delivery studies and clinical studies on the cerebral oedema propagation seem to give substantial

hints on the influence of the axonal fibres on fluid diffusion (Reulen *et al.*, 1977; Geer and Grossman, 1997; Stummer, 2007). Therefore, the recognition of the axonal features has comprised the outer ring of myelin sheaths, so all the data expressed in this research are representative of axons and their relative myelin rings: the "outer diameter" of the axon.

The distributions of the measured data are in agreement with findings of previous studies that involved ultra-strong gradients for diffusion MRI and different electron microscopy techniques. For example, values of the CC diameter are within the range of the existing literature where more than 50% of the measurements are confined between 0.5µm and 1.5µm. (A.Lamantia and Rakic, 1990; Assaf *et al.*, 2008; Liewald *et al.*, 2014; Jones *et al.*, 2018; Nunes *et al.*, 2017). Interestingly, the values measured on ovine brain are more similar to the ones measured on chimpanzees and humans than to the measurements performed on macaques. In fact, although the range of values and the lognormal distribution of data is maintained, the spread of the ovine values is more similar to the former two species than the latter, which presents a higher concentration of smaller axons in the CC. This validates how sheep can be successfully used as an animal model and could replace other species given its similarity to human cerebral cytostructure (Caminiti *et al.*, 2009).

CR consistently showed geometrical data trend very similar to the CC; this similarity between these two areas was also maintained in the measured axonal density, with the FO showing a less dense axonal population when compared to CR and CC. Irregularities and degeneration of the myelin layers have been found slightly more often in FO samples. These degenerative patterns have been widely detected in several studies across different species and although its consequences on the brain functionality have not yet been fully understood, it has been related to the normal aging processes occurring in all living organisms (Bowley *et al.*, 2010; Peters, Sethares and Moss, 2010).

The variation of the diameter and the cross-sectional area measured within the same axonal structures is due to the different subcellular structures within the axon, of which the most prominent is the mitochondria that appeared as bulges along the axonal tube (Abdollahzadeh *et al.*, 2019). These features contributed to the ellipticity findings in all of the three areas, that unequivocally show that axons should be thought as ellipsoidal, rather than circular, tubular structures with ellipticity values comprised between 0.7 and 0.9.

This study also gives a first quantifiable measure of the level of tortuosity of the fibrous component of the WM. Interestingly, also this geometrical quantity follows a lognormal distribution. Low values of tortuosity have been detected in all of the three fibre tracts showing that, at the microscale, axons follow a nearly straight path in the CNS. Also for this geometrical entity, a difference between the FO and the CC-CR duo has been detected with FO showing slightly more tortuous axons. It is important to highlight that previous studies always took into considerations WM samples from cranial nerves or from spinal cord where a much wavier layout of the axonal tracts is visible (INSERT REF).

All of these findings suggest that while commissural and projection fibres have a more similar cytoarchitecture, the long projection fibre of FO seem to slightly differ, probably due to its particular anatomical configuration. Given its fornix shape, the more accentuated bending and curving of the macroscopic fibre bundle might be the reason of the measured difference.

Another focal point of this study is to create a usable database aimed at fluid dynamics and micromechanical modelling based on the geometrical properties measured from the 3D reconstructions. However, irregularities and artefacts arising from the manual segmentation process would have hindered a usable, standardised 3D file object aimed at FEA studies. Therefore, the axonal data discussed above have been post-processed in order to create potential representative volume elements (RVE) for micromechanical analysis ready to be used as inputs for FEA packages and for other studies.

A semi-automated reconstruction of the axonal architecture has been performed via a custom made code in Matlab. Because of the representativeness of the content measured, RVEs of 15x15x15µm have been chosen and assembled following a periodicity constraint on the plane perpendicular to the direction of the fibres. The sampling of the image acquisition during FIB-SEM imaging has been maintained with a total of 100 slices with a thickness of 0.15µm each.
In every volume, the geometrical inputs come from a random subsampling of the distributions of data distributions mentioned before: cross-sectional area, diameter, ellipticity, tortuosity and axonal density. Additionally, the measured variations of cross-sectional area, diameter and ellipticity along the fibre direction have been followed. In red the outcome for the CC, in green the CR and in blue the FO.

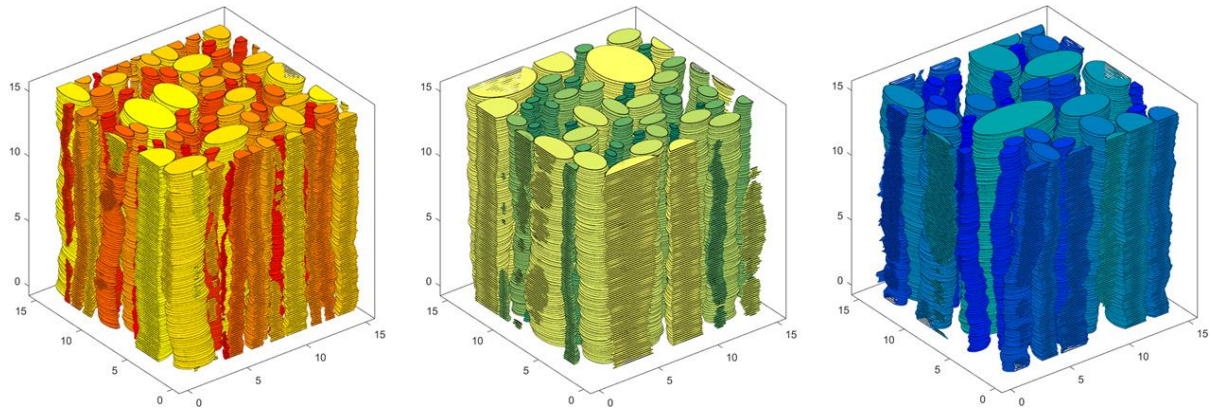

Figure 11 Representative periodic volumes of the CC (shades of red), CR (shades of green) and FO (shades of blue) generated via a Matlab custom-built code.

(Future Work and Conclusions)

Cryo-imaging techniques have been shown to differently preserve the ultrastructure of the biological matter when compared to the alcohol-driven dehydration that characterizes the methodology followed in this study (Simons and Nave, 2016). In fact, the authors realise that the techniques applied in this research have affected the sampled tissue by some shrinkage factor (Virtanen *et al.*, 1984). However, room temperature fixation technique herein adopted provides a robust and relatively easy solution for a high rate imaging output of multiple specimens. In fact, the aforementioned agreements between our data and data from other studies show that any adverse effect to the structure is negligible for the main purpose of this study.

Additional refinement by adding MRI images of the sampled brains as reference images could lead to extra information on the sampling position relative to the axonal tracts of each individual cerebrum (Catani et al. 2012a). In fact, the authors realise that manual sampling from visual recognition of the areas of interest does not provide exact sampling coordinates of the specimena relative to each brain.

Finally, this study is a first important attempt of geometrical micro characterization of the different pathways in which WM tracts are anatomically subdivided. We show the feasibility of this methodology aimed at creating an axonal geometry database for each of the tracts of the cerebral tissue. We also show how commissural and projection fibres seem to be more similar to each other

when compared to long association fibres. Ultimately, such a detailed knowledge of the microstructure can provide a key insight for a deeper understanding of the different cerebral macro phenomena. Diffusivity, permeability and mechanical behaviour of cerebral tissue are all intrinsically dependent on the cytoarchitecture of the WM and can only be better understood with a detailed knowledge of this. All of these fundamental properties can also be further studied via in silico experiments and simulations that can now be based on models that are geometrically representative of real life tissue.

REFERENCES

Abdollahzadeh, A. *et al.* (2019) 'Automated 3D Axonal Morphometry of White Matter', *Scientific Reports*, 9(1), pp. 1–16. doi: 10.1038/s41598-019-42648-2.

Aboitiz, F. *et al.* (1992) 'Fiber composition of the human corpus callosum', *Brain Research*, 598, pp. 143–153.

Abolfathi, N. *et al.* (2009) 'A micromechanical procedure for modelling the anisotropic mechanical properties of brain white matter', *Computer Methods in Biomechanics and Biomedical Engineering*, 12(3), pp. 249–262. doi: 10.1080/10255840802430587.

Alexander, D. C. *et al.* (2017) 'Imaging brain microstructure with diffusion MRI: Practicality and applications', *NMR in Biomedicine*, (November 2016), pp. 1–26. doi: 10.1002/nbm.3841.

Arbogast, K. B. and Margulies, S. S. (1999) 'A fiber-reinforced composite model of the viscoelastic behavior of the brainstem in shear', *Journal of Biomechanics*, 32(8), pp. 865–870. doi: 10.1016/S0021-9290(99)00042-1.

Assaf, Y. *et al.* (2008) 'AxCaliber: A method for measuring axon diameter distribution from diffusion MRI', *Magnetic Resonance in Medicine*, 59(6), pp. 1347–1354. doi: 10.1002/mrm.21577.

Barazany, D., Basser, P. J. and Assaf, Y. (2009) 'In vivo measurement of axon diameter distribution in the corpus callosum of rat brain', *Brain*, 132(5), pp. 1210–1220. doi: 10.1093/brain/awp042.

von Bartheld, C. S., Bahney, J. and Herculano-Houzel, S. (2016) 'The search for true numbers of neurons and glial cells in the human brain: A review of 150 years of cell counting', *Journal of Comparative Neurology*, 524(18), pp. 3865–3895. doi: 10.1002/cne.24040.

Bowley, M. P. *et al.* (2010) 'Age changes in myelinated nerve fibers of the cingulate bundle and corpus callosum in the rhesus monkey', *The Journal of Comparative Neurology*, 518(15), pp. 3046–3064. doi: 10.1002/cne.22379.

Bradley, D. and Roth, G. (2011) 'Adaptive Thresholding using the Integral Image', *Journal of Graphics Tools*, 12(2), pp. 13–21. doi: 10.1080/2151237x.2007.10129236.

Callaghan, P. T. *et al.* (1991) 'Diffraction-like effects in NMR diffusion studies of fluids in porous solids', *Nature*, 351(6326), pp. 467–469. doi: 10.1038/351467a0.

Caminiti, R. *et al.* (2009) 'Evolution amplified processing with temporally dispersed slow neuronal connectivity in primates', *Proceedings of the National Academy of Sciences*, 106(46), pp. 19551–19556. doi: 10.1073/pnas.0907655106.

Cory, D. G. and Garroway, A. N. (1990) 'Measurement of Translational Displacement Probabilities by NMR_MRM1990.pdf', 444, pp. 435–444.

Duncan, I. D. and Hoffman, R. L. (1997) 'Schwann cell invasion of the central nervous system of the myelin mutants', *Journal of Anatomy*, 190(1), pp. 35–49. doi: 10.1017/S0021878296001483.

Dyrby, T. B. *et al.* (2013) 'Contrast and stability of the axon diameter index from microstructure imaging with diffusion MRI', *Magnetic Resonance in Medicine*, 70(3), pp. 711–721. doi: 10.1002/mrm.24501.

Fadić, R., Vergara, J. and Alvarez, J. (1985) 'Microtubules and caliber of central and peripheral processes of sensory axons', *The Journal of Comparative Neurology*, 236(2), pp. 258–264. doi: 10.1002/cne.902360209.

Feirabend, H. K. P., Choufoer, H. and Ploeger, S. (1998) 'Preservation and Staining of Myelinated Nerve Fibers', *Methods*, 15(2), pp. 123–131. doi: 10.1006/meth.1998.0615.

Fitzgerald, M., Greuner, G. and Mtui, E. (2012) *Clinical Antomy and Neuroscience*. 6th edn. Edited

by M. Hyde and J. Scott. Elsevier.

Franceschini, G. *et al.* (2006) 'Brain tissue deforms similarly to filled elastomers and follows consolidation theory', *Journal of the Mechanics and Physics of Solids*, 54(12), pp. 2592–2620. doi: 10.1016/j.jmps.2006.05.004.

Geer, C. P. and Grossman, S. A. (1997) 'Interstitial fluid flow along white matter tracts: A potentially important mechanism for the dissemination of primary brain tumors', *Journal of Neuro-Oncology*, 32(3), pp. 193–201. doi: 10.1023/A:1005761031077.

Giannuzzi, L. A. and Stevie, F. A. (2005) *Introduction to focused ion beams : instrumentation, theory, techniques, and practice*, *Introduction to Focused Ion Beams*. Boston, MA: Springer US.

Gray, H. (1918) *Anatomy of the Human Body*. 20th edn. Philadelphia: Lea & Febiger.

Honda, H., Takamatsu, H. and Wei, J. J. (1972) 'Relative Conduction Velocities of Small Myelinated and Non-myelinated Fibres in the Central Nervous System', *Nihon Kikai Gakkai Ronbunshu, B Hen/Transactions of the Japan Society of Mechanical Engineers, Part B*, 68(672), pp. 2327–2332.

Innocenti, G. M., Carlén, M. and Dyrby, T. B. (2016) 'The Diameters of Cortical Axons and Their Relevance to Neural Computing', in *Axons and Brain Architecture*. Elsevier, pp. 317–335. doi: 10.1016/B978-0-12-801393-9.00015-3.

Innocenti, G. M., Vercelli, A. and Caminiti, R. (2014) 'The diameter of cortical axons depends both on the area of origin and target', *Cerebral Cortex*, 24(8), pp. 2178–2188. doi: 10.1093/cercor/bht070.

Jin, X. *et al.* (2013) 'A comprehensive experimental study on material properties of human brain tissue', *Journal of Biomechanics*. Elsevier, 46(16), pp. 2795–2801. doi: 10.1016/j.jbiomech.2013.09.001.

Jones, D. K. *et al.* (2018) 'Microstructural imaging of the human brain with a "super-scanner": 10 key advantages of ultra-strong gradients for diffusion MRI', *NeuroImage*. Elsevier Ltd, 182(December 2017), pp. 8–38. doi: 10.1016/j.neuroimage.2018.05.047.

Karami, G. *et al.* (2009) 'A micromechanical hyperelastic modeling of brain white matter under large deformation', *Journal of the Mechanical Behavior of Biomedical Materials*. Elsevier Ltd, 2(3), pp. 243–254. doi: 10.1016/j.jmbbm.2008.08.003.

Kıray, H. *et al.* (2016) 'The multifaceted role of astrocytes in regulating myelination', *Experimental Neurology*, 283, pp. 541–549. doi: 10.1016/j.expneurol.2016.03.009.

Kubota, Y. *et al.* (2011) 'Conserved properties of dendritic trees in four cortical interneuron subtypes.', *Scientific reports*, 1, p. 89. doi: 10.1038/srep00089.

Lamantia, A.-S. and Rakic, P. (1990) 'Cytological and quantitative characteristics of four cerebral commissures in the rhesus monkey', *The Journal of Comparative Neurology*, 291(4), pp. 520–537. doi: 10.1002/cne.902910404.

Liewald, D. *et al.* (2014) 'Distribution of axon diameters in cortical white matter: an electron-microscopic study on three human brains and a macaque', *Biological Cybernetics*, 108(5), pp. 541–557. doi: 10.1007/s00422-014-0626-2.

Lundgaard, I. *et al.* (2014) 'White matter astrocytes in health and disease', *Neuroscience*, 276, pp. 161–173. doi: 10.1016/j.neuroscience.2013.10.050.

Materialise (2019) 'Materialise Mimics 16.0'. Leuven, Belgium.

Mikula, S. and Denk, W. (2015) 'High-resolution whole-brain staining for electron microscopic circuit reconstruction', *Nature Methods*, 12(6), pp. 541–546. doi: 10.1038/nmeth.3361.

Miller, R. (1987) ‘Representation of brief temporal patterns, Hebbian synapses, and the left-hemisphere dominance for phoneme recognition’, *Psychobiology*, 15(3), pp. 241–247. doi: 10.3758/BF03327275.

Miller, R. (1996) *Axonal conduction time and human cerebral laterality. A psychobiological theory.* Australia: Harwood Academic Publishers.

Moore, K. L., Dalley, A. F. and Agur, A. M. R. (2013) *Clinically Oriented Anatomy 7th revise*. Lippincot and Williams and Wilkins.

Nunes, D. *et al.* (2017) ‘Mapping axonal density and average diameter using non-monotonic time-dependent gradient-echo MRI’, *Journal of Magnetic Resonance*. Elsevier Inc., 277, pp. 117–130. doi: 10.1016/j.jmr.2017.02.017.

Ong, H. H. *et al.* (2008) ‘Indirect measurement of regional axon diameter in excised mouse spinal cord with q-space imaging: Simulation and experimental studies’, *NeuroImage*, 40(4), pp. 1619–1632. doi: 10.1016/j.neuroimage.2008.01.017.

Ong, H. H. and Wehrli, F. W. (2010) ‘Quantifying axon diameter and intra-cellular volume fraction in excised mouse spinal cord with q-space imaging’, *NeuroImage*. Elsevier Inc., 51(4), pp. 1360–1366. doi: 10.1016/j.neuroimage.2010.03.063.

Ouyang, H., Nauman, E. and Shi, R. (2013) ‘Contribution of cytoskeletal elements to the axonal mechanical properties’, *Journal of Biological Engineering*. Journal of Biological Engineering, 7(1), p. 21. doi: 10.1186/1754-1611-7-21.

Perge, J. A. *et al.* (2009) ‘How the Optic Nerve Allocates Space, Energy Capacity, and Information’, *Journal of Neuroscience*, 29(24), pp. 7917–7928. doi: 10.1523/jneurosci.5200-08.2009.

Peters, A. (1960) ‘The Structure of Myelin Sheaths in the Central Nervous System of Xenopus laevis (Daudin)’, *The Journal of Cell Biology*, 7(1), pp. 121–126. doi: 10.1083/jcb.7.1.121.

Peters, A., Sethares, C. and Moss, M. B. (2010) ‘How the primate fornix is affected by age’, *The Journal of Comparative Neurology*, 518(19), pp. 3962–3980. doi: 10.1002/cne.22434.

Reulen, H. J. *et al.* (1977) ‘Role of pressure gradients and bulk flow in dynamics of vasogenic brain edema.’, *Journal of neurosurgery*, 46(1), pp. 24–35. doi: 10.3171/jns.1977.46.1.0024.

Rushton, W. A. H. (1951) ‘A theory of the effects of fibre size in medullated nerve’, *The Journal of Physiology*, 115(1), pp. 101–122. doi: 10.1113/jphysiol.1951.sp004655.

Salzer, J. L. (2015) ‘Schwann cell myelination’, *Cold Spring Harbor Perspectives in Biology*, 7(8), pp. 1–26. doi: 10.1101/cshperspect.a020529.

Sanjeeva Reddy, T., Rajalakshmi, R. and Ramakrishnan, C. V. (1983) ‘Lipid composition of gray and white matter in developing rat brain’, *International Journal of Developmental Neuroscience*, 1(1), pp. 65–74. doi: 10.1016/0736-5748(83)90012-6.

Schuez, A. and Miller, R. (2002) *Cortical Areas Unity and Diversity*, *On Humanism*. Edited by A. Schüz and R. Miller. LONDON: Taylor & Francis. Available at: https://www.taylorfrancis.com/books/9780203219911.

Sepehrband, F. *et al.* (2016) ‘Parametric Probability Distribution Functions for Axon Diameters of Corpus Callosum’, *Frontiers in Neuroanatomy*, 10(May), pp. 1–9. doi: 10.3389/fnana.2016.00059.

Simons, M. and Nave, K. A. (2016) ‘Oligodendrocytes: Myelination and axonal support’, *Cold Spring Harbor Perspectives in Biology*, 8(1), pp. 1–15. doi: 10.1101/cshperspect.a020479.

Stummer, W. (2007) ‘Mechanisms of tumor-related brain edema.’, *Neurosurgical focus*, 22(5), p. E8. doi: 10.3171/foc.2007.22.5.9.

The Mathworks, I. (2018) ‘MATLAB and Statistics Toolbox Release 2018b’. Natick, Massachusetts.

Virtanen, J. *et al.* (1984) ‘the Effect of Fixation on and Morphology in Scanning Electron Microscopy’, *Acta Ophtalmologica*, 62, pp. 577–585.

Weickenmeier, J. *et al.* (2016) ‘Brain stiffness increases with myelin content’, *Acta Biomaterialia*. Acta Materialia Inc., 42, pp. 265–272. doi: 10.1016/j.actbio.2016.07.040.

White, D. L. *et al.* (1976) ‘The chemical nature of osmium tetroxide fixation and staining of membranes by X-ray photoelectron spectroscopy’, *Biochimica et Biophysica Acta (BBA) - Biomembranes*, 436(3), pp. 577–592. doi: 10.1016/0005-2736(76)90442-9.

Woolsey, T. A., Hanaway, J. and Gado, M. H. (2003) *The Brain Atlas*. 3rd edn, *Book*. 3rd edn. Hoboken, New Jersey: A John Wiley & Sons, Inc.

Discussion

This doctorate thesis dealt with different aspects and topics in the field of EDEN2020 project. Enhanced Delivery Ecosystem for Neurosurgery in 2020 (EDEN2020) is a European project supported by the European Union's EU Research and Innovation programme Horizon 2020 under grant agreement n° 688279.

The main aim of EDEN2020 is to provide a step change in the treatment of brain disease by delivering an integrated technology platform for minimally invasive neurosurgery.

EDEN2020 is built around two parallel research threads, the first focused on a clinical investigation of diffusion, encompassing experiments and computational modelling, and the other on technological development of a steerable catheter and catheter controller, intelligent planner, real-time intra-operative visualisation and tracking, and in vivo diagnostics via flexible access.

Clinical research activities workflow has been validated in a staged approach throughout the project three sequential animal trials: ex vivo experiments to fine tune system performance and procedural work flow; in vivo ovine trials to ascertain feasibility of the system under realistic operating conditions; in vivo study to evaluate and verify system performance in a clinical setting.

The right animal model choice has been the first procedural step of my PhD. The project needed a translational model, characterized by similar brain and skull features compared to human anatomy respecting the 3R rules (reduce, refine, replace). Large animal models have been contemplated as better models than small one as mouse, rat, rabbit, even though small-animal models are usually favourited due to low cost, ease of care, and the possibilities for high work rate. Moreover murine and rabbit model are characterized by a lissencephalic brain cortex which is a major limit for EDEN2020.

A brief analysis on large animal models, composed by ovine and swine animals, have been conducted focusing animal behaviour, growth index and most important, skull anatomy and features. Ovine model has been selected as proper model for EDEN2020 project.

The present doctorate thesis contains three researches in different topic all under the EDEN2020 project scenario.

The first study reported a work concerning the validation of a novel stereotactic head frame MRI compatible for ovine models. Since no stereotactic head frame tools for ovine model MRI

compatible were available and the surgical workflow in EDEN2020 needed the MRI and CT study for neuroplanning purpose, an *ad hoc* ovine head frame system has been developed and validated to achieve this objective. The validation protocol has been composed by the sheep head fixation analysis and MRI compatibility test. The results in *ex vivo* and *in vivo* tests reported an average linear motion for the ex-vivo trials was 0.81 ± 0.54 mm., while for the in-vivo trials was 0.68 ± 0.61 mm. The MRI compatibility test was evaluated in an MRI scanner and data analysis was carried out following the National Electrical Manufacturers Association (NEMA) procedures standard assuming a statistically and spatially uniform distribution of noise. The head frame system for the ovine model presented, address several clinical requirements of translational studies, such as CT/MRI compatibility, compatibility with a conventional human stereotactic CRW frame, robustness during the surgical procedure and robustness against the anatomical variability which is inherent in the sheep model. The system described may benefit future research projects using sheep as an animal model.

The objective of the second work illustrated in this thesis was to determine the major ovine white matter fibre bundles via diffusion tensor resonance tractography. Diffusion Tensor Magnetic Resonance Imaging (DTI) allows to decode the mobility of water molecules in cerebral tissue, which is highly directional along myelinated fibres. By integrating the direction of highest water diffusion through the tissue, DTI Tractography enables a non-invasive dissection of brain fibre bundles. As such, this technique is a unique probe for in vivo characterization of white matter architecture. Unravelling the principal brain texture features of preclinical models that are advantageously exploited in experimental neuroscience is crucial to correctly evaluate investigational findings and to correlate them with real clinical scenarios. Firstly the *in vivo* brain MRI protocol for ovine animal models was optimized on a 1.5T scanner. Topography of the ovine cortex was then studied and DTI maps were derived to perform DTI tractography reconstruction of the corticospinal tract (CST), corpus callosum (CC), fornix (FX), visual pathway (VP) and occipitofrontal fascicle (OF), bilaterally for all the animals involved in the study with a minimal inter-subject variability. The present work built an innovative ovine tractography atlas, demonstrating that multiple white matter fibre tracts can be consistently reconstructed in sheep. Additionally, the population-averaged atlas can be integrated into publicly available imaging software, paving the way toward space standardization of ovine imaging analyses. It will enable to design homogeneous studies considering the direction and reciprocal position of white matter fibre bundles, that will significantly support the meticulous study of numerous brain pathologies. In conclusion, the ovine

tractography atlas can be considered as a valuable tool to implement the knowledge of sheep's brain anatomy and to improve the activity of clinicians and researchers using this animal model in neuroscience studies

The third work involved the microscopic analysis cytoarchitecture of commissural, long association and projection fibre, specifically the corpus callosum, the fornix and the corona radiata. The fibre tract analysed have been selected from the bundles reconstructed via DTI analysis. Corpus callosum and Fornix have been studied properly while corticospinal tract has been sampled via corona radiata. Ovine samples from three different subjects have been stained with osmium tetroxide, embedded in resin and then imaged using scanning electron microscope combined with focused ion beam milling. Particular focus has been given to the characteristic cytological feature of the white matter: the axons. Via 2D images it has been estimated a homogeneous myelination via detection of ~40% content of lipids in all the different fibre tracts. Additionally, for each tract, a 3D reconstruction of volumes (average dimensions of 15x15x15µm) has been performed. Namely, outer axonal ellipticity, outer axonal cross sectional area and its relative perimeter have been measured. The study provided useful insight into the fibrous organisation of the tissue that can be described as composite material presenting elliptical tubular fibres with an average cross-sectional area of circa 0.52µm2 and an estimated mean diameter of 1.15µm. This study is a first important attempt of geometrical micro characterization of the different pathways in which WM tracts are anatomically subdivided. The data acquired from the microstructure can provide a key insight for a deeper understanding of the different cerebral macro phenomena indeed diffusivity, permeability and mechanical behaviour of cerebral tissue are all intrinsically dependent on the cytoarchitecture of the WM. All of these fundamental properties can also be further studied via in silico experiments and simulations that can now be based on models that are geometrically representative of real life tissue.

Appendix

EDEN2020: Encephalic tissue damage evaluation after catheter insertion in sheep brain model

Introduction

As this project is still ongoing, the last period of the PhD has been focused on the analysis of the brain tissue damage after catheter introduction. The first part of the project has been concentrated in the use of a rigid catheter simulating a common clinical scenario. The results of the damage from the rigid catheter will be compared with the steerable catheter developed in EDEN2020.

Given the nature of this project which will see the natural end on March 2020, analysis and data are currently in acquisition. Here below is presented a brief overview about the rational on which the catheter tissue damage analysis is based.

Sheep has been involved in several studies with different aims. Unfortunately there are few papers that analyse tissue damages after the catheter, or any other medical device, introduction in sheep brain.

Despite these limitations in the brain damage analysis in scientific literature, sheep has been used as large animal model of traumatic brain injury, and considering the experimental procedures, brain injury scenario is the more closer than others to our purpose. (Dai et al. 2018)

Considering the catheter introduction as a little penetrating brain injury we can identify "Penetrating brain injury" from all these models as a useful kind of brain injury model. This model could be comparable to our aims with all the differences of pathophysiological brain damage, methods, goal noted.

In literature the analysis of a brain injury can be done with three different methodologies (fig1) [10].

- Cerebrospinal fluid sample (Neurotransmitters)
- Blood sample (Interleukin, Cytokine, Neurotransmitters)
- Tissue analysis (Fluorescence dye, Immunohistochemistry, Histology, SEM, Digital microscopy)

Cerebrospinal fluid and blood sample can give us in real time information about development of the damage during the in vivo phases. Tissue analysis are done after the animal euthanasia.

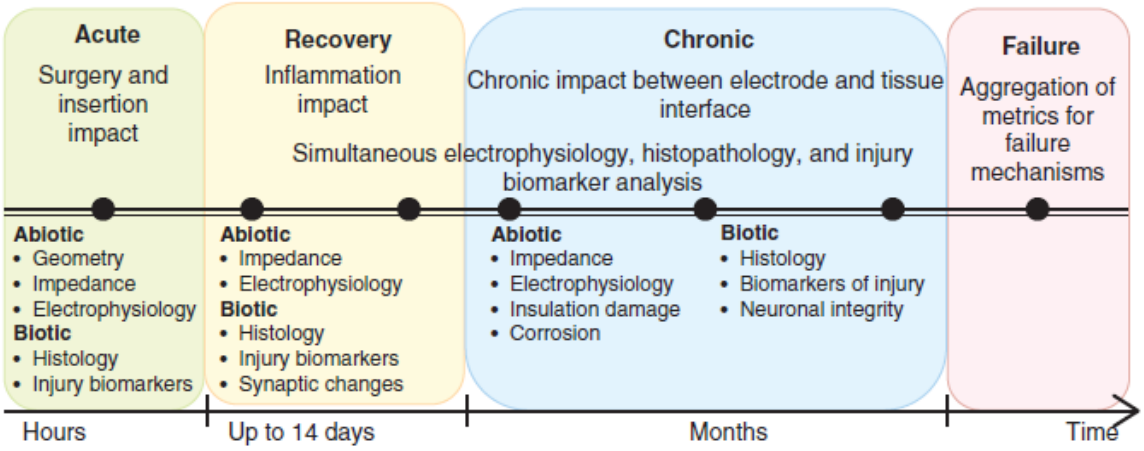

Figure 10 A suggested protocol for monitoring the evolution of "biotic" and "abiotic" factors that contributes to the failure of neural implant. [10, 11](McCreery 2016)

Methods

1) Blood analysis Elisa Test (IL-1 Beta; IL-18; TNF-alpha)

Cytokine are structural and functional components with pro and/or anti-inflammatory aims and are even mediators of the cellular immune responses.

Several reports indicate that interleukin (IL) IL-1 beta, IL-18 and tumour necrosis factor alpha (TNF alpha) are involved in the beginning and development of the inflammatory cascade after traumatic brain injury. IL 1 beta binds the receptors localized on microglia and astrocytes in brain. Activation of the neuroglial and immune cell IL1 receptors induct the production and release of inflammatory cytokines as IL-1 beta and IL-18. The damage effect of IL 1 beta can be also related to activation of TNF alpha.

IL-1 beta, IL-18 and TNF-alpha are all pro-inflammatory cytokines.

No papers involving traumatic brain injury used blood analysis with sheep as animal models. However several papers used cytokines analysis during the study of brain damages with different animal models as pigs and rats.(Dai et al. 2018)

2) Blood brain barrier (BBB) integrity with Evans blue. Correlation between catheters and BBB damages (Olympus Fluo View FV300)

The presence of the brain blood barrier makes difficult the use normal vital or necrotics dye administration. The drug administration must be done intravenously and the most dye molecules have a dimension bigger than 500-600 Da which is the size of the BBB pores. Besides that molecular dye are linking with carrier proteins as albumins which avoid the passage of the barrier.

The catheter during the insertion damage the brain parenchyma. The astrocytes make an intimate contact with the cerebrovascular endothelium of parenchymal blood microvessels and are critical for the normal function of BBB. Not only astrocytes are linked to the brain endothelium but even microglia interact with glia and endothelium cells in a paracrine manner. This anatomical and functional relationship showed the importance of gliovascular unit. The catheter damages this structure and the microcapillary circulation. Once the BBB is damaged the molecular can cross it and accumulate inside the brain area damaged.

A commonly used technique is the Evans Blue (EB), based on the ability of EB dye to bind to serum albumin immediately following its intravenous (IV) injection into the bloodstream. Since serum albumin does not cross the BBB under normal physiologic conditions, spectrophotometric determination of EB dye accumulation in brain tissue is carried out to analyse the extent of vascular leakage.

The analysis of the different tissue damages could be done by the Mapping of EB dye leakage in brain. With this method we should be able to explore with optical imaging to map vascular leakage and quantify EB by optical imaging and UV absorbance with fluorescence scanner (fig11-12). (Jaffer et al. 2013)

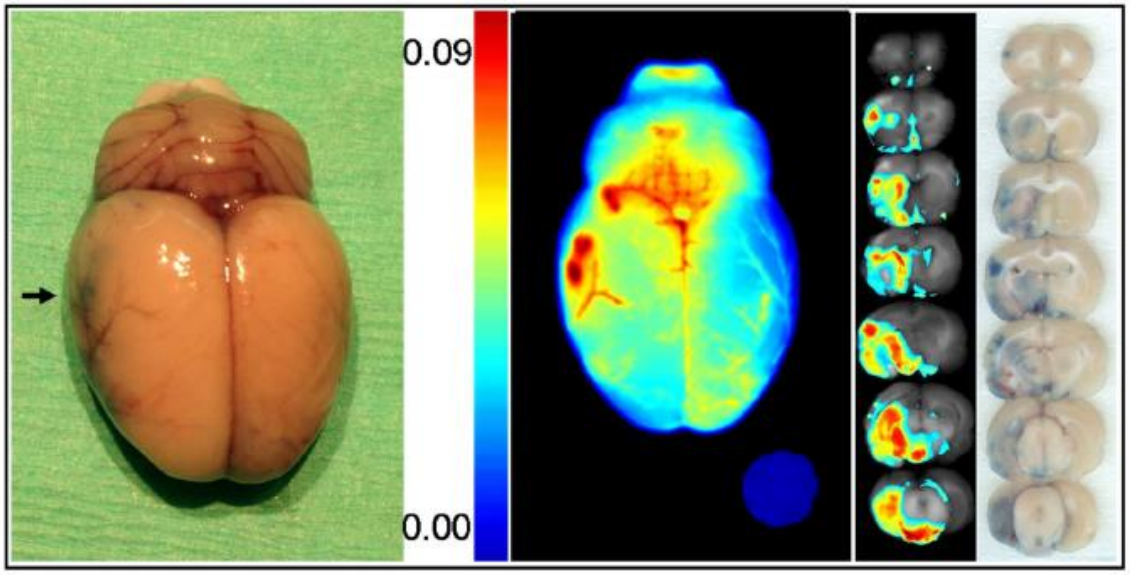

Figure 11: Vascular damage in stroke. Rat as animal model (Jaffer, Adjei and Labhasetwar 2013)

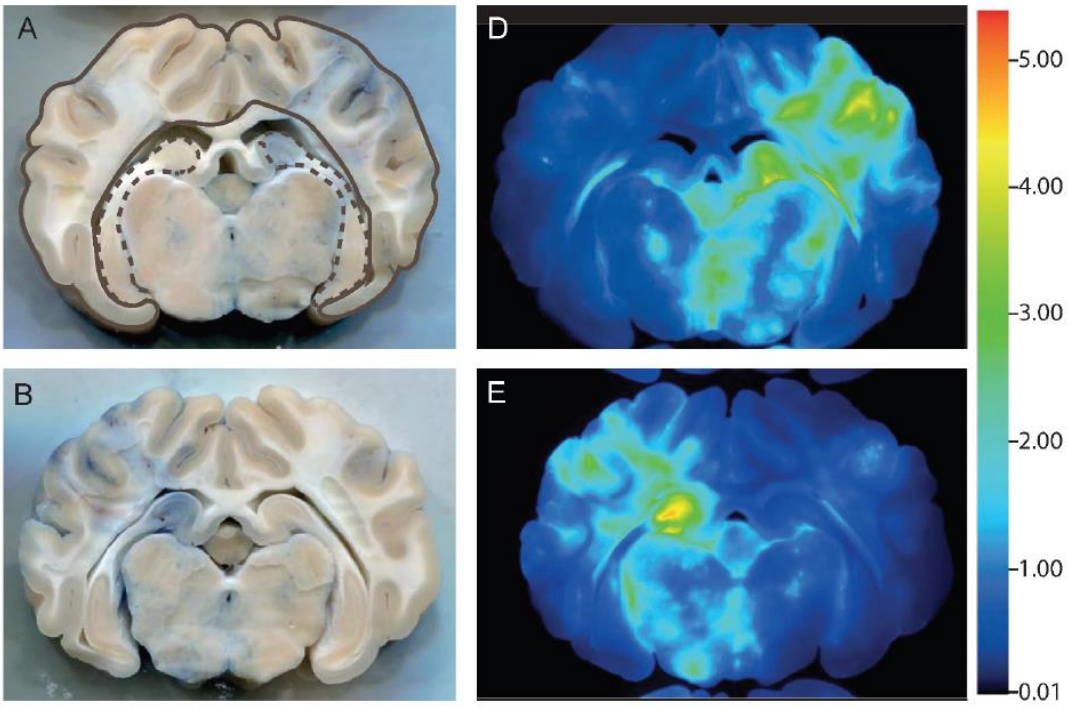

Figure 12: Analysis of Evans blue uptake in sheep brain (Pelekanos et al. 2018)

3) Histology with hematoxylin-eosin and Immunohistochemical analysis

The difference track shape can be observed with a normal histological study with hematoxylin and eosin. Brain can be cut with series of axial slides along the catheter trajectory (Tsumura et al.2016).

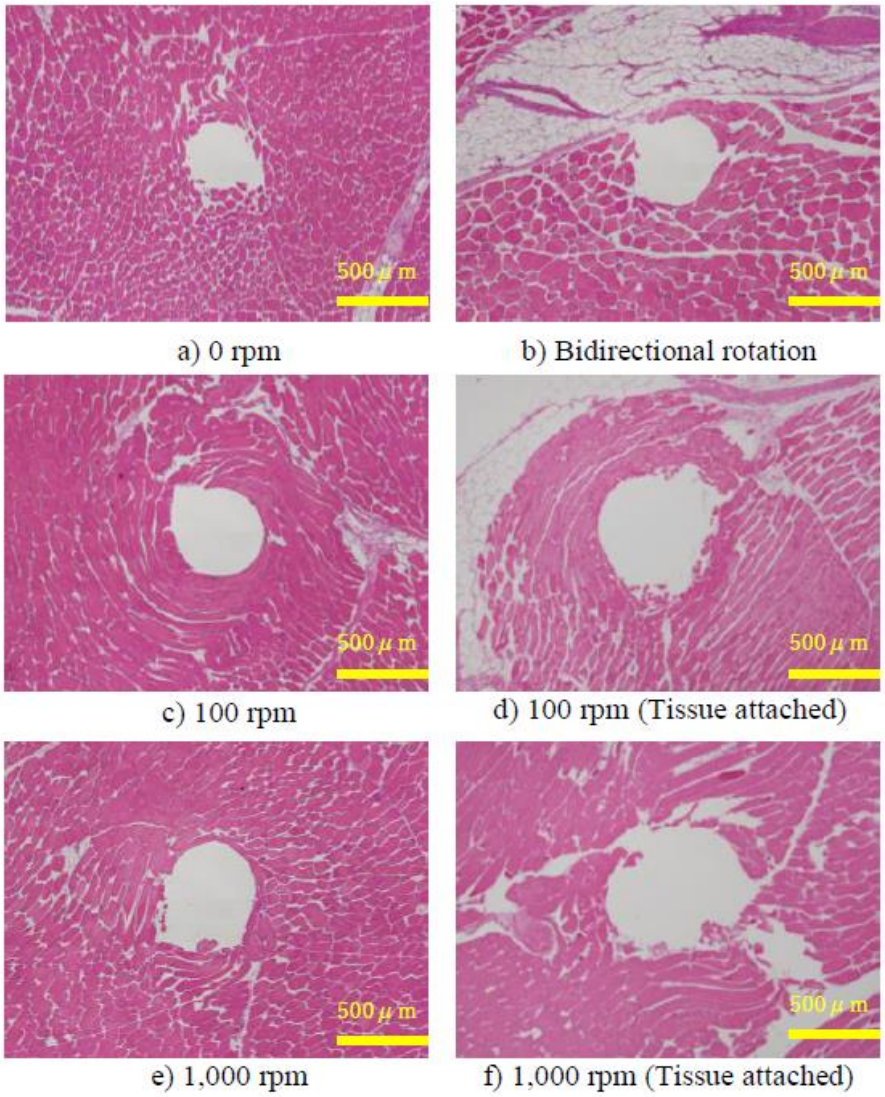

Figure 13: Histological Evaluation of Tissue Damage Caused by Rotational Needle Insertion Tsumura et al.2016

- Immunohistochemical detection with amyloid precursor protein (APP). APP is a membrane-spanning glycoprotein that is synthesised in normal neurons and involved in axoplasmatic transport. APP accumulates after distruption of the axonal cytoskeleton. It is not demonstrable in normal axons and immunostaining for APP can detect damaged axons within 60 minutes of injury. (Finnie et al. 2002)

4) Tissue preparation for Digital Microscope and FIB-SEM analysis (Fixation, Staining, Infiltration, Thermal curing)

Surface analysis:

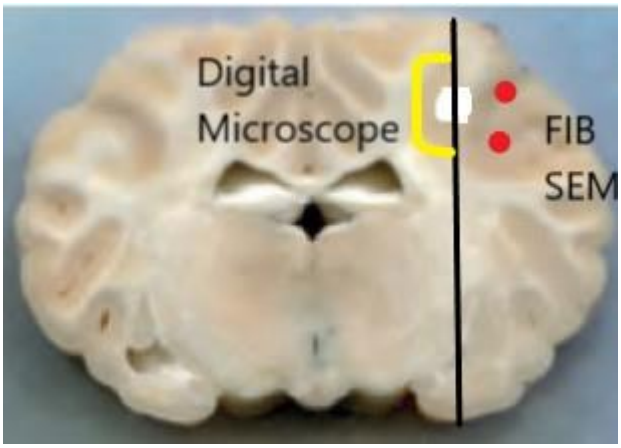

Figure 14: Example of sampling for different aims

- Sample preparing for Digital Microscope

Formalin 10 % fixing

- Sample preparing for FIB SEM analysis

FIXATION

1. Brain Samples is sectioned using scalpel blade into small pieces (puncher diameters).

2. Tissue samples are fixed for 2-3h at room temperature in 2% formaldehyde in 0.1 M sodium phosphate

buffer pH 7.4

3. Fixed samples are washed three times, 10’ each, in 0.1 M sodium phosphate buffer pH 7.4.

4. Fixed samples are left overnight in the fridge (~4°C), in 0.1 M sodium phosphate buffer pH 7.4.

STAINING

5. Samples are stained in 0.5% (w/v) osmium tetroxide (OsO4) in water for 1 h.

6. Samples are rinsed three times, 10’ each, in 0.1 M sodium phosphate buffer pH 7.4.

7. Samples are immersed in 25%, 50%,70% and 95% ethanol-water for 15’.

8. Samples are immersed in 100% ethanol two times, 15’ each.

INFILTRATION

9. Samples are immersed in 1:1 solution of ethanol and resin (LRWhite) for 2h.

10. Samples are immersed in 1:3 solution of ethanol and resin (LRWhite) for 2h.

11. Samples are immersed in pure resin overnight (LRWhite).

12. Add Catalyst to the LRWhite as per manufacturer instructions (full dissolution in 24h)

13. Oven temperature is set

14. Place samples in capsules and put in oven

- Polymerization in 24h at 60°C
- Polymerization in 48h at 40°C

- FIB SEM analysis (Zeiss Auriga Cross Beam)

The FIB SEM analysis will continue the work act by EDEN2020 based on the study of the normal white matter tracks in a healthy animal (see "Cytoarchitecture of commissural, association and projection fibres: a comparative study"). The team is studying the difference of cell structures, compression and damage of axons located into the brain parenchyma in peri-track area (figure 14). Samples form parenchyma surrounded the trajectory along the tracks and form the tips area will be taken and analysed.

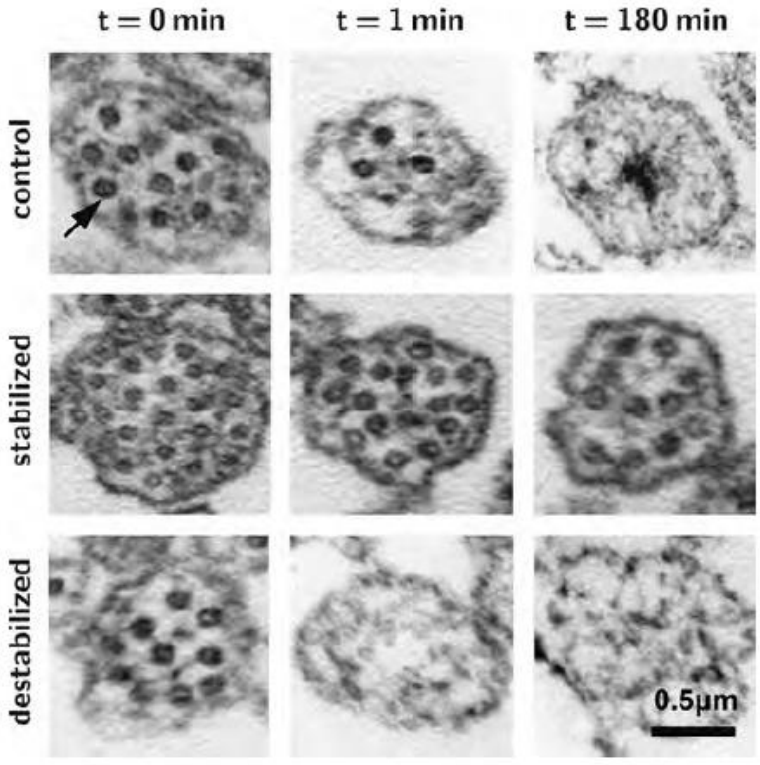

Figure 15: SEM analysis of axonal damage through the progressive loss of microtubules Tang-Schomer et al. 2010).

5) Cerebrospinal fluid and plasma neurotransmitters concentrations

In the immediate period following the primary brain injury there is a massive disturbance of the cellular ion homeostasis initiated by excessive release of the excitatory amino acid neurotransmitters glutamate and aspartate with the activation of glutamate receptors. The release of glutamate results in cellular influx of Na and Ca and efflux of K. The influx of calcium ions is considered the key event in early post traumatic brain injury leading to mitochondrial damage with an increase in free radical production (Marklund and Hillered 2011). If excess extracellular glutamate, glutamate receptors on the post-synaptic membrane will be excessively activated, resulting in excitotoxic injury, including the destruction of the Ca2C buffer system. Understand the neurotransmitters concentration after a brain injury can be useful to delineate a physiological response against the tissue damage.

In human the concentration of glutamate in the brain ranges from 1 to 10 μM, which is much lower than that in blood (40–60 μM) and astrocytes and neurons (10–100 μM). When the glutamate concentration in an endothelial cell exceeds the blood concentration, glutamate will be transported into the blood via facilitative transport. It is difficult for blood glutamate to enter the brain via either tight junctions or carriers (Bai et al. 2017). Under normal conditions, blood glutamate levels are maintained in a steady state by the blood brain barrier (BBB) (Chodobobski, Zink and Szmydynger-Chodobska 2011), however in a variety of brain diseases, the glutamate levels in the blood, cerebrospinal fluid (CSF) or both can significantly increase, and the normal intraparenchymal-blood glutamate concentration gradient is thereby disrupted (Bai et al. 2017). Analyses of Glutamate, Aspartate and Gaba in cerebrospinal fluid and blood concentration can be useful to outline the damage level of the brain injury after the catheters introduction and compare both. The neurotransmitters analysis on cerebrospinal fluid and plasma can be assayed using high performance liquid chromatography or mass spectrometry.

Hypothesis:

Plasma sample analysis

- Glutamate, Aspartate blood level increase = high BBB level damage
- Glutamate, Aspartate blood level decrease = low BBB damage. Neurotransmitters follow the gradient of concentration

- Glutamate, Aspartate blood level stable = no BBB damage detectable

Cerebrospinal fluid

- Glutamate and aspartate level increase = high brain parenchyma damage
- Glutamate and Aspartate level stable = no brain parenchyma damage detectable

Gaba is analysed as control neurotransmitter in consequence of its nature as inhibitory neurotransmitter. We assume that the concentration of Gaba would be always low and stable.

References

Preclinical testing of Neural Prostheses. In Neurobionics: The Biomedical Engineering of Neural Prostheses.

Bai, W., W. L. Zhu, Y. L. Ning, P. Li, Y. Zhao, N. Yang, X. Chen, Y. L. Jiang, W. Q. Yang, D. P. Jiang, L. Y. Chen & Y. G. Zhou (2017) Dramatic increases in blood glutamate concentrations are closely related to traumatic brain injury-induced acute lung injury. Sci Rep, 7, 5380.

Chodobski, A., B. J. Zink & J. Szmydynger-Chodobska (2011) Blood-brain barrier pathophysiology in traumatic brain injury. Transl Stroke Res, 2, 492-516.

Dai, J. X., Y. B. Ma, N. Y. Le, J. Cao & Y. Wang (2018) Large animal models of traumatic brain injury. Int J Neurosci, 128, 243-254.

Finnie, J. W., J. Manavis, P. C. Blumbergs & G. E. Summersides (2002) Brain damage in sheep from penetrating captive bolt stunning. Aust Vet J, 80, 67-9.

Jaffer, H., I. M. Adjei & V. Labhasetwar (2013) Optical imaging to map blood-brain barrier leakage. Sci Rep, 3, 3117.

Marklund, N. & L. Hillered (2011) Animal modelling of traumatic brain injury in preclinical drug development: where do we go from here? Br J Pharmacol, 164, 1207-29.

McCreery, D. 2016. Preclinical testing of Neural Prostheses. In Neurobionics: The Biomedical Engineering of Neural Prostheses.

Pelekanos, M., G. Leinenga, M. Odabaee, S. Saifzadeh, R. Steck & J. Götz (2018) Establishing sheep as an experimental species to validate ultrasound-mediated blood-brain barrier opening for potential therapeutic interventions. Theranostics, 8, 2583-2602.

Tang-Schomer, M. D., A. R. Patel, P. W. Baas & D. H. Smith (2010) Mechanical breaking of microtubules in axons during dynamic stretch injury underlies delayed elasticity, microtubule disassembly, and axon degeneration. FASEB J, 24, 1401-10.

Tsumura, R., Y. Takishita, Y. Fukushima & H. Iwata (2016) Histological evaluation of tissue damage caused by rotational needle insertion. Conf Proc IEEE Eng Med Biol Soc, 2016, 5120-5123.

Further work related to the PhD period

Sheep Brain Slicer

Introduction

Nowadays imaging techniques allow to obtain sensitive measure of tissue integrity. MRI can identify areas of abnormality and pathological processes which are the common features in experimental trials. The high sensibility of the imaging procedures biopsy is often required to diagnose and differentiate pathological processes. Nevertheless histological information are mandatory for a certain diagnosis and the possibility to compare the data acquired from different techniques is a value added in research.

For sheep as animal model the sampling from specific brain area is hard and some limitations can occur. For a proper comparison the orientation of MRI slice plane must match the sectioning plane of the brain tissue when cut. The large size of the brain makes hardly applicable the normal brain cutting on a flat surface, the sampling is consequently not accurate.

In order to be able to compare the pathological or normal brain tissue between the histology sections and MRI studies a brain slicer tool is needed.

Here we presented a method to create a custom brain holders and slicers from a real sheep brain.

Methods

Female adults, 70kg, *Ovis Aries* sheep *Bergamasca* heads were used.

The brain was removed after a craniotomy using a surgical oscillating saw respecting the organ anatomy. The sheep brain obtained has been casted in silicon rubber malleable glue in order to create a plastic brain clone. (figure 16).

The silicon brain has been then immersed into a case gypsum filled and the brain shape has been engraved in a gypsum cast (figure 16).

Laser scanner machine that has been used to create a mesh from the gypsum case of the brain case surface. The brain mesh has been uploaded in Solidwork software for three dimensional parametric design and planning.

A sheep brain slicer has been molded using a Boolean subtraction of the sheep brain mesh to a solid. The slice paths have been designed for coronal or sagittal sections, to manage to isolate specific sheep brain regions quickly and consistently or in case prepare uniform slices for microtome dissection.

Two brain slicer prototypes have been designed. Once with coronal slicer cut along all the brain area and one sagittal lane passing through the middle brain area (figure 17). The second with sagittal slicer cut along all the brain area and one coronal lane passing through the middle brain area (figure 17). The cut lane dimension has been set in 0.5 mm.

Once designed the sheep brain slicer has been create with a 3D printer in plastic material for a demo purpose (figure 18) and then printed in surgical steel (figure 19).

With these two slicer models is possible to reach a good sampling method reproducing it within the same target area x and y values.

Figure 16: Sheep brain casting

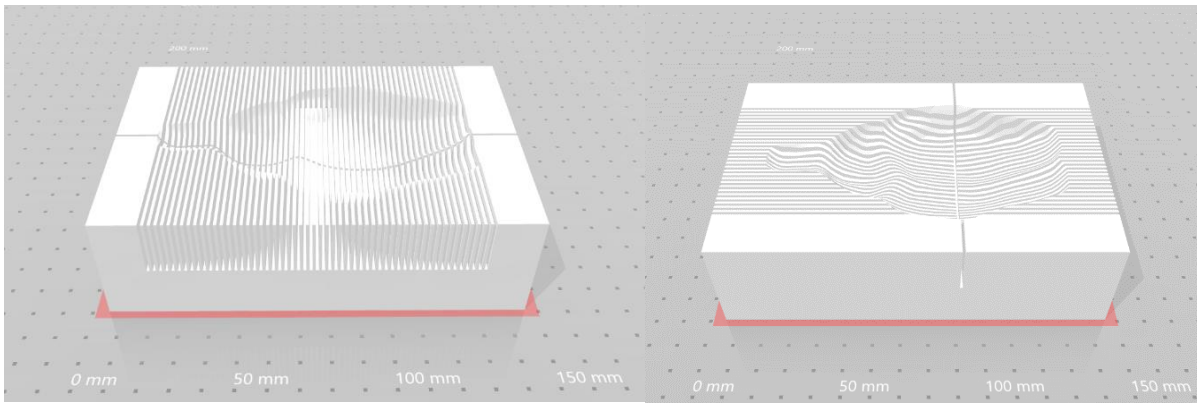

Figure 17: Sheep brain slicer designed in Solidwork

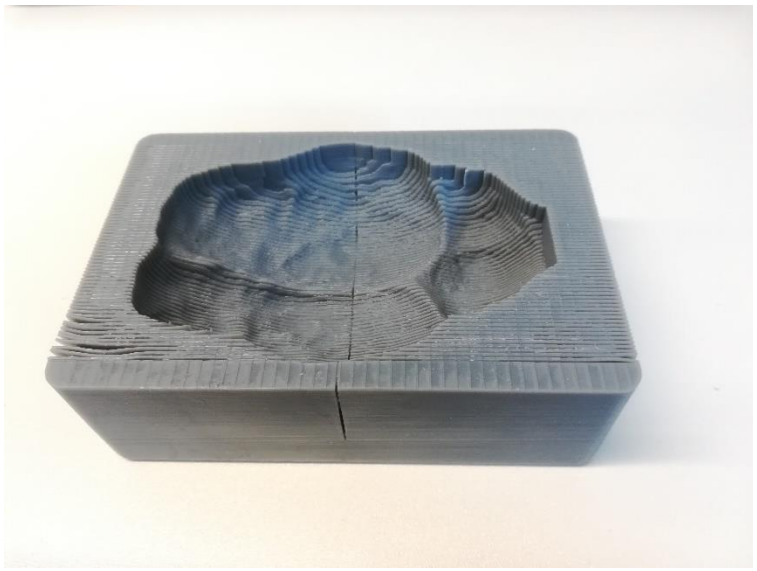

Figure 18: Sheep brain slicer Demo, printed in plastic material with a 3D printing machine

Figure 19: Sheep brain slicer with coronal cut rows